

Characterization and Application of Nanomaterials

VOLUME 3 , ISSUE 2 , 2020

2

ISSN: 2578-1995



Editorial Board

Editor-in-Chief

Prof. Sergey Victor Bulyarskiy

Institute of Nanotechnologies of Microelectronics
Russian Federation

Dr. Mohsen Sheikholeslami

Department of Mechanical Engineering, Babol Noshirvani University of Technology
Islamic Republic of Iran

Editorial Board Member

Dr. Nikolai Inokent'evich Plusnin

Institute of Automation and Control Processes
Russian Federation

Prof. Umapada Pal

Autonomous University of Puebla
Mexico

Prof. Levan Sandro Chkhartishvili

Georgian Technical University
Georgia

Prof. Haiping Xu

Shanghai Polytechnic University
China

Prof. Mostafa Ibrahim Abd-Elrahman

Assiut University
Egypt

Dr. Amir Sadeghi

Institute of Material Science and Engineering
Germany

Dr. Simge Gencalp Irizalp

Manisa Celal Bayar University
Turkey

Dr. Munshi Mahbubul Basit

Georgia Southern University
United States

Dr. Marcio Fernandes Leão

Federal University of Rio de Janeiro
Brazil

Dr. Hari Prasad Reddy Kannapu

Hanyang University
Republic of Korea

Prof. Serap Derman

Yildiz Technical University
Turkey

Dr. Sivasankaran Harish

Kyushu University
Japan

Dr. Muhammad Saeed

Government College University Faisalabad
Pakistan

Dr. Soheil Gohari

The University of Melbourne
Australia

Prof. Mumin Sahin

Trakya University
Turkey

Dr. Maryam Zohri

Tehran University of Medical Science
Islamic Republic of Iran

Characterization and Application of Nanomaterials

Editor-in-Chief

Prof. Sergey Victor Bulyarskiy

*Institute of Nanotechnologies of Microelectronics
Russian Federation*

Dr. Mohsen Sheikholeslami

*Department of Mechanical Engineering
Babol Noshirvani University of Technology
Islamic Republic of Iran*

Characterization and Application of Nanomaterials

<https://systems.enpress-publisher.com/index.php/CAN/index>

Contents

Original Research Article

49 Effect of heating and resistance on emission properties of carbon nanotubes

Sergey V. Bulyarskiy, Alexander A. Dudin, Alexander V. Lakalin, Andrey P. Orlov, Alexander A. Pavlov, Roman M. Ryazanov, Artemiy A. Shamanaev

60 Coal combustion residues characterization using scanning electron microscopy & energy dispersive X-ray (SEM-EDXA) analysis

Ritesh Kumar, Sadanand Sharma, Ajit Kumar, Charu Arora

73 Relative stability of planar clusters B₁₁, B₁₂, and B₁₃ in neutral- and charged-states

Levan Chkhartishvili

81 Subnanophase coatings as new type low-dimensional nanomaterials: Ultra-high-vacuum synthesis, properties and application

Nikolay Plusnin

Review Article

87 A review on metal-organic framework: Synthesis, properties and application

Sanju Soni, Parmendra Kumar Bajpai, Charu Arora

ORIGINAL RESEARCH ARTICLE

Effect of heating and resistance on emission properties of carbon nanotubes

Sergey V. Bulyarskiy^{1*}, Alexander A. Dudin¹, Alexander V. Lakalin¹, Andrey P. Orlov¹, Alexander A. Pavlov¹, Roman M. Ryazanov², Artemiy A. Shamanaev²

¹Institute of Nanotechnology of Microelectronics of the Russian Academy of Sciences, 32A Leninskii pr., Moscow, 119991, Russia; E-mail: bulyar2954@mail.ru

²Scientific-Manufacturing Complex «Technological Centre» build 1, Shokin sq., Zelenograd, Moscow, 124498, Russia

ABSTRACT

We have studied the effect of the series resistance on the heating of the cathode, which is based on carbon nanotubes and serves to realize the field emission of electrons into the vacuum. The experiment was performed with the single multi-walled carbon nanotube (MCNT) that was separated from the array grown by CVD method with thin-film Ni-Ti catalyst (nickel 4 nm/Ti 10 nm). The heating of the cathode leads to the appearance of a current of the thermionic emission. The experimental voltage current characteristic exhibited the negative resistance region caused by thermal field emission. This current increases strongly with increasing voltage and contributes to the degradation of the cold emitter. The calculation of the temperature of the end of the cathode is made taking into account the effect of the phenomenon that warms up and cools the cathode. We have developed a method for processing of the emission volt-ampere characteristics of a cathode, which relies on a numerical calculation of the field emission current and the comparison of these calculations with experiments. The model of the volt-ampere characteristic takes into account the CNT's geometry, properties, its contact with the catalyst, heating and simultaneous implementation of the thermionic and field emission. The calculation made it possible to determine a number of important parameters, including the voltage and current of the beginning of thermionic emission, the temperature distribution along the cathode and the resistance of the nanotube. The phenomenon of thermionic emission from CNTs was investigated experimentally and theoretically. The conditions of this type emission occurrence were defined. The results of the study could form the basis of theory of CNT emitter's degradation.

Keywords: Carbon Nanotubes; Field Emission; Thermionic Emission; Volt-ampere Characteristic; Emitter Temperature

ARTICLE INFO

Article history:

Received 11 October 2020

Received in revised form 4 November 2020

Accepted 9 November 2020

Available online 21 November 2020

COPYRIGHT

Copyright © 2020 Sergey V. Bulyarskiy *et al.*

doi: 10.24294/can.v3i2.567

EnPress Publisher LLC. This work is licensed under the Creative Commons Attribution-NonCommercial 4.0 International License (CC BY-NC 4.0)

<http://creativecommons.org/licenses/by/4.0/>

1. Introduction

The carbon nanotubes (CNTs) have the important practical properties such as high electrical and thermal conductivity, suitable mechanical properties, and ability to absorb and emit electromagnetic waves^[1]. Scientists from all over the world have developed the variety of convenient technological methods for producing CNTs, which promotes the development of studies of this allotropic form of carbon. At present, various practical applications of nanotubes are shown, including field-effect transistors, lithium-ion batteries, radiation receivers, interconnections of integrated microcircuits, conductive composites, etc.^[1] CNTs have a small diameter. For the case with single-walled CNT, it is from 0.8 to 1.5 nm; for multi-walled CNT — from units to tens nanometers, CNT's diameter is much less than their

length (large aspect ratio), which results in enhancement of the electric field near the CNT's tip and contributes to field emission. Several papers that appeared in 1995 described the phenomenon of field emission in CNTs^[2-4]. This phenomenon formed the basis for a number of important applications from the point of view of practical applications: flatscreens^[5,6], miniature X-ray tubes^[7,8], light-emitting devices^[9,10], miniature vacuum lamps^[11,12], terahertz amplifiers^[13,14], and high-frequency vacuum switches^[15].

For widespread use of field emission (FE), it is necessary to study the possibility of achieving high emission current densities and stability of this process. These issues are discussed in detail foremost from the theoretical point of view, in particular, the necessary information can be found in the reviews^[16,17].

Voltage-current characteristic of cold cathode in the region of prevalence of field emission current is generally described by Fowler-Nordheim formula. Detailed analysis of this model and its transition to the region of thermionic emission was carried out in the studies of Rupesinghe *et al.*, Eletsii, Bocharov & Eletsii, and Murphy^[15,18]. The calculations of field-emission current for CNT were shown in several studies, for example, in the studies of Rupesinghe *et al.*, Eletsii, Bocharov & Eletsii, Murphy, as well as Mayer & Lambin^[15-19]. Fowler-Nordheim dependence in usable form has a formula^[20]:

$$J = \frac{eE}{\pi h \phi t y} \left(- \frac{\pi \sqrt{m} \phi \theta y}{heE} \right) \quad (1)$$

where: $t(y) = 1 + 0.1107 \cdot y^{1.33}$, $\theta(y) = 1 - y^{1.69}$,

$y = \frac{e}{\phi} \sqrt{\frac{eE}{\pi \epsilon}}$, e is elementary charge (C); h is Planck constant (J·s); E is the local electric field strength near the emitting surface (V/m); ϕ is work function of an electron from a CNT (J); m is free-electron mass; J is current density of the FE (A/m²). $t(y)$ и $\theta(y)$ are weakly varying functions that can be taken equal to unity without increasing the error in determining the work function. We can

neglect the weak power dependence of the functions $t(y)$ and $\theta(y)$ by setting $t(y) \approx 1$ and $\theta(y) \approx 1$. This condition allows us to obtain the following formula for calculating of the work function:

$$J = 1.54 \cdot 10^{-6} \frac{E^2}{\phi} \exp\left(-\frac{6.83 \cdot 10^9 \phi^{3/2}}{E}\right) \quad (2)$$

where: $[\phi] = \text{eV}$; $[E] = \text{V/m}$; $[J] = \text{A/m}^2$.

The experimental results are often represented in the Fowler-Nordheim coordinates: $\ln(J/E^2) = f(1/E)$. A straight line approximates these results and the work function is calculated from the slope of which. The amount of the calculation these work function depends on the choice of the initial and final electric field strengths, which specify the region of the current-voltage characteristic. In generally, this choice is not motivated. Therefore, the result of calculating contains significant systematic errors.

Even in the first papers devoted to field emission, it was found that CNT's tip is heated by flow of field-emission current, and its temperature is proportional to the square of the current density^[19,21], which is quite obvious in accordance with the Joule-Lenz law. Models that are more complex were considered in the studies of Bocharov *et al.*^[16] and Murphy *et al.*^[17]

A single nanotube has a rather large thermal resistance. This resistance prevents the release of heat into the substrate with which the lower end of the nanotube is connected. CNT's tip heating leads to thermionic emission current, which may be large and even exceed the field emission current. Moreover, the resistance of CNT's changes the voltage-current characteristic as a function of temperature and current value due to an additional voltage drop. CNT's resistance makes a definite contribution to the form of the voltage-current characteristic, taking part of the voltage to itself at high current densities. Thus, CNT's resistance leads to a deviation of the experimental results from Ed. (1). Therefore, when researchers involve only Fowler-Nordheim dependence to determine the work function, they admit two systematic errors: firstly, thermionic emission is neglected, and, secondly, they

don't take into account the voltage drop on the nanotube.

In this paper, the emission currents of a single multi-walled nanotube have been studied experimentally in a wide range of current values. The authors have revealed deviations of the current-voltage characteristic from the Fowler-Nordheim dependence. Moreover, the calculation of the temperature of CNT's heating has been carried out, and the conditions under which the nanotube resistance and the thermionic emission current have a significant effect on the voltage-current characteristic shape were analyzed, and the algorithm for CNT parameters calculating was presented, namely, the electrical resistance, the dependence of the CNT heating temperature from the current value.

2. Experimental results

Carbon nanotubes were grown by the chemical vapor deposition (CVD) method in Plasmalab System 100 (Oxford Instruments) on silicon substrate on which a catalyst was deposited consisting of a two-layer metal film: titanium 10 nm and nickel 2 nm. The film of the catalyst was covered with silicon oxide, in which windows were opened with a diameter of 0.7 μm . The CNT growth was carried out by CVD method. Gas flow consisted of an acetylene with addition of ammonia in a 3:1 ratio rate. It was constant during the growth process. The synthesis temperature was 600 $^{\circ}\text{C}$. As a result, single multi-walled carbon nanotubes 2-3 μm in height were obtained (**Figure 1**).

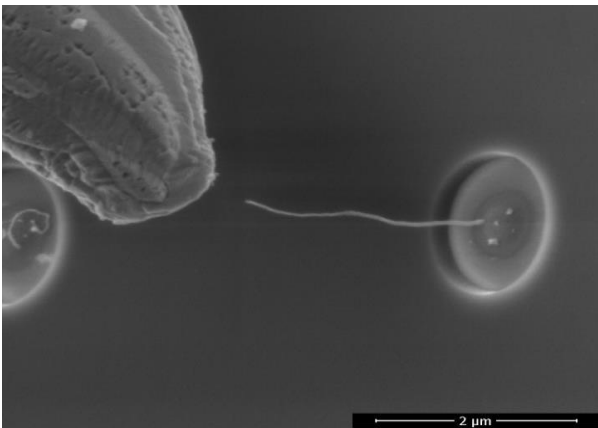


Figure 1. SEM image of single multi-walled carbon nanotube (cathode) and tungsten tip (anode).

The measurements were carried out in a high vacuum in the chamber of two-beam FEI Helios NanoLab 650i system. A measuring electron microscope could obtain images with a resolution of not worse than 0.7 nm at an accelerating voltage of not more than 1 kV. The pressure in the measuring chamber was $5 \cdot 10^{-5}$ Pa. In this chamber there was a probe system Kleindiek Nanotechnik with 4 separate independent manipulators that can operate at voltages up to 150 V. Each probe had its own coaxial connector. For current-voltage measurements on DC currents, a programmable two-channel source-meter Source Meter 2634B from Keithley was used. This device can measure currents up to 10^{-15} A. It is equipped with special shielded three axial leads with the function of ultra-low currents compensation. The input impedance of source-meter (over 100 Volts) provides a minimum level of the introduced distortions and errors in tested circuits during the measurements for this class of instruments.

The voltage-current characteristic of emission current of the single multi-walled CNT is shown in **Figure 2**. It was the starting point for further processing. The electrical circuit in which the emission current flows is shown in the inset of **Figure 2**. This current consists of two components: its nonlinear resistance characterizes field emission and thermionic emission, each of these processes (R_{FE} and R_{TE}). The total voltage applied to the circuit (U) is composed of the sum of the voltages, one of which falls on the resistance of the nanotube (U_R), and the other one — on the nonlinear resistance of the emitting tip of the nanotube (U_E). We must divide the current of the current-voltage characteristic into two components. One component is the field emission current, and the second component is the thermionic current. These components are determined by the following sequence of actions:

- 1) The field emission current is calculated (the calculations are shown in the following subsection). The work function is selected in such way that the field-emission current coincides with the initial section of the experimental voltage-current characteristic (**Figure 2**). This calculation allows us to determine U_E .

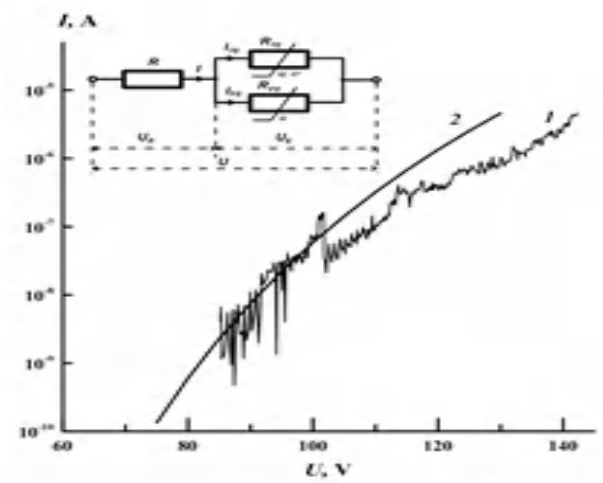


Figure 2. Voltage-current characteristic of the emission current of the single multi-walled CNT: 1 — experimental; 2 — modeling by formula; Top corner: equivalent circuit of CNT.

2) The voltage of the model curve, there is a deduction from the voltage of the experimental curve for each current value. The difference of these voltages makes it possible to determine U_R (**Figure 2**), to construct the current-voltage characteristic of the series resistance of a carbon nanotube and calculate this resistance $R=10\text{ M}\Omega$. Then the model value of the voltage drop across the series resistance of a nanotube is: $U_R = IR$.

3) We are conducting the second stage of modeling the volt-ampere characteristic. The total theoretical voltage (U_t), which should be on the emission system, is calculated as the sum of the voltage on the nonlinear resistance of the emitting tip of the nanotube (U_E) and the series resistance (U_R). We calculate the difference between the theoretical and experimental voltage drops at each current value: $U_t - U = U_E + U_R - U$. The result is a volt-ampere characteristic of the section, which contains two parallel non-linear resistances (R_{FE} and R_{TE}). The result of the transformations is shown in **Figure 3**. This figure shows the initial experimental current Ed. (1); field emission current Ed. (2); the experimental section of negative resistance Ed. (3). The voltage reaches a critical value (U_c) at a critical value of the current (I_c). Further increases of the current leads to a heating of the nanotube, as a result of which, the resistance for the thermionic current decreases. This leads to a decrease in voltage drop across the parallel connection section of non-

linear resistances. The voltage at the end of the nanotube, which emits electrons, falls and the emission current decreases. It is evident that when CNT's tip is heated to a certain critical temperature, a thermionic emission current appears, and the voltage at the emitting end (U_E) falls. A section of negative resistance is present, then: $I > I_c$. The current that exceeds the critical region is thermionic in fact. The field emission current does not exceed the critical current.

Thus, the thermionic current component dominates when the total current density exceeds a critical value. This is because the end of the tube is heating when the current flows. The temperature of the end of the tube grows. Its temperature can reach several thousand degrees. This temperature leads to CNT destruction and the emission current degrades. The phenomenon of degradation of the field emission current is due to overheating of the nanotube. Below, we will carry out the necessary calculations to determine the conditions under which the emission process will be stable.

3. Modeling

3.1. Calculation of the currents of the field emission of a carbon nanotube (CNT)

The efficiency of field emission depends essentially on the electric field strength near the emitting surface. Therefore, the electric field strength requires an exact calculation. The calculation is carried out in two stages: first, the potential distribution and the magnitude of the electric field at the end of the tube are calculated; secondly, the current density of the cathode is calculated. The calculation of the electric field potential distribution is carried out in the classical approximation. We applied a model in which a CNT is a solid body of cylindrical shape. The end of this body represents a hemisphere (CNT with a closed end) or half a torus (CNT with an open end). This body has a metallic type of conductivity. The potential of the electric field is found by solving the 3-dimensional Laplace equation in the boundary element with the conditions given on its boundary. The solution of the Laplace equation was found by the boundary element

method, which is described in detail in the studies of Banerjee & Butterfield and Brebbia *et al.*^[22, 23]. This method involves splitting the surface of a solid body into triangular elements and forming the computational grid. Then the boundary conditions are given on its boundaries. As a result, instead of solving the integral equation, a system of linear algebraic equations is solved. By solving, we obtain the coefficients required for calculating the potentials in corresponding space points of emission system.

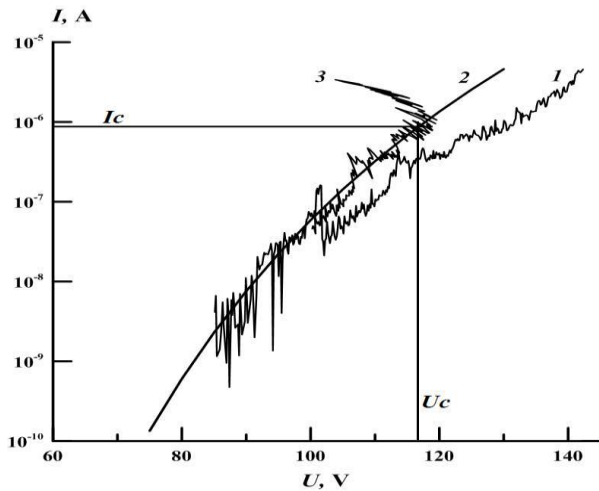


Figure 3. Current-Voltage characteristics of the investigated CNT: 1 — experimental I-V characteristic; 2 — modeling I-V characteristic (Ed. 3); 3 — I-V characteristic of the section, which contains two parallel non-linear resistances (R_{FE} and R_{TE}).

Partitioning of the boundary surface to boundary elements (BE), on the one hand, need to be quiet detailed to consider all special aspects of surface and on the other hand should not exceed a certain value due to the computing power used by the computer (memory capacity, processing speed). Based on these conditions, in this case, the entire boundary surface is divided into 20000–30000 triangular BE.

Electric field strength distribution must be calculated near all points of the CNT surface, since the cathode current is caused not only by emission from its end, but also from regions near it. **Figure 4** shows the emission system under investigation consisting of a single CNT (cathode) and an anode electrode, as well as its idealized model, which was later used to calculate the distribution of the electric

field and the field emission current.

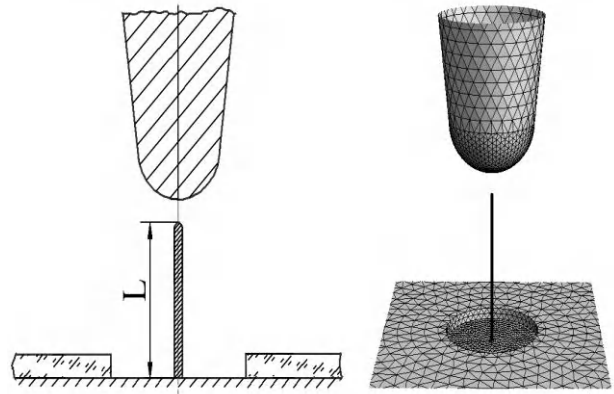


Figure 4. Model of a single CNT (cathode) and an anode electrode.

Geometric parameters of the calculation were obtained as a result of determining the size of a real experimental system, which is shown in **Figure 4**.

A system of equipotential surfaces was obtained after the implementation of the above mentioned calculation algorithm. The electric field strength was calculated as the potential gradient near the surface.

The cathode current is the sum of the current of the total boundary elements. Electrons, which are emitted by these elements, moved along a certain trajectory and, at the end of their path, hit the anode. The motion of an electron along a trajectory causes the formation of an elementary electric current. The sum of these currents over the area of the cathode creates an emission current (cathode current), as well as the components of this current that fall on other elements of the emission system (anode current, leakage current, etc.). Such approach is permissible on the basis of an estimate of the electron velocity in the system. The velocity of an electron in the corresponding electric field can be estimated from the law of energy conservation:

$$V = c \sqrt{1 - \left(\frac{m_0 c^2}{m_0 c^2 + eU} \right)^2}$$

Where: c is light velocity; m_0 is electron rest mass; U is accelerating voltage between cathode and anode. In the experiments, U did not exceed 150 V, therefore $V \leq 5 \cdot 10^6$ m/s.

Thus, the electron velocity is much smaller

than the speed of light, so they move with nonrelativistic velocities and the laws of classical mechanics can be used to calculate their trajectories of motion. We will assume that the Coulomb force acts on the electron, which must be used in the motion equation. The numerical integration was done by Euler's method^[24]. It should be noted that in the case of random cathode geometry (not flat) in Eqs. (1) and (2), E is understood as the field strength near the surface of the emitting elementary cathode pad, rather than the average value obtained by dividing the applied voltage by the distance between the anode and the cathode. When calculating the field-emission current from a single CNT, it is assumed that each BE of the cathode emits a current I_i , which is defined as $I_i = J_i \Delta S_i$, where J_i is the current density of the i -th BE of cathode, ΔS_i is the surface area of the i -th cathode BE (the surface area of the entire cathode $S = \sum \Delta S_i$). The current density J_i is calculated from the Fowler-Nordheim Ed. (1), in which the electric field strength E_i is taken from the solution of the Laplace equation for a given initial point at the center of each i -th BE. Then the total field emission current of the cathode is found by summing the currents over all sites ΔS_i :

$$I = \sum_i J_i \Delta S_i = \sum_i \frac{e^3 E_i^2}{8\pi h \phi t^2(y_i)} \exp\left(-\frac{8\pi\sqrt{2m}\phi^{3/2}\theta(y_i)}{3heE_i}\right) \Delta S_i \quad (3)$$

3.2. Calculation of the heating temperature of the end of a single carbon nanotube

The nanotube is heated when an electric current flows in it. Its temperature is not the same at its two ends. It is assumed that the temperature of the nanotube end, which is in contact with the substrate, is equal to the temperature of the substrate. The temperature of the opposite end was calculated by solving the heat-transfer equation taking into account the radiative cooling and the release of heat, which is caused by the current flow^[21,25]:

$$S \frac{d}{dx} \left(k(T) \frac{dT}{dx} \right) dx - 2\pi r \eta \sigma (T^4 - T_0^4) dx + I^2 \frac{R(T)}{L} dx = 0 \quad (4)$$

Where: $S = \pi(r^2 - r_0^2)$ is cross-section area of CNT; r is outer radius of CNT; r_0 is inner radius of CNT; $k(T)$ is coefficient of heat conductivity along the CNT axis; $T=T(X)$ is the temperature along the

CNT axis; T_0 is the temperature of surrounding bodies (substrate); L is length of CNT; $R(T)/L$ is electrical resistance of a unit length of CNT; η is the coefficient of the grayness of the thermal radiation of CNT ($\eta < 1$) in our case, which was taken equal to 0.9; $\sigma = 5.67 \cdot 10^{-8} \text{ W}/(\text{m}^2 \text{K}^4)$ is Stefan-Boltzmann constant; I is the current flowing through CNT (emission current). The boundary conditions for equation (4) have the formula:

$$T(0) = T_0, \quad \frac{dT(L)}{dx} = 0. \quad (5)$$

In the study of Vincent *et al.*^[21], the analytical solution of Ed. (4) was obtained in the absence of radiative cooling and provided that the thermal conductivity coefficient k , as well as the resistance R of the nanotube, which do not depend on temperature. However, for the case with CNTs there is a temperature dependence of k and R , therefore the results of Vincent *et al.*'s study^[21] should be considered as approximate. It was assumed in Bocharov & Eletsii's study^[25] that the thermal conductivity coefficient k and the resistance R are described by power functions of temperature. For the case: $k = aT^3$, $R = bT^d + c$ in Bocharov & Eletsii's study^[25], an analytic solution of Ed. (4) was obtained. In the study of Bocharov *et al.*^[26], it was assumed that: $k = k_0 (T/T_0)^\alpha$, $R = R_0 (T/T_0)^\alpha$, where α is an adjustable parameter, and equation (4) was solved numerically.

However, power-law dependence with the form $k = CT^\alpha$ for the thermal conductivity coefficient occurs only at temperatures below the Debye characteristic temperature^[27]. At high temperatures, due to the anharmonicity of long-wave oscillations and other causes, the thermal conductivity of a solid body decreases according to the law $1/T$, namely in the study of Ziman^[27]:

$$k = k_0 \frac{\Theta}{T} \quad (6)$$

Where: Θ is Debye temperature. The energy of the Debye phonon of carbon nanotubes is 0.103 eV^[28]. Accordingly, the Debye temperature is $\Theta = 1190\text{K}$. It is the dependence that dominates in the high-temperature region, when thermionic emission is possible. Therefore, for calculating the heating of

the nanotube, the dependence Ed. (6) was chosen.

The correct calculation of the temperature of nanotubes should be taken into account both their heating due to Joule heat, and cooling due to the Nottingham effect^[29]. The Nottingham effect is manifested in the cooling of the cathode. This effect is the result of the difference between the average energy of the electrons that leave the cathode and the electrons from the volume of the nanotube that takes their place. The electron that leaves the CNT carries away from the nanotube energy equal to the average energy of the thermal motion $(3/2)k_B T$ ^[30]. The number of electrons that are emitted from the cathode per unit time is I/e . Then the boundary condition Ed. (5) at the point $x=L$ will have the formula:

$$\frac{dT(L)}{dx} = -\frac{\sigma}{k} (T^4(L) - T_0^4) - \frac{3k_B T(L)}{2} \cdot \frac{I}{ekS}$$

The first term describes the cooling of CNTs by radiation from the end surface^[29,30], the second term due to the Nottingham effect^[30]. In addition, the temperature dependence of the resistance of CNTs has the formula^[30,31]:

$$R(T) = \frac{L}{S} \rho_0 (1 - \alpha T + \beta T^{3/2}) \quad (7)$$

Where: ρ_0 is the resistivity of CNTs. The heat conduction Ed. (4) takes the form with allowance for Ed (6), (7):

$$\left\{ \begin{array}{l} k \frac{\Theta}{T} S \left(\frac{dT}{dx} - \frac{1}{T} \left(\frac{dT}{dx} \right) \right) - \pi r \eta \sigma (T - T_0) + I \frac{\rho_0 (-\alpha T + \beta T^{3/2})}{S} = \\ T = T \\ \frac{dT}{dx} = -\frac{\sigma}{k} \frac{\Theta}{TL} (T L - T) - \frac{k_B T L}{ek} \cdot \frac{I}{ek \frac{\Theta}{TL} S} \end{array} \right. \quad (8)$$

The system that is given by Ed. (8) is solved by a numerical method to determine the temperature of the end of a nanotube that emits electrons. The values of the parameters were assumed to be equal to: $\alpha=8.5 \cdot 10^{-4} \text{ K}^{-1}$ ^[31]; $\beta=9.8 \cdot 10^{-6} \text{ K}^{-3/2}$ ^[31]; $\rho_0=2.33 \cdot 10^{-3} \Omega \cdot \text{m}$ ^[31]; $L=2.36 \text{ } \mu\text{m}$; $r=20 \text{ nm}$; $r_0=15 \text{ nm}$; $T_0=300 \text{ K}$; $I=10 \text{ } \mu\text{A}$; $\Theta=1190 \text{ K}$; $k_0=140 \text{ W}/(\text{m} \cdot \text{K})$. At the selected values of k_0 and Θ in the temperature range 200-1000 K, the thermal conductivity coefficient k lies in the range 55÷830

$\text{W}/(\text{m} \cdot \text{K})$. This corresponds to the literature data according to which k can vary from 25 to 3000 $\text{W}/(\text{m} \cdot \text{K})$ ^[25]. The results of the calculations are shown in **Figure 5**, curve 1 (curve 2 — calculation without taking into account the Nottingham effect).

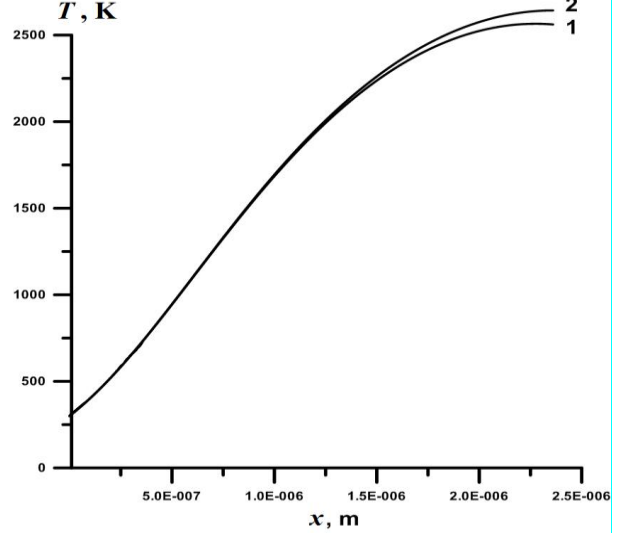


Figure 5. Temperature distribution along the axis of the carbon nanotube: 1 — taking into account (1) the Nottingham effect; 2 — without taking into account the Nottingham effect. The values of the coefficients are indicated in the text.

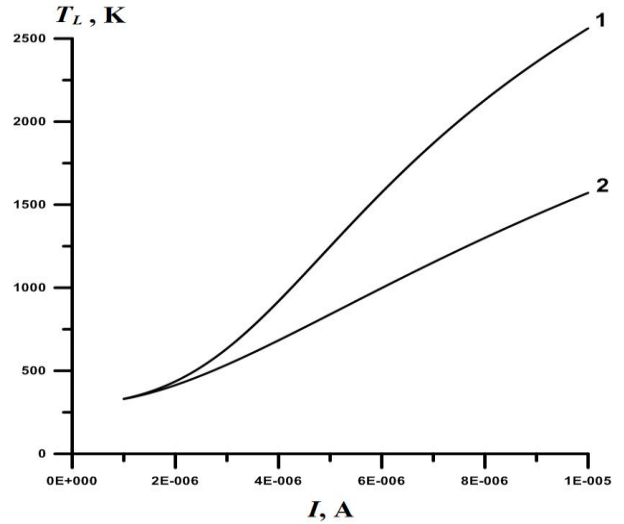


Figure 6. The temperature of the emitting end of CNTs on the value of the flowing emission current, taking into account the Nottingham effect. 1 — $k=k_0(\Theta/T)$; 2 — $k=\text{const}$. The values of the coefficients are shown in the text.

Figure 6 shows the temperature dependence of the emitting end of the CNTs (T_L) as a function of the flowing emission current, taking into account the Nottingham effect (for comparison, the curve for $k=\text{const}$ is also given there). The calculation is

made for the values of the coefficients, which are given in the text before that. The temperature of the emitting end of the CNT in the case $k=k_0$ (Θ/T) turned out to be higher than in the case $k=\text{const}$ in the whole considered range of emission currents.

The nanotube length varied from 0.5 to 4 μm when calculating the temperature. The temperature of the cold end of the nanotube contacted to the substrate was assumed to be $T_0 = 300\text{ K}$.

Equation (4) was solved for different values of the current I , and thus a dependence $T_L - T_0 = f(I)$ was obtained, where T_L is the temperature of the emitting end, as is shown in **Figure 7**.

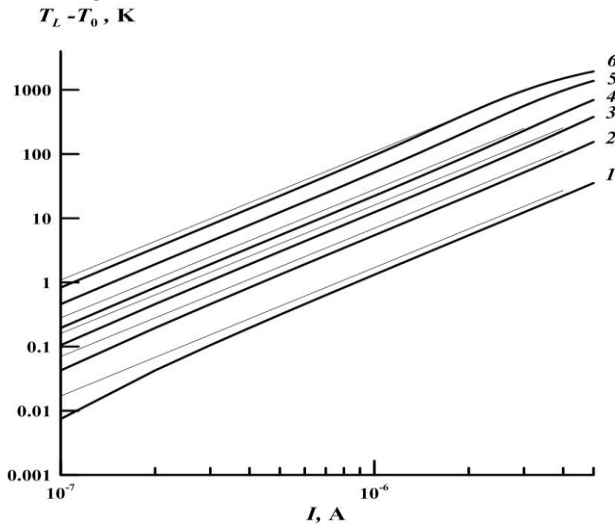


Figure 7. Dependence of the superheating temperature of the emitting end of a CNT on the flowing current for CNTs of different lengths: 1 — 0.5 μm ; 2 — 1.0 μm ; 3 — 1.5 μm ; 4 — 2.0 μm ; 5 — 3.0 μm ; 6 — 4.0 μm .

In this figure, the exact solution of Ed. (4) is compared with the approximate analytical solution obtained under the condition that there are no radiative cooling, no Nottingham effect, the thermal conductivity coefficient and the resistance of CNTs are constant^[21]:

$$T_L - T_0 = \frac{I^2 R}{2kS} L \quad (9)$$

The results of the calculations in **Figure 7** show that the simplified solution gives an overestimate value of the superheat temperature of the emitting end of the nanotube for all values of its length. A simplified solution approximates the exact solution with increasing current strength. We as-

sume that the temperature dependence of the thermal conductivity Ed. (6) is compensated by additional cooling due to the Nottingham effect. The temperature of the cathode overheating increases in proportion to the square of the emission current. The current strength of the 1 μA is a critical value in our case, exceeding which results in the appearance of thermionic emission currents and the appearance of unstable volt-ampere characteristics.

4. Results and discussion

The emission current is composed of the field and thermionic components according the electrical circuit of the current flow is shown in **Figure 2**. This current is represented by curve 3 in **Figure 3**. Field emission current is represented by curve 2. It is obvious that at the maximum values of the voltage (U_c) at which the negative resistance region starts, the currents of field-electron and thermionic emission are approximately equal. Further current growth is due to the thermionic component, and the field current decreases, while changing along curve 2.

Thus, the region of negative resistance of the voltage-current characteristic (**Figure 3**) is due to the fact that the current of thermionic emission predominates over the field emission current. The end of the nanotube is already overheated to such an extent that it can be destroyed. The voltage (U_c) and current (I_c) at which the negative resistance region starts can be considered as critical. As soon as the total current exceeds this value, the emission becomes unstable and the degradation processes begin.

It is important to estimate the conditions under which degradation of emission currents is possible. There is a conditional current limit, the excess of which causes a rapid overheating of the nanotube end and the degradation of the emission. At the boundary, the total current is equal to the sum of the currents of the field electron emission and the thermionic emission, $I = I_{TE} + I_{FE}$.

Subsequently thermionic current predominates. Therefore, as a condition for changing the emission mechanism, one can choose the equality of currents

$I_{TE} = I_{FE}$ or $I_{TE}(T) = I/2$. This condition allows us to estimate the geometric dimensions of the carbon nanotubes of the cathode at a fixed value of the flowing current at which their heating begins.

The temperature of CNT end warming up is determined by the current of thermionic emission (I_{TE}) and the geometric dimensions of the nanotube, which ultimately determine the magnitude of its electrical resistance Ed . (9). For rough estimation of the overheating temperature, it is enough to restrict ourselves to Ed . (9). The resistance of a nanotube is estimated by the formula:

$$R = \rho \frac{L}{S}, \quad \rho = R_0 \frac{S_0}{L_0} \quad (10)$$

where: — $CNTS = \pi(r^2 - r_0^2)$ cross-section area. The values of these parameters were calculated from the experiments $R_0 = 10 \text{ M}\Omega$; $S_0 = 5.5 \cdot 10^2 \text{ nm}^2$; $L_0 = 2.36 \text{ }\mu\text{m}$; $\rho = 2.33 \cdot 10^{-3} \text{ }\Omega \text{ m}$. The expression for the thermionic emission current is:

$$I_{TE} = S_{CNT} \frac{4\pi m_n^*}{h^3} (kT)^2 \exp \left[-\frac{\varphi - \sqrt{e^3 E / (4\pi \epsilon_0)}}{k_B T} \right] \quad (11)$$

where: $S_{CNT} = 2\pi r^2$ is the area of CNT emitting surface (hemisphere surface area); $m_n^* = 0.3m$ is effective mass of electron in CNT; k_B is Boltzmann constant; T is absolute temperature; ϵ_0 is electrical constant.

The conditional boundary of the transformation of a stable process to an unstable process is calculated from formulas (10) and (11). If we neglect the decrease in the height of the barrier in the formula (11) by the electric field, then the condition $I_{TE}(T) = I/2$ will be written in the formula:

$$\frac{1}{2} I = S_{CNT} A(T(L))^2 \exp \left[-\frac{\varphi}{k_B T(L)} \right] \quad (12)$$

Substituting Ed . (9) into Ed . (12), we obtain:

$$\frac{I}{S_{CNT}} = 2A \left(T_0 + \frac{I^2 \rho L^2}{2kS^2} \right)^2 \exp \left[-\frac{\varphi}{k_B \left(T_0 + \frac{I^2 \rho L^2}{2kS^2} \right)} \right] \quad (13)$$

For the case with given CNT radius r , formula (13) allows us to calculate the cross-sectional area S

and the length L , which correspond to the beginning of the appearance of the thermionic emission current (I_{TE}) for a given value of the total current I , as is shown in **Figure 8**.

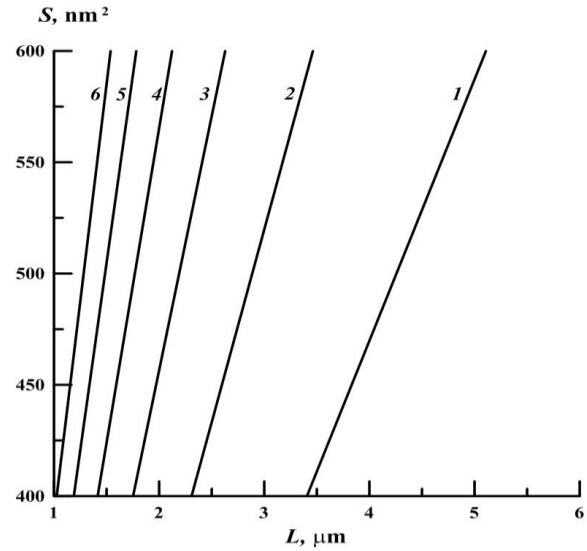


Figure 8. Dependencies for current values I: 1 — 2 μA ; 2 — 3 μA ; 3 — 4 μA ; 4 — 5 μA ; 5 — 6 μA ; 6 — 7 μA .

This figure represents several regions in the space of length — CNT area. This space is divided into regions by the curves, which are calculated for certain currents. These curves represent the boundary behind which the regime of thermionic emission and degradation of CNTs occurs. For each curve, the following statement is true: if the length of the nanotube is larger and the area is smaller, then we cross the boundary and fall into the degradation region.

With inverse relations between the parameters, namely, the length is less than the boundary one, and the area is larger, and then we fall into the region of stability of the emission.

5. Summary and conclusions

The analysis of emission processes with a single nanotube showed that when the current density increases, the end that emits electrons is heated. In this case, along with the field emission current, a thermionic emission current appears. The growth of the total current causes overheating of the end of the nanotube. This current is almost completely associated with the phenomenon of thermionic emission. At the same time, the emission process be-

comes unstable. So the temperature of overheating can exceed 1000°C, and then the nanotube begins to break down.

To analyze these processes, within the framework of this work, an algorithm has been developed that relies on numerical calculations of the field emission current and the overheat temperature. It is shown that when there is overheating, a negative resistance region occurs. At this moment, the thermionic current begins to predominate. The correlation between the current density, length and cross-sectional area of the nanotube was calculated, which allows estimating the regions in which cathode degradation can progress and the emission becomes unstable.

Acknowledgements

The work was carried out with the financial support of the Ministry of Education and Science of Russia (Project No.: 16.9007.2017/БЧ).

References

1. Bulyarskiy SV. Carbon nanotubes: Technology (in Russian). Manage Properties Application. Ulyanovsk: Strezhen; 2011. p.479.
2. Chernozatonskii LA, Gulyaev YV, Kosakovskaja ZJ, *et al.* Electron field emission from nanofilament carbon films. *Chemical Physics Letters* 1995; 233(1-2): 63–68.
3. De Heer WA, Chatelain A, Ugarte D. A carbon nanotube field-emission electron source. *Science* 1995; 270: 1179–1180.
4. Rinzler AG, Hafner JH, Nikolaev P, *et al.* Unraveling nanotubes: Field emission from an atomic wire. *Science* 1995; 269: 1550–1553.
5. Wang Q, Yan M, Chang R. Flat panel display prototype using gated carbon nanotube field emitters. *Applied Physics Letters* 2001; 78: 1294–1296.
6. Mauger M, Vu TV. Vertically aligned carbon nanotube arrays for giant field emission displays. *Journal of Vacuum Science & Technology B Microelectronics & Nanometer Structures* 2006; 24(2): 997–1003.
7. Reyes-Mena A, Jensen CH, Bard E, *et al.* Miniature X-ray tubes utilizing carbon-nanotube based cold cathodes. *Advances in X-ray Analysis* 2005; 48: 204–209.
8. Matsumoto T, Mimura H. Point X-ray source using graphite nanofibers and its application to X-ray radiography. *Applied Physics Letters* 2003; 82: 1637–1639.
9. Saito Y, Uemura S, Hamaguchi K. Cathode ray tube lighting elements with carbon nanotube field emitters. *Japanese Journal of Applied Physics* 1998; 37(3B): L346–L348.
10. Croci M, Arfaoui I, Stöckli T, *et al.* A fully sealed luminescent tube based on carbon nanotube field emission. *Microelectronics Journal* 2004; 35: 329–336.
11. Yasutomo Y, Ohue W, Gotoh Y, *et al.* Frequency mixing with a tetrode vacuum transistor. *IEEE*, 2012.
12. Sabaut L, Ponard P, Mazellier JP, *et al.* Electrostatic modeling of an in-plane gated field emission cathode. *Journal of Vacuum Science & Technology B* 2016; 34(2): 02G101.
13. Yuan X, Zhu W, Zhang Y, *et al.* A Fully-sealed carbon-nanotube cold-cathode terahertz gyrotron. *Scientific Reports* 6. 2016. Article number: 32936.
14. Paoloni C, Carlo A, Brunetti F, *et al.* Design and Fabrication of a 1 THz Backward Wave Amplifier. *Terahertz Science and Technology* 2011; 4: 1102–1110.
15. Rupesinghe NL, Chhowalla M, Teo KBK, *et al.* Field emission vacuum power switch using vertically aligned carbon nanotubes. *Journal of Vacuum Science & Technology B* 2003; 21(1): 1071–1076.
16. Eletsii AV. Carbon nanotube-based electron field emitters. *Uspekhi Fizicheskikh Nauk* 2010; 180(9): 897.
17. Bocharov GS, Eletsii AV. Theory of carbon nanotube (CNT)-based electron field emitters. *Nanomaterials* 2013; 3: 393–442.
18. Murphy EL, Good RH. Thermionic emission, field emission, and the transition region. *Physical Review* 1956; 102: 1464–1473.
19. Mayer A, Lambin Ph. Quantum-mechanical simulations of field emission from carbon nanotubes. *Carbon* 2002; 40: 429–436.
20. Sun J, Zhang Z, Hou S, *et al.* Work function of single-walled carbon nanotubes determined by field emission microscopy. *Applied Physics A* 2002; 75(4): 479–483.
21. Vincent P, Purcell ST, Journe C, *et al.* Modelization of resistive heating of carbon nanotubes during field emission. *Physical Review B* 2002; 66(7): 429–436.
22. Banerjee PK, Butterfield R. *Boundary element methods in engineering science*. London: McGRAW-HILL Book Company (UK) Limited; 1981. p.452.
23. Brebbia CA, Telles JCF, Wrobel LC. *Boundary element techniques*. Berlin, Heidelberg, New York, Tokyo: Springer-verlag; 1984. p.464.
24. Shoup TE. *Applied numerical methods for microcomputers*. Englewood Cliffs, NJ: Prentice-Hall; 1984. p.194.
25. Bocharov GS, Eletsii AV. Thermal instability of field emission from carbon nanotubes. *Technical Physics* 2007; 52(4): 498–503.
26. Bocharov GS, Eletsii AV, Sommerer TJ. Optimization of the parameters of a carbon nanotube-based field-emission cathode. *Technical Physics* 2011; 56(4): 540–545.

27. Ziman JM. Electrons and phonons. The theory of transport phenomena in solids. Oxford at the Clarendon Press; 1960. p.554.
28. Hone J, Llaguno MC, Biercuk MJ, *et al.* Thermal properties of carbon nanotubes and nanotube-based materials. *Applied Physics A* 2002; 74: 339–343.
29. Paulini J, Klein T, Simon G. Thermo-field emission and the Nottingham effect. *Journal of Physics D: Applied Physics* 1993 (Printed in the UK); 26: 1310–1315.
30. Wei W, Liu Y, Wei Y, *et al.* Tip cooling effect and failure mechanism of field-emitting carbon nanotubes. *Nano Letters* 2007; 7: 64–68.
31. Huang N, Chen J, Chen J, *et al.* Mechanism responsible for initiating carbon nanotube vacuum breakdown. *Physics Review Letter* 2004; 93: 075501.

ORIGINAL RESEARCH ARTICLE

Coal combustion residues characterization using scanning electron microscopy & energy dispersive X-ray (SEM-EDXA) analysis

Ritesh Kumar¹, Sadanand Sharma¹, Ajit Kumar¹, Charu Arora^{2*}

¹CSIR-Central Institute of Mining & Fuel Research (CIMFR), Barwa Road, Dhanbad-826001, Jharkhand, India.

²Guru Ghasi Das Vishwavidyalaya, Bilaspur-459005, Chhatisgarh, India; E-mail: charuarora77@gmail.com

ABSTRACT

The objective of the present study is to observe the surface morphology, structure and elemental composition of the ash particles produced from some thermal power stations of India using scanning electron microscopy (SEM) and energy dispersive X-ray analysis (EDXA). This information is useful to better understand the ash particles before deciding its utility in varied areas.

Keywords: Coal Combustion Residues; Characterization; XRD; SEM-EDXA; FTIR

ARTICLE INFO

Article history:

Received 24 October 2020

Received in revised form 21 November 2020

Accepted 26 November 2020

Available online 7 December 2020

COPYRIGHT

Copyright © 2020 Ritesh Kumar *et al.*

doi: 10.24294/can.v3i2.595

EnPress Publisher LLC. This work is licensed under the Creative Commons Attribution-NonCommercial 4.0 International License (CC BY-NC 4.0).

<http://creativecommons.org/licenses/by/4.0/>

1. Introduction

Power sector is the major consumer of coal in our country. With rapid industrialization, since independence and improvement in the quality of life, the demand for power has increased tremendously and this has led to the increase in the consumption of coal. The increasing population has further increased the coal consumption. India is the world's third largest producer and the fourth largest consumer of electricity. More than 51% of India's commercial energy demand is met through the country's vast coal reserves^[1]. The Indian power sector generated approximately 1160.141 BU of electricity in 2016-2017^[2,4]. During the last two decades, the growth in the power sector has been phenomenal. Of the total power generated more than 50% has been contributed by coal-fired power station^[3,4]. The electricity demand owing to increase in the population and industrialization during last one and a half decade has increased tremendously, which has led to the per-capita increase in power consumption in India to 1010 kWh in 2014-2015 and 1075 kWh in 2015-2016. The installed capacity, which was 72,320 MW in 1993-1994, has now reached 329,226 MW as on August, 2017^[5,6,7].

Coal-fired power stations still dominates the energy sector in India. India has vast reserves of thermal grade coal that is cheaply and readily available as a raw material for power generation. The estimated coal reserves as on 01.04.14 in India are 301.564 BT^[8,9,10]. The production of coal has increased from about 70 MT in early 1970s to 639.234 MT in 2015-2016^[11]. Coal that is used for power generation in the country is mostly low-grade coal containing 30–50% ash^[12,13,14]. The combustion of coal at the coal-fired power stations produces ash

residues of inorganic minerals.

Around 132 thermal power stations are there in the country that meets 51% of India's commercial energy demand. These thermal power stations produce around 150MT of coal combustion residues (CCRs) per year that is causing great environmental concern in the form of air, water and land pollution besides its proper handling and disposal^[3]. Disposal of such a huge amount of CCRs craves for huge tract of land besides having several environmental implications in the disposal environment. In country like India, where land resources is very limited, proper management of CCRs is the need of the hour not only in our country but also throughout the world and all these requires proper understanding of CCRs through its characterization study.

Mostly two types of ashes namely, fly ash and bottom ashes are produced by thermal power stations in India. Fraction that tries to escape along with flue gas, are trapped by electrostatic precipitators and mechanical dust collectors and is referred as fly ash. This constitutes about 80 percent of the ash produced. The other fraction collects at the bottom of the furnace and is named as the bottom ash. This is coarser in nature and constitutes about 20 percent of the ash produced. The two ashes in the wet system of disposal (as practiced in our country by most of the coal based thermal power plants) are made into slurry form and pumped to the disposal area especially made for this purpose. The ash in such disposal pond is known as pond ash.

Table 1. Status of world energy at the end of 2016^[18] (BP, 2017)

	2016	Change 2016 over 2015 (%)
Electricity generation (TWH)	24816.4	2.2
Coal		
Reserves (MT)	1139331	-
Production (MT)	7460.4	-6.5
Production (MT of oil equivalents)	3656.4	-6.2
Consumption (MT of oil equivalents)	3732.0	-1.7

Table 2. Year-wise coal consumption, power generation and generation growth in India (2003-2004 to 2013-2014)^[19,20,21,22]

Year	Coal Consumption (Million Tonnes)	Generation (BUs)	Generation Growth (%)
2003-2004	-	558.30	-
2004-2005	278.00	587.40	5.21
2005-2006	281.00	617.50	5.12
2006-2007	302.00	662.50	7.29
2007-2008	330.00	704.50	6.34
2008-2009	355.00	723.80	2.74
2009-2010	367.00	771.551	6.60
2010-2011	387.00	811.143	5.13
2011-2012	417.56	876.887	8.11
2012-2013	545.60	912.056	4.01
2013-2014	489.40	967.150	6.04
2014-2015	530.40	1048.673	8.43
2015-2016	545.90	1107.822	5.64
2016-2017	-	1160.141	4.72
2017-2018	-	1229.400 (Target)	5.97

The major challenge before the nation is to effectively utilize these coal combustion residues in bulk and that too in environmentally benign manner. The increasing number of thermal power stations and also the ever increasing population will add more pressure for immediate utilization. The ash utilization in India in 1992-1993 was 2–3%^[15],

which has now increased to 60.97% of CCRs as per the latest report^[16]. However, the percentage of ash utilized is still low as compared to other developed countries of the world where utilization is close to 100%^[17]. Though in our country the situation has changed since last one and a half decade, we have to go a long way to fulfill the promise of 100% uti-

lization.

Table 1 shows the status of world energy at the end of 2016. **Table 2** and **Table 3** show the year-wise coal consumption and power generation in India from 2003-2004 to 2013-2014 and per-capita electricity consumption in India from 2005-2006 to 2015-2016, respectively. **Table 4** shows the per-capita consumption of electricity by leading countries of the world. **Table 5** shows the India's CCRs utilization scenario. Similarly, **Table 6** provides the data on CCRs utilized by the leading

countries of the world. **Figure 1** shows year-wise power generation in BUs and coal consumption in MT in India.

This paper provides a detailed characterization study of CCRs from Indian thermal power station. The paper covers SEM-EDXA analysis of the CCR samples. The actual aim of this paper is to understand CCRs suitability in various applications using the characterization data so that the material can be used in an environmentally friendly manner.

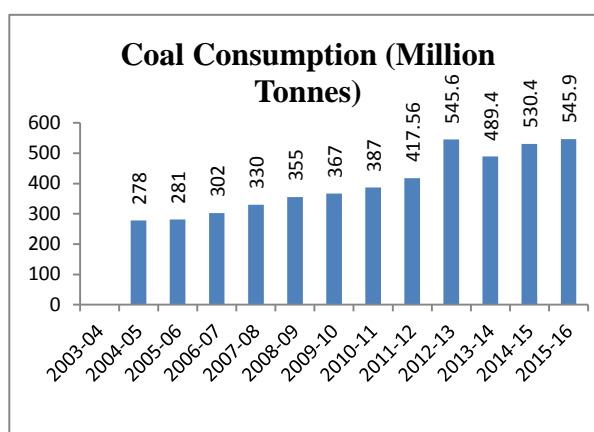
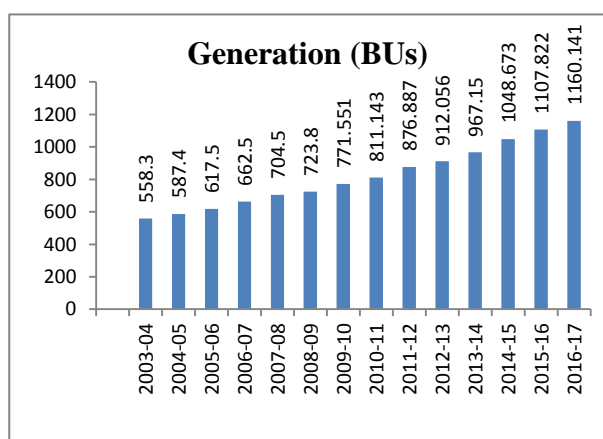


Figure 1. Year-wise power generation (BUs) and coal consumption (MT) in India.

Table 3. Year-wise per-capita electricity consumption in India (2005-2006 to 2015-2016)^[23,24]

Year	Consumption (kWh)
2005-2006	631
2006-2007	673
2007-2008	717
2008-2009	734
2009-2010	779
2010-2011	819
2011-2012	884
2012-2013	914
2013-2014	957
2014-2015	1010
2015-2016	1075

Table 4. Comparative per-capita consumption of electricity (kWh)^[25,26]

Countries	Consumption (kWh) for 2013
Canada	15520
USA	12987
Australia	10067
Japan	7836
France	7382
UK	5409
World	3026
India	957

Table 5. Year-wise CCRs utilization in India (1993-1994 to 2005-2006)

Year	Utilization (%)
1992-1993	2-3%
2002-2003	22.68
2003-2004	29.39
2004-2005	38.04
2005-2006	45.69
2006-2007	50.86
2007-2008	53.00
2008-2009	57.11
2009-2010	62.60
2010-2011	55.79
2011-2012	58.48
2012-2013	61.37
2013-2014	57.85
2014-2015	54.31

2. Materials and methods

2.1 Selection of thermal power stations

For assessing the environmental characteristics of coal combustion residues (CCRs) five thermal power stations, viz. three of Damodar Valley Corporation (DVC), namely, Bokaro Thermal Power Station (BTPS), Chandrapura Thermal Power Sta-

tion (CTPS) and Durgapur Thermal Power Station (DTPS), one fluidised bed combustion (FBC), Plant of Tata Iron & Steel Company (TISCO) and one of Fertilizer Corporation of India Ltd. (FCI), Sindri unit were chosen. All the thermal power stations are either located on the banks of Damodar river or in its immediate vicinity in the states of Jharkhand and West Bengal.

These thermal power stations were chosen for the following reasons:

- These form the life-line of an industrial belt in Damodar river basin
- Power plants and the ash ponds are close to surface water bodies.
- There is probability of surface and ground water contamination due to leaching of trace elements from the ash ponds of these plants.

Also, these thermal power stations were easily accessible and it was possible to get desired facilities for the studies. **Figure 2** shows the locations of

the power stations under study along river Damodar. Similarly, **Table 7** gives the composition of coal being used at different thermal power stations.

Table 6. Utilization of fly ash by various countries^[15]

S.No.	Country	Utilization (%)
1	Australia	40
2	Canada	40
3	China	35
4	Czechoslovakia	40
5	Denmark	85
6	France	70
7	Germany FR	85
8	Greece	45
9	Hungary	50
10	India	41
11	Israel	80
12	Japan (a)	40
13	Netherlands	100
14	Poland	100
15	South Africa	35
16	U.K.	60
17	U.S.A	35

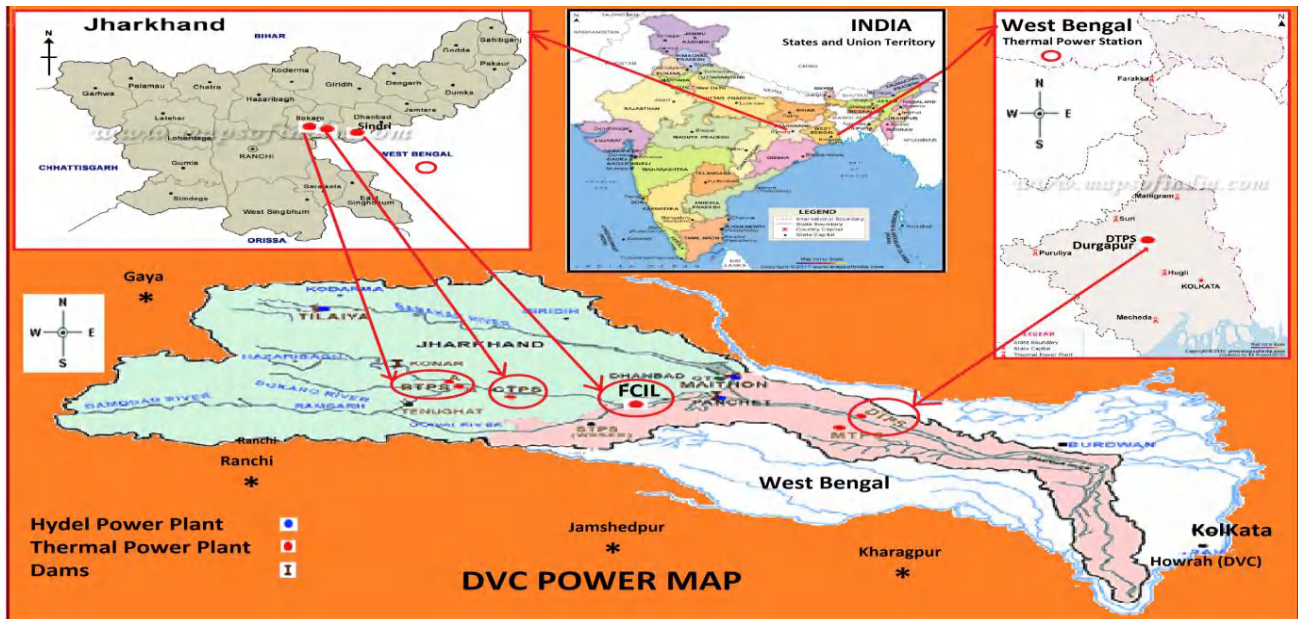


Figure 2. Location of Bokaro thermal power stations along the River Damodar.

Table 7. Composition of coal being used at different thermal power stations^[27]

Parameters	BTPS	CTPS	DTPS	FBCP	FCIL
Fixed carbon (%)	36.28–47.77	41.75	55.30	26.67	45–47
Volatile matter (%)	15.8–18.12	16.20	24.50	-	16–19
Moisture (%)	0.9–1.11	0.60	2.80	1.1	0.5
Ash (%)	34.23–40.25	41.45	27.40	65	30–35
Gross calorific value (kcal/kg)	4670–4970	4665	5560	2200	4800

2.2 Sampling

Fly ash (FA) and bottom ash (BA) samples were collected on five different days over a week and a final homogenized sample for each of the fly ash and bottom ash were prepared by mixing the appropriate portions. Similarly, pond ash samples were collected from the ash ponds site from five different locations on five different days over a week and a final homogenized sample was prepared mixing appropriate portions. The CCR samples after coning and quartering method were then taken for characterization studies adopting analytical methods.

2.3 Scanning electron microscopy & energy dispersive X-ray analysis

The scanning electron microscopy (SEM)^[29,30] allows high-level magnifications, which can be used for studying morphology of the sample of finer materials. It uses a focused electron beam to scan small areas of solid sample surfaces. Secondary electrons are emitted from the sample and are collected to create an area map of the secondary emissions. This secondary emission is very much dependent on the surface characteristics and so the area obtained is a magnified image of the sample. This technique is also referred to as energy dispersive X-ray analysis (EDXA). The back-scattered electrons also produce X-rays and the same can be utilized by many instruments for the qualitative compositional analysis of microscopically small portions of the sample. This technique is also referred to as energy dispersive X-ray analysis (EDXA). The sample requirement for the SEM analysis is that the solid samples, viz. thin films, powder, fibers and bulk materials should be vacuum compatible.

The principle of working of the instrument is that an electron beam, accelerated at 25 KV energy, is generated at electron gun. The electron beam is passed through various electro-magnetic lenses. It first passes through condenser lens forming an electron beam spot. The fine electron beam is then focused by objective lens. The focused electron beam is deflected by beam deflection coil throughout the

specimen. As soon as the focused electron beams falls on the specimen, the secondary electron beams are emitted as per the sample topography. The secondary electrons are processed to secondary electron image in the display unit through a secondary electron detector assembly.

The scanning electron microscopic studies were carried out using Model S-415A (**Figure 3**), Hitachi Instruments Ltd., Tokyo, Japan. The fine powders are sonicated in test tube with methanol solvent in a sonicator machine for 1 hour. The fine particles were then suspended in the medium. It was then pipetted out through a pipette in a cover slip and dried. After properly drying, it was subjected to gold coating to eliminate the charging effect of the electron beam during SEM observation. This was done in an ion coater (Model 1132, Eiko Engineering, Japan) by Sputtering Technique at a 1400V D.C., 8-10 mA current for 3 minutes. After gold coating, it was placed in the evacuation chamber of SEM. After evacuation, the electron beam was generated at 25 KV energy and the secondary electron Ashi Pentax Camera was attached to the instrument to record images and the photomicrographs were taken one by one.



Figure 3. Scanning electron microscope, Hitachi Instruments Ltd., Japan, Model 415A.

2.4 Results and discussion

The results of the characterization of coal combustion residues (CCRs) from five thermal power stations, viz. BTPS, CTPS, DTPS, FBCP and FCI, Sindri for assessing their characteristics for various uses as determined by instrumentation techniques such as SEM-EDXA is discussed below.

3. SEM-EDXA

The morphological features of the leached and unleached CCR samples were examined with the help of scanning electron microscope using scanning electron microscopy (SEM) technique. **Table 8** gives the observation made with respect to SEM studies of CCR samples under study. These are also shown in **Figure 4** to **Figure 8**. The study of the micrographs of the unleached CCR samples in general indicated that CCR consisted primarily of spherical particles with nodules present on it. The particles were of different sizes and ranged from 1 μ to 100 μ . Similarly, study of the micrographs of leached CCR samples clearly shows the leaching pattern that has taken place. The particles in the leached samples lacked agglomeration and were more dispersed than one can observe in the case of unleached samples. Thus, one can conclude that the surface film or the irregularities caused the unleached particles to agglomerate.

Figure 9 shows few micrographs of the leached CCR samples. One can easily observe the leaching phenomena that have taken place and that the surfaces of the leached particles were observed to be smoother. It means that the material residing on the surface has been washed away during the leaching. Surficial element mostly present included

alkali and alkaline earth metals, i.e. sodium, potassium, calcium and magnesium. As these got washed away due to the first flush phenomenon, their presence in the leached samples also decreased considerably. Decrease in concentration of these elements with time can be very well observed from the plot of the open column percolation experiment results for these elements.

Some of the particles on the leached samples were found distorted as can be seen from the micrographs of the leached samples. Distortion of particle surface is due to dissolution or disruption of the surface, making the wall thinner and thinner and finally rupturing the wall.

As is pointed out, the particles are mostly spherical in shape and they are either hollow spheres commonly known as cenospheres or solid spheres or may be containing many smaller spheres within a sphere known as plerosphere. All three can be seen from the micrographs. Cenospheres and plerospheres are present in very low amount. Some spongy morphology can also be noticed from the micrographs. A point of special importance is the fact that most of the particles are found to be of spherical nature. Due to being spherical mixed with cement, it can add workability to cement concrete mix. Being spherical and hollow can be used as filler in paints and so on.

Table 8. Summary of SEM study of CCR samples from a few thermal power stations of India

Plant	Samples	SEM (Observations)
PS	FA#A; FA#B; BA#A; BA#B; PA	<ul style="list-style-type: none"> ● Mostly spherical in shape with size varying from less than 1 micron to 100 micron. ● Particles were found mostly spherical in shape with nodules present on it. ● Some cenospheres could also be seen from the micrographs.
CTPS	FA#1; FA#2; BA#1; BA#2; PA	<ul style="list-style-type: none"> ● A few plerospheres could also be seen from the micrographs. ● Cenospheric particles show frequent bursts which are inductive of chemical activity having occurred within them.
DTPS	FA; BA; PA	<ul style="list-style-type: none"> ● Surfaces of some particles show extensive mechanical damage caused by impactation. ● Small size particles were seen sticking to the larger spherical particles possibly on account of the convexity of the surfaces.
FBCP	FA; PA	<ul style="list-style-type: none"> ● Leached particles were observed to be smoother. This shows the washout of the elements residing on the surface with time. Plot of OPCE also shows this decreasing trend.
FCIL	S1; S2; S3; S4	<ul style="list-style-type: none"> ● Some spongy morphology could also be seen from the micrographs.

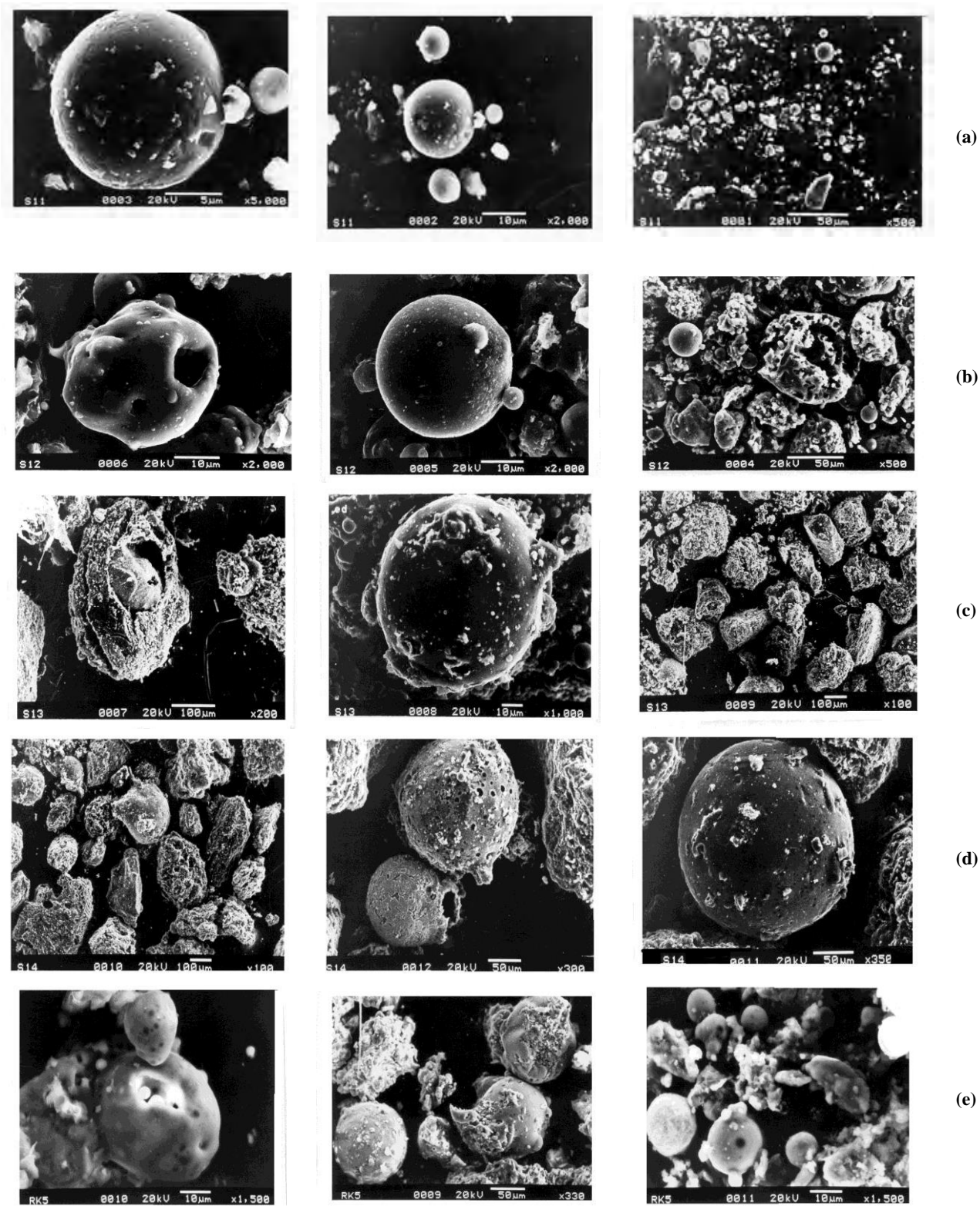


Figure 4. Scanning electron micrographs of BTPS (a) FA#A; (b) FA#B; (c) BA#A; (d) BA#B and (e) PA.

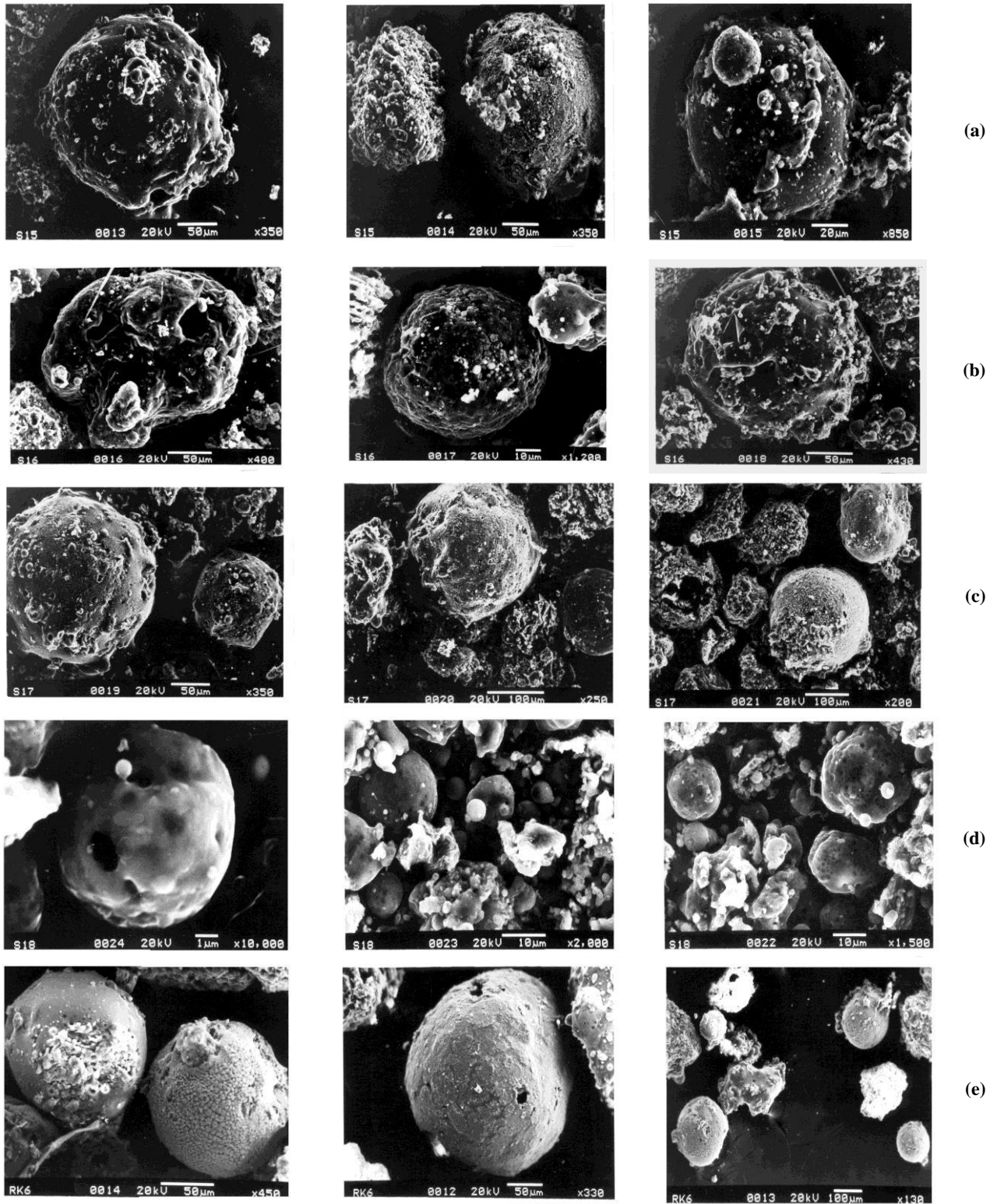


Figure 5. Scanning electron micrographs of CTPS (a) FA#1; (b) FA#2; (c) BA#1; (d) BA#2 and (e) PA.

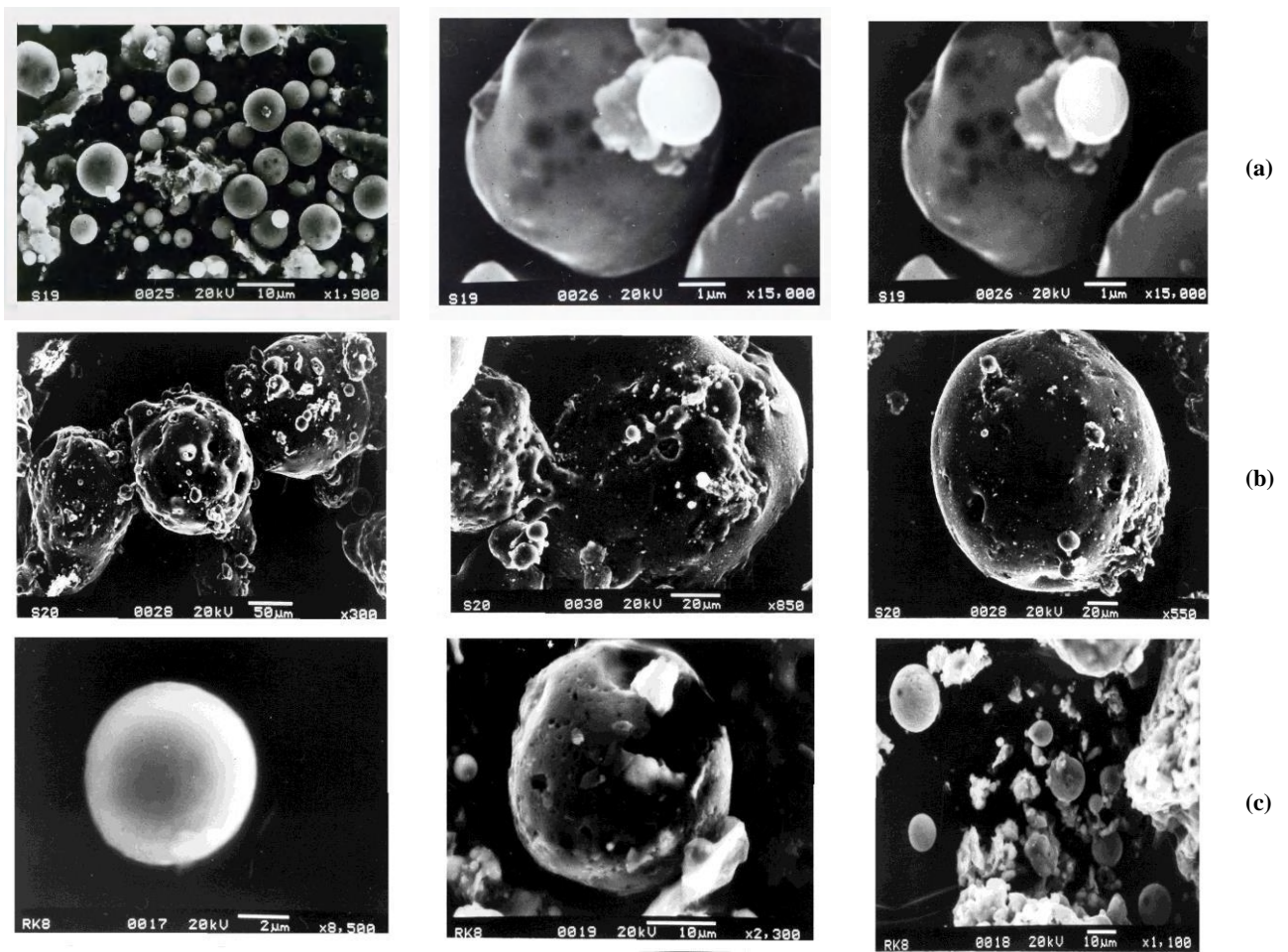


Figure 6. Scanning electron micrographs of DTPS (a) FA; (b) BA and (c) PA.

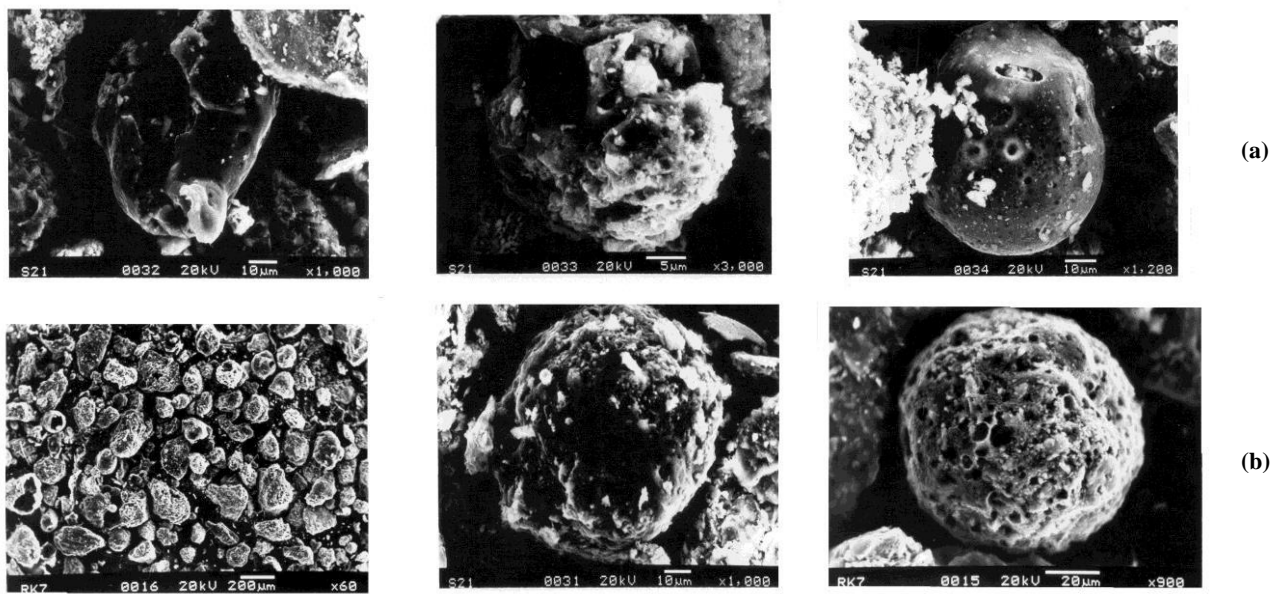


Figure 7. Scanning electron micrographs of FBCP (a) FA and (b) PA.

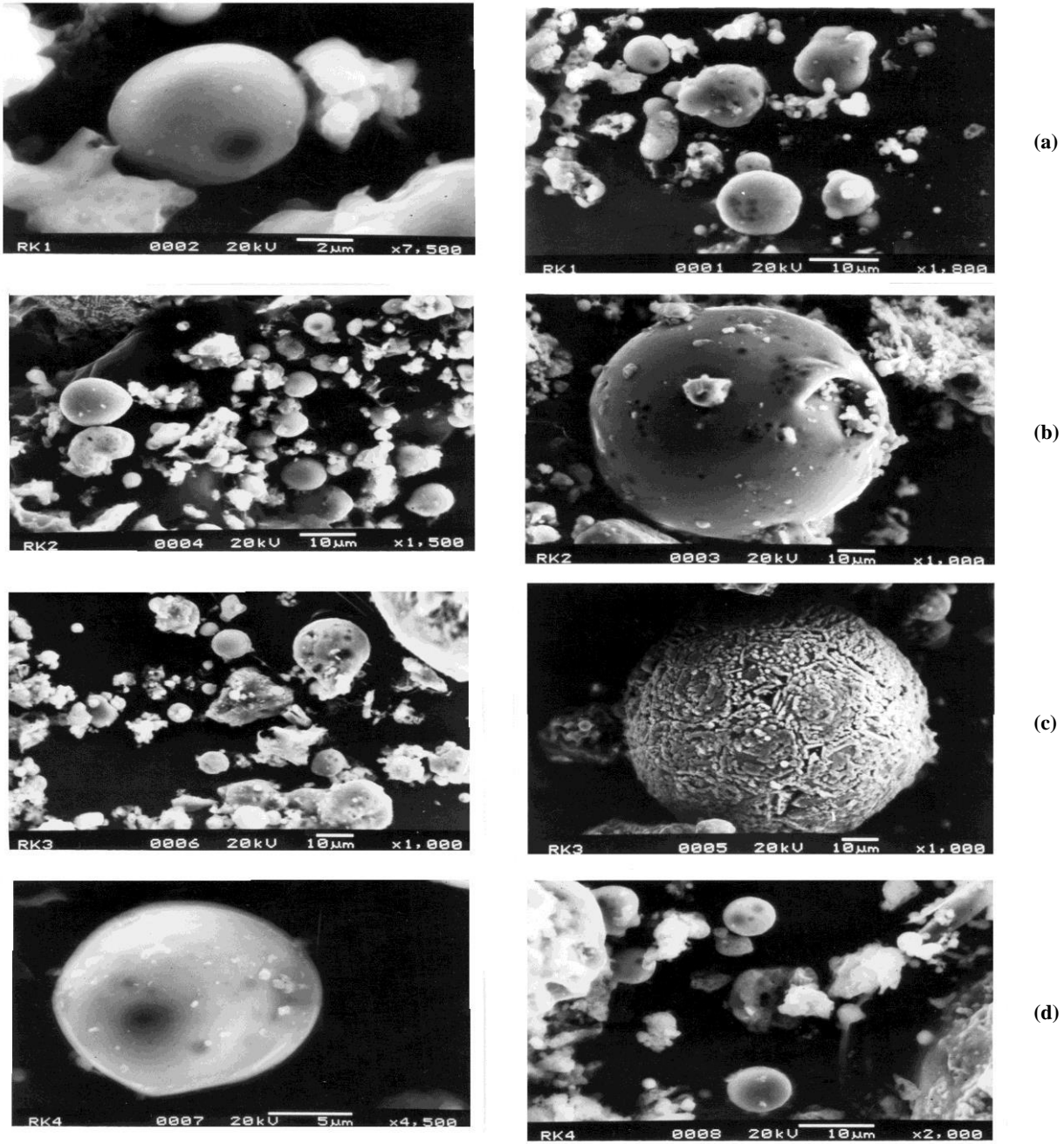


Figure 8. Scanning electron micrographs of FCI (a) S1; (b) S2; (c) S3 and (d) S4.

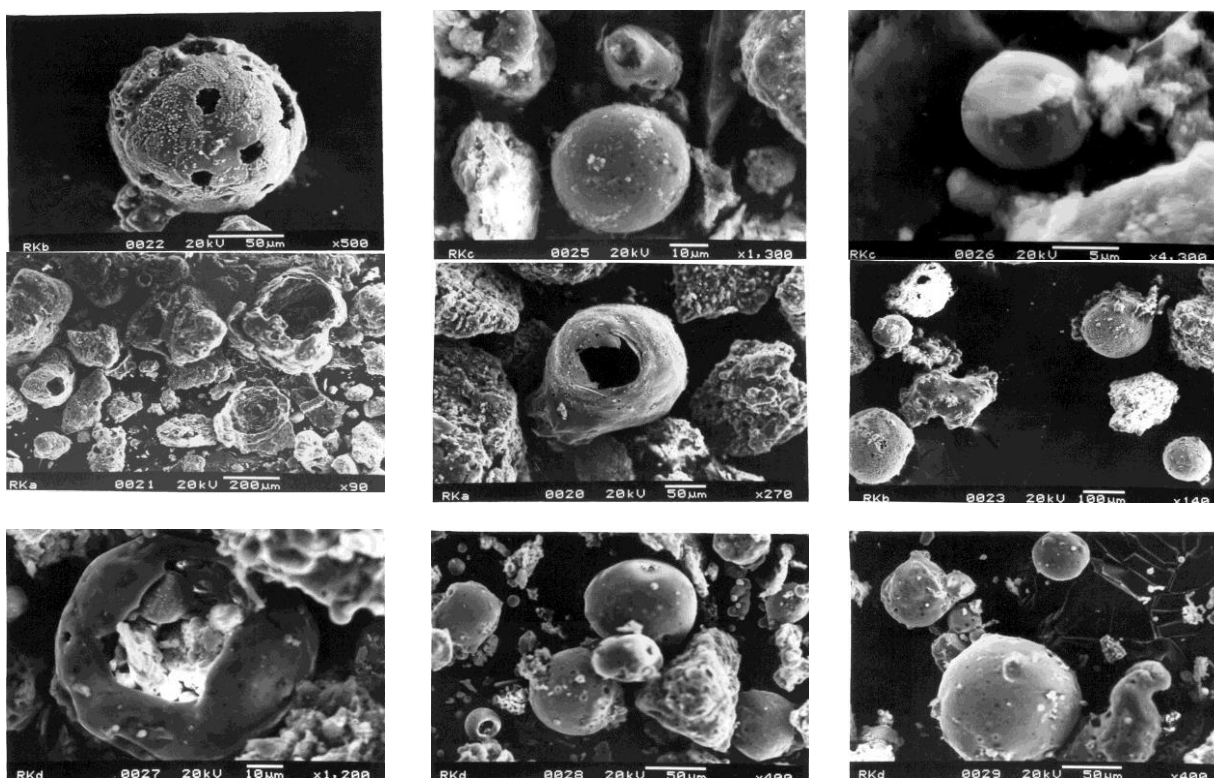


Figure 9. Scanning electron micrographs of CCR samples after leaching.

The observations of EDXA analysis are given in the Table 9. This study was performed to determine the trace element contents in the CCR samples. The study shows

that the CCR samples are typically formed of Si-Al-Fe system with traces of sodium, potassium, calcium, magnesium, sulphur and titanium.

Table 9. Summary of EDXA of CCR samples from a few thermal power stations

Plant	Samples	Si	Al	Fe	Na	K	Ca	Mg	S	Ti
BTPS	FA#A	25.97	14.85	3.34	2.52	1.63	0.62	0.12	0.02	0.97
	FA#B	21.67	14.56	3.75	6.35	1.42	0.89	0.92	0.06	2.16
	BA#A	25.88	17.36	2.07	1.93	1.27	0.09	0.02	-	1.32
	BA#B	26.40	15.93	1.36	1.10	1.66	0.32	0.64	-	1.04
	PA	23.20	12.20	8.54	4.36	1.16	0.37	0.90	0.21	1.06
CTPS	FA#1	27.35	14.54	5.09	0.01	1.11	0.44	0.05	0.72	0.91
	FA#2	25.66	16.94	2.92	-	1.16	0.15	0.50	0.02	0.53
	BA#1	27.34	14.70	2.78	0.84	1.15	0.31	0.21	0.28	1.61
	BA#2	22.90	15.90	7.28	1.41	1.23	0.90	0.64	-	1.69
	PA	24.64	14.88	4.25	0.65	1.06	0.41	1.01	0.38	0.79
DTPS	FA	25.73	13.36	3.11	2.78	1.62	0.71	0.86	-	1.42
	BA	24.87	12.49	4.81	4.73	1.31	1.51	1.13	0.15	0.06
	PA	18.05	22.62	1.01	1.43	0.75	0.34	0.46	0.05	1.03
FBCP	FA	24.97	13.11	4.63	1.77	2.61	2.77	0.80	0.51	1.34
	PA	22.27	19.64	2.31	0.35	1.28	0.78	0.63	0.59	1.66
FCI	S1	26.10	14.28	1.98	-	1.27	0.31	0.55	-	1.39
	S2	21.51	13.17	11.91	-	0.94	0.50	0.23	-	1.14
	S3	25.78	15.59	2.84	-	1.45	0.72	0.25	-	1.16
	S4	26.59	14.40	2.54	-	1.26	0.35	0.65	-	1.73

4. Conclusion

The SEM studies of the CCRs have shown that CCRs consisted primarily of spherical particles with nodules present on it. The particles varied in size from less than 1 micron to 100 micron. The particles consisted of cenospheres (hollow spheres), solid spheres and plerospheres (spheres within a sphere). Spongy morphology and a small amount of angular shaped particles were also seen. This was due to the presence of unburned carbon and other minerals. Being spherical and hollow these particles can be used as filler in paints and so on. On the other hand, the SEM studies of the CCR particles after leaching have clearly shown the leaching pattern that has taken place. The particles after leaching lacked agglomeration compared to the original particles. Some of the particles were also observed distorted in shape while walls of some of the particles were found ruptured. This distortion and rupturing may be accounted due to the dissolution of the surficial elements making the wall of the sphere thinner and thinner and finally the wall ruptures.

List of Abbreviations

CCRs	Coal Combustion Residues
DTPS	Durgapur Thermal Power Station
BTPS	Bokaro Thermal Power Station
CTPS	Chandrapura Thermal Power Station
TISCO	Plant of Tata Iron & Steel Company
FCIL	Fertilizer Corporation of India Limited
DVC	Damodar Valley Corporation
SEM	Scanning Electron Microscopy
EDXA	Energy Dispersive X-Ray Analysis
BP	British Petroleum
CEA	Central Electricity Authority
TEDDY	Teri Energy Data Directory and Yearbook

References

1. Thermal Power Plants in India. Retrieved from: <http://cbrienvis.nic.in/Thermal%20Power%20Station%20in%20India%202016.pdf>.
2. Power Sector at a Glance All India. Retrieved from: <http://powermin.nic.in/en/content/power-sector-glance-all-india>.
3. TEDDY (TERI Energy Data Directory & Yearbook). Annual Report 2015/2016.
4. Central Electricity Authority (CEA, 2017). Retrieved from: <http://www.cea.nic.in/reports/monthly/executive-summary/2017/exe-summary-06.pdf>.
5. Electricity Sector in India. Retrieved from: https://en.wikipedia.org/wiki/Electricity_sector_in_India.
6. CEA Report 2014/2015, 2016/2017. Retrieved from: www.cea.nic.in.
7. TEDDY (TERI Energy Data Directory & Yearbook). Annual Report 2016/2017.
8. TEDDY (TERI Energy Data Directory & Yearbook). Annual Report 2014/2015.
9. Coal Reserves (As on 01.04.14). Retrieved from: <https://www.coal.nic.in/content/coal-reserves>.
10. Coal Reserves in India as on 01.04.2014. Retrieved from: <http://www.mcl.gov.in/Others/ecoalfields.php>.
11. Provisional Coal Statistics 2015-2016. Retrieved from: <http://www.coalcontroller.gov.in/writereaddata/files/Provisional%20Coal%20Statistics%202015-16.pdf>.
12. Kumar V. Management of fly ash in India: A perspective. 3rd International Conference — Fly Ash Utilization and Disposal, February 19-21, 2003, New Delhi, India.
13. Mishra UC. Environmental impact of coal industry and thermal power plants in India. *Journal of Environmental Radioactivity* 2004; 72(1-2): 35-40.
14. Zamuda CD, Sharpe MA. A case for enhanced use of clean coal in India: An essential step towards energy security and environmental protection. Workshop on Coal Beneficiation and Utilization of Rejects, Ranchi, Jharkhand, India, August 22-24, 2007.
15. Kumar V, Mathur M. Fly ash in roads and embankments. National Seminar and Business Meet in Use of Fly Ash in Roads and Embankments, Allahabad, June 3-15, 2005.
16. Fly ash scenario in India. Retrieved from: <http://cbrienvis.nic.in/flyashscenario.html>.
17. CEA (Central Electricity Authority). Annual Report, 2015-2016. Retrieved from: www.cea.nic.in.
18. BP, 2017; BP Statistical review of World Energy 2017. Retrieved from: <http://www.bp.com/content/dam/bp/en/corporate/pdf/energy-economics/statistical-review-2017/bp-statistical-review-of-world-energy-2017-full-report.pdf>.
19. TEDDY (TERI Energy Data Directory & Yearbook). Annual Report 2003/2004, 2004/2005, 2005/2006, 2009, 2014/2015, 2015/2016.
20. CEA (Central Electricity Authority). Annual Report 2011/2012, 2012/2013, 2014/2015. Retrieved from: www.cea.nic.in.
21. Executive Summary 2017; Retrieved from: <http://www.cea.nic.in/reports/monthly/executivesummary/2017/exe-summary-01.pdf>.
22. Power Sector at a Glance, 2017; Retrieved from: <http://powermin.nic.in/en/content/power-sector-glance-all-india>.

- ce-all-india.
23. Garg P. Energy scenario & vision 2020 in India. *Journal of Sustainable Energy & Environment* 2012; 3: 7–17.
 24. Annual Report 2011/2012, 2012/2013, 2014/2015. CEA (Central Electricity Authority). Retrieved from: www.cea.nic.in.
 25. Electric power consumption (kWh per capita). Retrieved from: <http://data.worldbank.org/indicator/EG.USE.ELEC.KH.PC>.
 26. Dubbudu R. India's per capita electricity consumption lowest among BRICS nations. May 10, 2016. Retrieved from <https://factly.in/indias-per-capita-electricity-consumption-lowest-among-brics-nations/>.
 27. Kumar R. Environmental assessment of coal combustion residues from a few thermal power stations [PhD thesis]. Dhanbad: Indian School of Mines; 2009.
 28. Pungor E. A practical guide to instrumental analysis. CRC Press, Inc; 1995.
 29. Goldstein J, Newbury ED, Echlin P, *et al.* Scanning electron microscopy and X-ray microanalysis: A text for biologists, material scientists and geologists. 2nd Ed. Plenum US; May 31, 1992.
 30. Goldstein J, Newbury DE, Michael JR *et al.* Scanning electron microscopy and X-ray microanalysis. 3rd Ed. New York: Plenum Press; 2003.
 31. Smith B. Infrared spectral interpretation. London, New York, Washington DC: CRC Press; 1999.
 32. Smidt E, Bohm K, Schwanninger M. The application of FT-IR spectroscopy in waste management. Boku University of Natural Resources and Life Sciences, Vienna, Austria. 2007. Retrieved from: <http://cdn.intechopen.com/pdfs/14634.pdf>.

ORIGINAL RESEARCH ARTICLE

Relative stability of planar clusters B_{11} , B_{12} , and B_{13} in neutral- and charged-states

Levan Chkhartishvili

Department of Engineering Physics, Georgian Technical University, Tbilisi, Georgia;

E-mail: chkharti2003@yahoo.com

ABSTRACT

Theoretically, within the diatomic model, the relative stability of most abundant boron clusters B_{11} , B_{12} , and B_{13} with planar structures in neutral, positive and negative charged-states is studied. According to the specific (per atom) binding energy criterion, B_{12}^+ (6.49 eV) is found to be the most stable boron cluster, while $B_{11}^- + B_{13}^+$ (5.83 eV) neutral pair is expected to present the preferable ablation channel for boron-rich solids. Obtained results would be applicable in production of boron-clusters-based nanostructured coating materials with super-properties such as lightness, hardness, conductivity, chemical inertness, neutron-absorption, etc., making them especially effective for protection against cracking, wear, corrosion, neutron- and electromagnetic-radiations, etc.

Keywords: Cluster; Charge State; Specific Binding Energy; Diatomic Model; Relative Stability; Clusters-based Coating Material; Boron

ARTICLE INFO

Article history:

Received 12 June 2020

Received in revised form 4 July 2020

Accepted 7 July 2020

Available online 20 July 2020

COPYRIGHT

Copyright © 2020 Levan Chkhartishvili.

doi: 10.24294/can.v3i2.761

EnPress Publisher LLC. This work is licensed under the Creative Commons Attribution-NonCommercial 4.0 International License (CC BY-NC 4.0).

<http://creativecommons.org/licenses/by/4.0/>

1. Introduction

Boron-clusters-based nanostructured coating materials due to their super-properties such as lightness, hardness, conductivity, chemical inertness, neutron-absorption, etc. can serve for effective protection against cracking, wear, corrosion, neutron- and electromagnetic-radiations, etc.^[1,2]. This makes boron clusters B_n , $n=1,2,3,\dots$, interesting to be investigated in details.

Summarizing experimental and theoretical data available in the literature on all-boron nanomaterials (e.g. see our overviews on subject^[3-5]), one can conclude that, according to the specific (per constituting atom) binding energy ε criterion, ultra-small, with $n \leq 20$, boron clusters prefer (quasi)planar structures, while at higher n , they should be wrapped first into cylinders and then into spheres forming boron nanotubes or boron fullerenes, respectively. In (quasi)planar clusters, ε increases with n because of increasing in mean coordination number of constituent atoms. Within the initial approximation, specific binding energy of boron clusters is expected to be almost saturated around $n \geq 10$. But, when the polarity deal into the bonding — commonly characteristic of structures of identical atoms with differently coordinated atomic sites — is taken into account, there is expected a weak maximum instead. In general features, the experimental mass-spectra fits these theoretical findings. However, formation probability peak is well-pronounced for species B_{11} , B_{12} , and B_{13} . Naturally,

such a behavior is related not only to the energy-factor, but mainly to the process kinetics. Usually, boron clusters are formed by the ablation of elemental boron or boron-rich solid materials, main structural motifs of which are slightly deformed regular icosahedra of boron atoms B_{12} ^[6].

Present paper aims to theoretically study the relative stability of most abundant boron clusters B_{11} , B_{12} , and B_{13} with (quasi)planar structures in different charged-states.

2. Method of calculations

In clusters of identical atoms, binding energy per atom, i.e., specific binding energy, serves for the key factor determining their relative stabilities and, consequently, concentrations of clusters with different numbers of atoms in the products of ablation of corresponding solid materials.

Based on various ab initio methods specific binding energy and some other important physical characteristics of boron clusters were numerically calculated by Boustani *et al.* (summarizing of these studies see in the study of Boustani^[7]) and some other teams (see above cited reviews and references therein). But, more vividly these species can be described based on the diatomic model. It should be noted that such model-based approach provides quite good quantitative results as well.

The application of the Fermi's old diatomic model^[8] to the multi-atomic structures is based on the property of interatomic bonding to be saturated. In the initial, i.e., pair interactions, approximation the binding energy of a structure simply equals to the sum of energies of interactions between neighboring atoms. Based on the pair interactions approximation, microscopic theory of expansion and its generalization to the periodical structures allow correct estimation of the thermal expansion coefficient for number of crystalline substances^[9]. Despite its simplicity, the diatomic model is still successfully used to calculate anharmonic effects in solids^[10]. An analogous approach was used by us to explain isotopic effects of thermal expansion and melting in all-boron lattices^[11-15].

Suppose that the index $i = 1, \dots, n$ numbers the atoms constituting cluster of n atoms, and C_i are their coordination numbers, respectively. In the initial approximation, binding energies between each pair of adjacent atoms E_0 are equal, and it turns out that:

$$\varepsilon \approx \frac{E_0}{2n} \sum_{i=1}^{i=n} C_i \quad (1)$$

Here, the factor $1/2$ is introduced to correct the double sum which includes every pair of neighboring atoms twice. We used approximated formula (1) to estimate ground-state binding energy of all-boron nanostructures, mainly, boron nanotubes^[16-18].

However, clusters are finite structures of atoms and, consequently, coordination numbers of sites at center are higher than that at periphery. This leads to the redistribution of the outer valence shell electrons and, as a result, differences between binding energies of neighboring atomic pairs. Note the report^[19] on high-pressure experiments and ab initio evolutionary crystal structure predictions that explore the structural stability of boron under pressure and reveal a partially ionic high-pressure boron phase.

Our formulation of the first approximation to the diatomic model theory takes into account corresponding polarity of the bonds. In case of identical constituent atoms, it is obvious to assume that these electrons between the atoms are divided proportionally to their coordination numbers. This implies that the atoms develop non-zero effective static atomic charges with charge numbers Z_i determined from the relation:

$$\frac{nZ_i}{V} = 1 - \frac{nC_i}{\sum_{j=1}^{j=n} C_j} \quad (2)$$

respectively, Here V is the total number of the outer valence shell electrons in the atoms constituent cluster.

Thus, the binding energy per atom in the first approximation, i.e., including correction related to the interatomic bonds polarity, is:

$$\varepsilon \approx \frac{1}{2n} \sum_{i=1}^{i=n} (E_0 C_i - E_1 Z_i \sum_{k_i=1}^{k_i=C_i} Z_{k_i}) \quad (3)$$

Where the index $K_i = 1, \dots, C_i$ numbers the nearest neighboring atoms of i -atoms, respectively;

$$E_1 = \frac{e^2}{4\pi\varepsilon_0 d} \quad (4)$$

is the energy-dimension parameter (e and ε_0 are elemental charge and electric constant, respectively); and d is the initial bonds length in the equilibrium.

In our previous studies^[20-23], relations (2), (3), (4) are used to estimate effective static atomic charges, dipole moment, and specific binding energy in the boron planar clusters.

Further improvement of this approximation means determination of the equilibrium bond length in the first approximation as well. It can be done by the minimization of the system potentials energy including bond length-dependent vibrational and electrostatic interaction energies^[24].

Within the frame of the diatomic approach, further refinement of the clusters' binding energy and other ground-state parameters can be achieved by abandoning the requirement for equality of all the bond lengths. In another study of mine^[25], a general theoretical frame for further studying is provided. Finally, we have got a set of linear equations determining not precisely planar, but quasi-planar equilibrium cluster configurations.

Finally, all the above described theory-levels of the diatomic approach are summarized in the mini-review^[26].

By definition, cluster binding energy is the difference between sum of energies of isolated atomic particles and energy of their bounded structure. Energy of a neutral atom exceeds that of positive ion by the ionization potential (IP), while is less by the electron affinity (EA) that of negative ion. Let $Q=0, \pm 1, \dots, \pm n$ be the ionic charge number of the cluster, then,

$$\varepsilon_Q = \frac{QE_Q}{n} \quad (5)$$

should be the specific binding energy correction

related to its charge state if E_Q is IP or EA depending on the sign of Q . Taking into account this correction, in present work, specific binding energy of planar boron clusters are estimated from the relation:

$$\varepsilon \approx \frac{1}{n} \left(\frac{1}{2} \sum_{i=1}^{i=n} (E_0 C_i - E_1 Z_i \sum_{k_i=1}^{k_i=C_i} Z_{k_i}) + E_Q Q \right) \quad (6)$$

3. Species studied and results

Because B_{12} icosahedral clusters are the main structural units of structural modifications of boron and boron-rich compounds, here we studied stability of planar boron clusters B_{11} , B_{12} and B_{13} with almost the same number of constituent atoms both in neutral- and charged-states.

For obtaining numerical results, one needs input parameters such as E_0 and E_1 (or d) characteristic of pair interaction between two boron atoms. They can be found e.g. from the quasi-classical B-B potential^[27]: $E_0 \approx 2.80$ eV, $E_1 \approx 8.09$ eV; and $d \approx 1.78$ Å. Note that this potential was successfully applied to explaining of the above mentioned isotopic effects of boron atoms also in geometric models for boron nanostructures^[28].

As for IP and EA of boron atom, they equal to $E_{+1} \approx 8.30$ eV and $E_{-1} \approx 0.28$ eV, respectively^[29]. Outer valence shell of the isolated B-atom contains a single $2p$ -electron. Consequently, their total number $V=10$ in B_{11}^+ , $V=11$ in B_{11}^0 and B_{12}^+ , $V=12$ in B_{11}^- , B_{12}^0 and B_{13}^+ , $V=13$ in B_{12}^- and B_{13}^0 , and $V=14$ in B_{13}^- , respectively. Obtained results of calculations confirmed the expectation that cluster-isomers with symmetrical shapes and without holes (vacant sites) in their structure, i.e., with the maximal number of interatomic bonds, should be most stable. Correspondingly, in the tables below, we present structures and characteristics only for ground-state isomers.

Table 3-1 shows that among the neutral clusters studied, the atomic charges are maximal in B_{11} , apparently because of its asymmetric structure. On contrary, symmetric clusters B_{12} and B_{13} reveal higher polarity of bonding in their charged-states.

Table 3-1. Static charge number of atomic sites in most abundant boron clusters

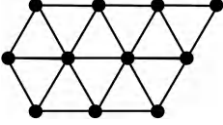
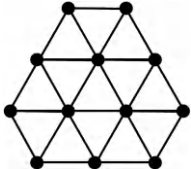
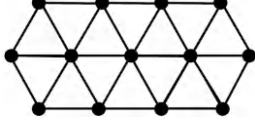
Ground-state isomer	Cluster	Coordination number	Number of sites	Static charge number
	B_{11}^+	2	1	+ 11/21
		3	4	+ 2/7
		4	4	+ 1/21
		6	2	- 3/7
	B_{11}^0	2	1	+ 10/21
		3	4	+ 3/14
		4	4	- 1/21
		6	2	- 4/7
	B_{11}^-	2	1	+ 3/7
		3	4	+ 1/7
		4	4	- 1/7
		6	2	- 5/7
	B_{12}^+	3	6	+ 5/16
		4	3	+ 1/12
		6	3	- 3/8
	B_{12}^0	3	6	+ 1/4
		4	3	0
		6	3	- 1/2
	B_{12}^-	3	6	+ 3/16
		4	3	- 1/12
		6	3	- 5/8
	B_{13}^+	3	6	+ 4/13
		4	4	+ 1/13
		6	3	- 5/13
	B_{13}^0	3	6	+ 1/4
		4	4	0
		6	3	- 1/2
	B_{13}^-	3	6	+ 5/26
		4	4	- 1/13
		6	3	- 8/13

Table 3-2. Specific binding energy of most abundant boron clusters

Clusters	Binding energy per atom, eV
B_{12}^+	6.49
B_{13}^+	6.34
B_{11}^+	6.21
B_{13}^0	5.60
B_{12}^0	5.47
B_{11}^0	5.34
B_{13}^-	5.25
B_{11}^-	5.24
B_{12}^-	5.10

From the **Table 3-2**, one can see that positively charged clusters are certainly more stable than neutral clusters, while lasts are more stable than negatively charged ones.

Table 3-3. Specific binding energy of neutral pairs of most abundant boron clusters

Pairs of clusters	Binding energy per atom, eV
$B_{11}^- + B_{13}^+$	5.83
$B_{12}^+ + B_{12}^-$	5.79
$B_{11}^+ + B_{13}^-$	5.69
$B_{11}^0 + B_{13}^0$	5.48
$B_{12}^0 + B_{12}^0$	5.47

According to the data presented in the **Table 3-3**, preferably channels of ablation of icosahedral boron-rich materials are related to the formation of neutral pairs of differently charged clusters.

4. Discussion and conclusions

Before making conclusions based on results

obtained by us, we need to discuss shortly the theoretical data available in the literature on B_{12} cluster isomers stability.

As is known, boron atoms are unique in their strong preference for forming icosahedral structural units. In the icosahedral cage B_{12} , each atom has 5 other atoms as nearest neighbors. Such B_{12} units are unstable by themselves, but distorted B_{12} icosahedra do form a stable framework for boron and many boron compounds. In particular, the α -rhombohedral crystalline boron may be considered an almost perfect cubic close packing of B_{12} icosahedra. In general, the persistence of the icosahedral structure is explained by the fact that the chemical valence of boron is not completely saturated under 5-fold coordination and that there exist outwardly directed bonds which serve to link icosahedra.

The X_α -method of the scattered-wave self-consistent-field (SCF- X_α -SW) with muffin-tin-potential and local exchange was applied^[30] to determine quantitatively electronic structure and binding energy of icosahedral B_{12} . Then the binding energy was used to estimate the cohesive energy of the B_{12} units in the α -rhombohedral structure. From this, an effective B_{12} - B_{12} interaction potential in the solid was constructed. The binding energy of 35.6 eV was obtained at an equilibrium bond distance of 1.96 Å, which is within 10 % of the bond distance of 1.77 Å found in B_{12} icosahedra in bulk boron. The electronic structure of B_{12} corresponded to an open-shell configuration so that such an isolated cluster would be chemically unstable.

Geometries and electronic structures of the B_{12} cluster have been investigated using a Car-Parrinello ab initio molecular dynamics simulation^[31]. The icosahedral structure was found to be locally stable, but with a few dangling bonds. On annealing or melting, this structure rearranges to a more open geometry. The new structure has a significantly lower energy despite a lower coordination. But, bonds are stronger and there are no dangling bonds.

The structure and stability of small boron clusters were investigated employing density functional theory (DFT)^[32]. The search for minima was performed using gradient methods at the local spin

density (LSD) level. Most of the final structures prefer planar or quasi-planar forms and can be considered to be fragments of planar or spherical surfaces. A group of spherical boron clusters may exist. However, their energies are generally higher than those of the convex or quasi-planar clusters. This also means that clusters of real bulk, sections of the boron lattice, have less stable configurations. They try to close the open spheres with a small number of atoms. In particular, the distorted icosahedral B_{12} cluster with closed structure has energy by 2.01–3.28 eV higher than that of the convex B_{12} structure.

Based on ab initio quantum-chemical methods, accurate calculations on small boron clusters were carried out to determine their electronic and geometric structures^[33]. The geometry optimization with a linear search of local minima on the potential-energy surface (PES) was performed using analytical gradients in the framework of the restricted Hartree-Fock SCF approach. Most of the final structures of the boron clusters are composed of two fundamental units: either of hexagonal or of pentagonal pyramids. The resulting quasi-planar and convex structures can be considered as fragments of planar surfaces and as segments of nanotubes or hollow spheres, respectively. In particular, the most stable isomers of B_{12} clusters are 2 planar and 1 convex clusters. In contrast to the convex or the quasi-planar clusters, the structures of the cage-clusters are rather similar to those of the well-known α - and β -rhombohedral boron crystals, or to those of the boron hydrides. The energies of the cage-clusters on average are between 2 and 5 eV higher than those of the convex or the quasi-planar clusters.

Taking into account that interesting features of elemental boron and boron compounds are the occurrence of highly symmetric icosahedral clusters and rich chemistry of boron also dominated by cage-structures, in the study of Zhai *et al.*^[34], the authors reported experimental and theoretical evidences that small boron clusters prefer planar structures and exhibit aromaticity and antiaromaticity according to the Huckel rules, akin to planar

hydrocarbons.

The electronic and geometric structures, including binding energies, of small and neutral boron clusters have been investigated using DFT^[35]. Linear, planar, convex, quasi-planar, open-cage and cage structures have been found. None of the lowest energy structures and their isomers has an inner atom; i.e., all the atoms are positioned at the surface. Within size range under the consideration, the planar and quasi-planar (convex) structures have the lowest energies. In particular, 11 different structures of B₁₂ cluster were investigated. Their binding energies are ranging from 4.037 to 4.599 eV/atom. The first lowest energy isomer is a convex structure containing three dovetailed hexagonal pyramids. Only ninth and tenth isomers are cages, slightly distorted icosahedral structures without the central atom.

Among the several aromatic boron clusters, B₁₂ and B₁₃⁺ are unique. They show three distinct sets of sextets, resulting in extraordinary kinetic stability. A novel way to analyze them was proposed in the study of Kiran *et al.*^[36], in which the cluster is partitioned as inner and outer rings. The molecular orbital analysis, based on this fragmentation, reveals that the delocalized valence electrons in B₁₂ and B₁₃⁺ clusters can be trifurcated leading to triple aromaticity, which is unique to these clusters.

Recently, Bhattacharyya *et al.*^[37] conducted a comprehensive numerical study of the ground-state structures of isomers of B₁₂ cluster. Geometry optimization was performed at a level of theory employing the extended basis sets. Once the geometry of a given isomer was optimized, its ground state energy was calculated more accurately at the level of theory employing even larger basis set. Thus, computed values of binding energies of various isomers are expected to be quite accurate. Geometry optimization revealed 10 distinct isomers. The vibrational frequency analysis performed on the 3 lowest energy isomers showed them to be stable. While, in boron-rich solids, icosahedron is the basic structural unit, in the isolated form, it was demonstrated to be unstable. The disc-like lowest-energy structure of B₁₂ cluster can be seen as a conse-

quence of the Jahn–Teller distortion of its icosahedral isomer. Computed binding energies per atom are 4.60 and 4.31 eV for quasi-planar and icosahedral isomers with C_{3v} and C_{2h} point group symmetries, respectively. This work, based upon ab initio geometry optimization, verifies early results and predicts the B₁₂ icosahedron to be higher in energy as compared to the lowest energy quasi-planar B₁₂ cluster. This clearly illustrates the tendency of the icosahedral structure towards distortion to a lower symmetry one, consistent with the Jahn–Teller theorem.

Thus, neutral B₁₂ icosahedral clusters constituting boron-rich materials, on ablation have to be converted into (quasi) planar disc-like isomer with higher specific binding energy. The charged cluster B₁₃⁺ also should have higher stability. Consequently, the formation of B₁₁, B₁₂ and B₁₃ clusters in different charged-states is expected.

Our calculations performed within the diatomic model using quasi-classical B–B interatomic potential, lead to following hierarchies in the formation probabilities of single boron clusters in various charged states and their neutral pairs: B₁₂⁺ > B₁₃⁺ > B₁₁⁺ > B₁₃⁰ > B₁₂⁰ > B₁₁⁰ > B₁₃⁻ > B₁₁⁻ > B₁₂⁻ and B₁₁⁻ + B₁₃⁺ > B₁₂⁺ + B₁₂⁻ > B₁₁⁺ + B₁₃⁻ > B₁₁⁰ + B₁₃⁰ > B₁₂⁰ + B₁₂⁰, respectively.

The obtained results would be helpful in controlling the synthesis of nanoboron materials with specific engineering properties.

References

1. Becker R, Chkhartishvili L, Martin P. Boron, the new graphene? *Vacuum Technology & Coating* 2015; 16 (4): 38–44.
2. Becker R, Chkhartishvili L, Martin P. Tribological applications for boron. *Vacuum Technology & Coating* 2015; 16 (10): 36–41.
3. Chkhartishvili L. Micro- and nano-structured boron. In: Perkins GL (editor). *Boron. Compounds, production and application*. New York: Nova Science Publishers; 2011.p. 221–294.
4. Chkhartishvili L. Nanoboron (An overview). *Nano Studies* 2011; 3: 227–314.
5. Chkhartishvili L. All-boron nanostructures. In: Kharisov B I, Kharissova O V, Ortiz–Mendez U (editors). *CRC concise encyclopedia of nanotechnology*. Boca Raton: CRC Press; 2016. p. 53–69.

6. Albert B, Hillebrecht H. Boron: Elementary challenge for experimenters and theoreticians. *Angewandte Chemie International Edition* 2009; 48(46): 8640–8668.
7. Boustani I. Towards novel boron nanostructural materials. In: Springborg M (editor). *Chemical Modelling: Applications and theory*. Cambridge: Royal Society of Chemistry; 2011. p. 1–44.
8. Fermi E. *Molecules, crystals, and quantum statistics*. New York, Amsterdam: W. A. Benjamin INC; 1966.
9. Novikova SI. *Thermal Expansion of Solids*. Moscow: Nauka; 1974.
10. Slutsker AI, Gilyarov VL, Luk'yanenko AS. Energy features of an adiabatically loaded anharmonic oscillator. *Physics of the Solid State* 2006; 48(10): 1947–1953.
11. Chkhartishvili L, Gabunia D, Tsagareishvili O, *et al.* Estimation of isotopic composition effect on substance melting temperature. *Bulletin of the Georgian National Academy of Sciences* 2004; 170(3): 530–532.
12. Chkhartishvili LS, Gabunia DL, Tsagareishvili OA. Estimation of the isotopic effect on the melting parameters of boron. *Inorganic Materials* 2007; 43(6): 594–596.
13. Chkhartishvili LS, Gabunia DL, Tsagareishvili OA. Effect of the isotopic composition on the lattice parameter of boron. *Powder Metallurgy and Metal Ceramics* 2008; 47(9-10): 616–621.
14. Gabunia D, Tsagareishvili O, Chkhartishvili L, *et al.* Isotopic composition dependences of lattice constant and thermal expansion of β -rhombohedral boron. *Journal of Physics: Conference Series* 2009; 176(012022): 1–10.
15. Chkhartishvili L, Tsagareishvili O, Gabunia D. Isotopic expansion of boron. *Journal of Metallurgical Engineering* 2014; 3 (3): 97–103.
16. Chkhartishvili L. On quasi-classical estimations of boron nanotubes ground-state parameters. *Journal of Physics: Conference Series* 2009; 176(1): 1–9.
17. Chkhartishvili L. Molar binding energy of the boron nanosystems. In: Konuk A, Kurama H, Ak H, *et al.* (editors). *Proceedings of the 4th international boron symposium*. Ankara: Osmangazi University; 2009. p.153–160.
18. Chkhartishvili L. Nanotubular boron: Ground-state estimates. In: Chikoidze E, Tchelidze T (editors). *New developments in materials science*. New York: Nova Science Publishers; 2011. p. 67–80.
19. Oganov AR, Chen J, Gatti C, *et al.* Ionic high-pressure form of elemental boron. *Nature* 2009; 457(7251): 863–867.
20. Chkhartishvili L, Becker R. Effective atomic charges and dipole moment of small boron clusters. *Proceedings of the ICANM 2015*. Ottawa: IAEMM; 2015. p. 130–147.
21. Becker R, Chkhartishvili L. Dipole moment of quasi-planar boron clusters. *Nano Studies* 2015; 11: 29–48.
22. Chkhartishvili L, Becker R, Avci R. Relative stability of boron quasi-planar clusters. In: Darsavelidze G, Guldashvili A, Chedia R, *et al.* (editors). *Proceedings of the international conference “Advanced Materials & Technologies”*. Tbilisi: Universal; 2015. p. 42–46.
23. Chkhartishvili L. Small elemental clusters in pair interaction approximation. *Proceedings of the ICANM 2016*. Montreal: IAEMM 2016. p. 128–132.
24. Chkhartishvili L. Planar clusters of identical atoms in equilibrium: 1. Diatomic model approach. *American Journal of Nano Research & Applications* 2017; 5(3-1): 1–4.
25. Chkhartishvili L. Quasi-planar elemental clusters in pair interactions approximation. *Open Physics* 2016; 14(1): 617–620.
26. Chkhartishvili L. Boron quasi-planar clusters. In: Pogrebnyak AD (editor). *A mini-review on diatomic approach*. *Proceedings of the IEEE 7th international conference on nanomaterials: Applications & properties (NAP—2017), Part 4, Track: Nanomaterials for electronics, spintronics and photonics*; Sumy: Sumy State University; 2017. p. 1–5.
27. Chkhartishvili L, Lezhava D, Tsagareishvili O. Quasi-classical determination of electronic energies and vibration frequencies in boron compounds. *Journal of Solid State Chemistry* 2000; 154(1): 148–152.
28. Chkhartishvili L, Mamisashvili N, Maisuradze N. Single-parameter model for multi-walled geometry of nanotubular boron. *Solid State Sciences* 2015; 47: 61–67.
29. Hayes WM (editor-in-chief). *Handbook of Chemistry and Physics (94th Ed.)*. Boca Raton: CRC Press; 2013. p. 10–147 & 10–197.
30. Bambakidis G, Wagner RP. Electronic structure and binding energy of the icosahedral boron cluster B₁₂. *Journal of Physics and Chemistry of Solids* 1981; 42(11): 1023–1025.
31. Kawai R, Weare JH. Instability of the B₁₂ icosahedral cluster: Rearrangement to a lower energy structure. *The Journal of Chemical Physics* 1991; 95(2): 1151–1159.
32. Boustani I. Structure and stability of small boron clusters. A density functional theoretical study. *Chemical Physics Letters* 1995; 240(1-3): 135–140.
33. Boustani I. Systematic ab initio investigation of bare boron clusters: Determination of the geometry and electronic structures of B_n (n = 2–14). *Physical Review B* 1997; 55(24): 16426–16438.
34. Zhai H, Kiran B, Li J, *et al.* Hydrocarbon analogues of boron clusters — planarity, aromaticity and antiaromaticity. *Nature Materials* 2003; 2(12): 827–833.
35. Atis M, Ozdogan C, Guvenc ZB. Structure and energetic of B_n (n = 2–12) clusters: Electronic structure calculations. *International Journal of Quantum*

- Chemistry 2007; 107(3): 729–744.
36. Kiran B, Kumar GG, Nguyen MT, *et al.* Origin of the unusual stability of B_{12} and B_{13}^+ clusters. *Inorganic Chemistry* 2009; 48(21): 9965–9967.
 37. Bhattacharyya P, Boustani I, Shukla A. First principles electronic structure study of B_{12} isomers: Jahn–Teller distortion flattens the icosahedron into a disc. arXiv:1802.01072v1 [physics.atm-clus] 4 Feb 2018; 1–32.

ORIGINAL RESEARCH ARTICLE

Subnanophase coatings as new type low-dimensional nanomaterials: Ultra-high-vacuum synthesis, properties and application

Nikolay Plusnin

Institute of Automation and Control Processes, Far East Branch, Russian Academy of Sciences, Vladivostok, Russia;
E-mail: plusnin@dvo.ru

ABSTRACT

In this paper, a classification of low-dimensional nanomaterials is given, and new type of these nanomaterials — subnanophase coatings are proposed. Experimental results on the formation of a wetting layer of a transition metal on a silicon substrate by physical deposition in vacuum and results of this layer identification by the EELS method are given. Based on these results, a new approach to the formation of subnanophase coatings has been proposed by creation of an interface stresses structuring WL. The possible properties and application prospects of subnanophase coatings are considered.

Keywords: Low-dimensional Nanomaterials; Subnanophase Coatings; Wetting Layer; Ultrahigh-vacuum; Formation; Properties; Application

ARTICLE INFO

Article history:

Received 24 June 2020

Received in revised form 18 July 2020

Accepted 23 July 2020

Available online 3 August 2020

COPYRIGHT

Copyright © 2020 Nikolay Plusnin.

doi: 10.24294/can.v3i2.1069

EnPress Publisher LLC. This work is licensed under the Creative Commons Attribution-NonCommercial 4.0 International License (CC BY-NC 4.0).

<http://creativecommons.org/licenses/by/4.0/>

1. Introduction

In the world there are many major scientific, educational and technological centers that are engaged in researches and various applications of nanotechnology and nanomaterials. In particular, there are a number of manufacturers of nanophase materials. The most famous among them is the company “Nanophase Technologies”, which produces nanodispersed powders “Nanogard” and “Nanotech” based on zinc and aluminum oxides, respectively^[1].

Usually, nanophase materials are obtained by compacting bulk materials from nanodispersed particles with a diameter of 2 to 50 nm. As a result, after compacting, they consist of grains 4-30 nm in size. In their atomic structure, nanophase materials are neither amorphous, nor crystalline, nor even quasicrystalline. It is believed that they are in a low-dimensional-nanophase state. This production technology of nanophase materials is still relevant today.

Considering the main role of effects underlying their basis, low-dimensional nanomaterials can be classified as follows:

- 1) Low-dimensional heterocrystalline ones with the effect of intercrystalline proximity.
- 2) Low-dimensional heterophase amorphous ones with the effect of interphase proximity.
- 3) Low-dimensional ones with the quantum effect in their constituent particles.
- 4) Two-dimensional ones with the effect of interaction with the

substrate.

5) Two-dimensional ones with the effect of interaction with the vacuum.

6) Two-dimensional ones with a transboundary quantum size effect.

Besides, various types of low-dimensional nanomaterials are possible, including thin-film, dispersed and composite nanomaterials, which are combination of these types of nanomaterials.

Here, we will focus on subnanophase coatings (SNP) consisted of low-dimensional clusters with a decisive influence on these coatings of interaction effects with the substrate and vacuum. Due to the influence of the strained interface on their structure and properties, these coatings can have a set of unique properties that are absent in bulk coatings, as well as in massive nanophase materials.

It is assumed that SNP coatings will be used in areas of the nano industry where the use of massive (with a thickness of more than 1 nanometer) and high-stable coatings is not required. Namely, when the coating can be non-equilibrium and metastable and have a nanometer thickness.

The problem of creating SNP coatings is associated with the methods of their synthesis, as well as with the methods of structural-phase diagnosis of their state and diagnosis of their properties, both in the process of obtaining these coatings and at its completion. The combination of the synthesis and growth control of SNP coatings in an ultrahigh vacuum environment allows reducing the number of control cycles and, thus, more effectively finding nanomaterials with the required properties.

Ultra-high vacuum (UHV) is the most convenient and cleanest medium for controlling the atomic and electronic structure and various properties of coatings. UHV allows you to synthesize coatings from atomic or molecular beams^[2] and use electron, ion, and photon beams to diagnose coatings^[3]. In addition, UHV-vacuum provides the ability to control the surface state of the coatings during their synthesis and allows cyclically controlling the formation of ultrathin layers and their interfaces, creating the necessary composition and structure in them. In addition, UHV technology (UHVT) similar

to nanotechnology (NT) is high-tech technology and use controlled manipulations with individual atoms and molecules.

In a vacuum, particle beams and fields can interact on a solid surface without interference. This property gives UHVT a unique advantage over NT in other environments. First of all, it is the controllability of the synthesis of coatings. Another important advantage of UHVT is the pure conditions for the synthesis and control of coatings. As for the lower level of practical application of UHVT due to the high cost, this is offset either by the high cost of the product (for example, in nanomedicine) or by the ability to produce a product in the form of a coating on large substrates (for example, in the field of solar energy, microelectronics and nanoelectronics).

Currently, methods and devices for the synthesis and control of coatings in vacuum have evolved significantly and reached a high level of perfection^[4]. This allows, in the main, focusing not on creating these methods, but on their use. However, the specificity of SNP coatings, their non-equilibrium, subnanostructural state, requires more precise regulation and a wider range of growth parameters. For this, it is necessary to develop methods for producing directed atomic beams, which will have a higher density and simultaneously lower temperature or kinetic energy.

In addition, the structure-phase specificity of SNP coatings, which differs in their atomic density and interatomic bonding configuration from bulk phases, requires the further development of more adequate methods of structural-phase analysis directly during synthesis. Therefore, it is necessary to increase the sensitivity of these methods or adapt them to the subnanometric sample thickness and to work in real time. The solution of these problems will allow creating new types of nanomaterials in a subnanophase state.

The purpose of this work is to develop an approach to the self-organizing synthesis of subnanophase coatings using physical deposition of vapor phase in ultrahigh vacuum.

2. Creating subnanophase coatings in vacuum

For the synthesis of SNP coatings in vacuum, both new methods of obtaining atomic vapor beams with low thermal energy of vapor are needed. Also methods of electron spectroscopy, microscopy and probe measurements adapted to SNP coatings are needed. In addition, it is necessary to solve the following list of main tasks for obtaining SNP coatings:

- (1) To develop design principles for their electronic and atomic structure.
- (2) To develop the principles of management of their growth and self-organization by regulating the density and temperature of the atomic vapor stream, as well as the temperature of the substrate.
- (3) To develop principles of subnanoscale diagnostics in real time of their structural-physical and other properties.

For this, it is necessary to conduct both theoretical studies (including computer simulation) and experimental studies.

Deposition from the vapor phase in vacuum at a low substrate temperature usually provides a non-equilibrium and, in particular, nanophase state of the coating^[5]. However, to obtain a thinner coating in a sub-nanophase state, this is not enough. High kinetic energy of vapor and latent heat of phase transitions in coating lead to mixing at the interface and the formation of alloys or compounds and additionally cause cluster fusion into larger islands and, thus, coarsening of the grains and transition to the bulk phase^[6].

The obvious way to solve this problem is to evaporate the material at a source with a low vapor temperature^[6,7], as well as decreasing the diffusion and chemical interaction of the coating with the substrate using a sub- or single-molecular intermediate layer^[8]. Also, it is necessary to modify the methods for monitoring the structural state of the coating and the interface layer thickness during the growth of coatings^[7,9,10].

The possibility of realizing the self-organization of SNP coatings from the vapor phase or atom-

ic beam was first shown by the example of metal growth on the surface of a single-crystal silicon substrate. Such a coating was first called by a surface multilayer phase^[11,12], and then, a two-dimensional nanophase^[13,14]. The first of these names reflected the view on the stabilizing role of the substrate, and the second on the two-dimensional nature of the SNP coating. Subsequently, the SNP coating got the short name “v-phase”. In this name, the uncertainty and low dimension structure of the SNP coating and, accordingly, the difficulty of its identification from experimental data were reflected.

Indeed, the existing variety of experimental research methods (X-ray, electron, ion, probe microscopy and spectroscopy) is well developed for the study of single-crystal, amorphous and even quasicrystalline homogeneous structural state. But, in the case of low-dimensional, disordered and, in general, non-uniform coating, most of these methods do not allow identifying this coating and separating them from bulk homogeneous phases. As a result, the SNP coating is often interpreted as a mixture of some bulk phases.

Nevertheless, the method of electron spectroscopy of characteristic electron energy loss (EELS) allowed us to identify the integral structure of the v-phase, namely the structure of its electron density and, indirectly, of its atomic density.

Indeed, the energy position of the loss peak in the EELS spectrum connected with the excitation of a volume plasmon gives information about the oscillation frequency of the plasma of valence electrons in the local region in which the electron loses its energy. And the oscillation frequency, in turn, gives information about the density of valence electrons and, indirectly, about the density of atoms that donate their electrons to a valence bond of one or another type.

For a solid, an approximation of solid balls is usually used. In this model, atoms are very tightly packed like solid balls. With this, the densest packing is realized in an ordered lattice — in a crystal. But, in the crystal, one can break the dense structure of the packing by means of subjecting this body to

stretching, inserting vacancies and rotating interatomic bonds, forming clusters and intercluster (intergranular) defective interfaces, as well as rotating the clusters themselves relative to each other.

Something similar seems to be realized in the v -phase under the action of tensile stresses caused by the substrate and under the action of its conjugation with this phase. It leads to the fact that the atoms in the phase at the interface are not closely connected to each other and their packaging is not compact. Due to this, in the EELS spectrum of the v -phase, shifted bulk plasma loss (BPL) peak is formed. But if the v -phase has an inhomogeneous structure, there will form a whole group of peaks. Each peak in this group corresponds to a local collective interaction with electrons of the same type of configuration of interatomic bonds and with the same electron density. The adaptation of the atomic and electron density in the phase to the density of the substrate, as well as the non-uniform nature of this density, cause the BPL peak to shift, expand, and decrease in intensity. Thus, it is possible to distinguish the v -phase from the bulk coating and determine the range of thickness on which the v -phase is formed by use the shift, the degree of expansion of the BPL peak, and a decrease in its intensity.

3. Experimental observation of metal SNP on silicon

A series of experiments was carried out to study the initial stage of growth of transition metals on silicon using the methods of AES, LEED, EELS, AFM, as well as measurements of conductivity, optical reflection and magnetization. Namely EELS data showed the formation of an SNP coating. Based on EELS data, we previously called these coatings by the v -phase, and then we called them by the wetting layer (WL). The latter name reflects the adaptation of the atomic density of the SNP coating to the atomic density of the substrate.

Figure 1 and **2** present the EELS spectra families, showing changes of electron density in Fe and Cr layers and at the metal-substrate interface, during growth of Fe and Cr on Si (001) and Si (111),

respectively. In **Figure 1a** and **1b**, electron density changes are shown in the case of mixing Fe with the Si substrate and in the case of the growth of pure Fe at elevated and lowered temperatures of metal's vapor, respectively. **Figure 1c** shows the EELS spectra of the Fe–Si phases obtained after annealing the samples of **Figure 1b**.

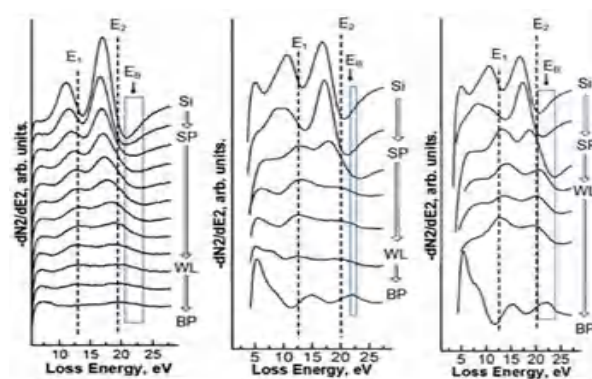


Figure 1. EELS Fe on Si (001) in the case of Fe growth at elevated (a) and lowered (b) vapor temperature, respectively; (c) EELS of Fe–Si phases on Si (001) after moderate annealing of the Fe coating in Figure (b)^[15].

In each case, we see transitions of: 1) a pure silicon surface (Si) into the surface phase (SP); 2) SP into the wetting layer (WL); and 3) WL of maximum thickness into the bulk phase (BP) of the metal or metal-silicon compound (silicide). These transitions show a change in the position of the peaks of the surface (E_1) and bulk (E_2) losses. The transition into SP ends when the surface loss shift ceases. And the transition into WL is completed when the energy position of the peak of bulk losses stabilizes without reaching the position of the peak of bulk losses in BP (EB).

Figure 1a and **1b** also show a non-monotonic increase in the energy of the peak of bulk plasmon losses, corresponding to transitions from SP to WL and from WL to BP. The formation of WL in non-equilibrium conditions is a general phenomenon of the formation of the metal/silicon interface. With this, in the case of solid-phase epitaxy, even ordering WL occurs, as is shown in **Figure 2**. And that evokes compacting WL. Therefore atomic density of WL becomes closer to the density of bulk silicide.

However, as can be seen from **Figure 1b** and **Figure 1c**, the amplitude of the peak of volume plasmon losses at the stage of WL formation is much smaller, and the peak width is greater than in BP. This can be explained only by the formation of SNP coverage. Moreover, in the case of SNP coverage of pure Fe on Si (001) (**Figure 1b**), these differences are more pronounced, since this coating is in a more non-equilibrium state and has a more pronounced gradient of the atomic density.

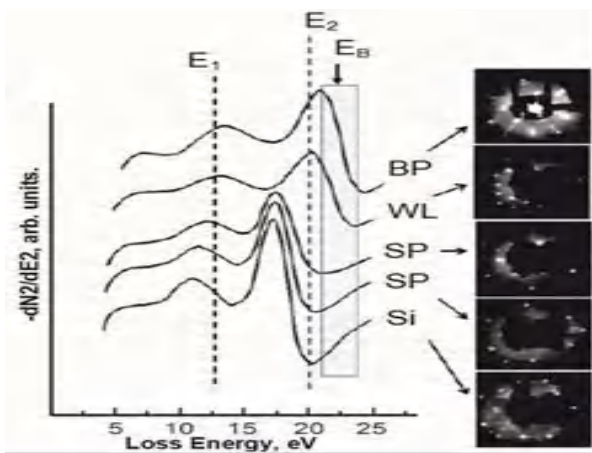


Figure 2. EELS and LEED of Cr-Si phases on Si (111) obtained by the deposition of Cr with an elevated vapor temperature and annealing^[15].

Indirect evidence of the formation of the Fe SNP on Si (001) at the WL formation stage was obtained on the basis of AES and AFM data. At this stage, for samples in **Figure 1c**, the stability of the coating in composition decreased according to AES, and the height of the surface relief was significantly less than at the stage of BP formation^[14].

At the same time, on the AFM images, the WL relief was not seen due to the diameter of the AFM needle near 1 nm. Invisible relief at this thickness can be explained only by a subnanophase structure of the coating. Additional confirmation of such structure of the metal WLs is also provided by data of on their electrical, optical and magnetic properties^[16]. These data show a resistive type of conductivity (independence of resistance on the temperature) of Cr WL, a high UV absorption (low UV reflection) in WL of Fe on Si (001). Moreover, the dependence of polarized light reflection on the

magnitude of the magnetic field perpendicular to Fe WL corresponds to the superparamagnetism of this WL. And as it is known, resistive type of conductivity, high UV absorption and superparamagnetism are most pronounced in coatings and films of metals with a nanophase or finely dispersed structure.

4. Properties and application of SNP coatings

Cluster or subnanoscale structure, uneven along the plane and subnanoscale gradient of structural properties in the transverse direction, determine the specific properties of coatings. Examples of specific properties of SNP coatings can also be increased wetting ability, increased surface area, increased surface curvature and latent energy of stresses. Due to the reduced atomic density, the presence of clusters, near amorphous type structure, a large number of vacancies, they will also have their modified electronic structure and modified optical, magnetic and electrical properties. And, as a result, there will be coatings with high UV absorption, magnetic-soft coatings and coatings with resistive conductivity type^[16]. In addition, in SNP coatings, by analogy with multilayer coatings, a chemical potential gradient is possible and, as a consequence, the presence of an embedded electric field.

Due to the low thickness of SNP coatings and due to the vacuum environment during physical vapor deposition, the scope of applications of SNP coatings will be limited to the element base of electronics, optoelectronics, and telecommunications. In addition, they can be used for various specialized applications where there is no mechanical damage and the influence of the corrosive environment and the atmosphere (for example, in biosensors).

It is assumed that the main application of SNP coatings will focus in the range of nanoelectronics, nanospintronics, nanooptics, nanoplasmonics, and analytical instrumentation for ecology, biology and medicine. Another application of SNP is the use of a tension energy hidden in them for solid-phase reactions, crystallization and other processes of formation of ultra-thin coatings.

5. Conclusion

The subnanophase coatings as a class of new materials have been proposed based on the classification of low-dimensional nanomaterials. Synthesize these coatings using physical deposition from low-temperature vapor with control them in ultrahigh vacuum, and use the EELS method to identify their subnanophase structure have been proposed. The experimental observations of subnanophase coatings in the form of a metal wetting layer on silicon substrate and also the indirect evidences of their subnanophase structure on data of AFM, optical, electrical and magnetic measurements have been presented. The properties and possible applications of subnanophase coatings are considered.

References

1. Hannink RHJ, Hill AJ (editors). Nanostructure control of materials. Cambridge: Woodhead Publishing Limited, 2006. p. 368.
2. Voorhoeve RJH. Molecular beam deposition of solids on surfaces: Ultrathin films. In: Treatise on solid state chemistry. New York, London: Plenum Press; 1976. p. 241–342.
3. O'Connor DJ, Sexton BA. Smart RStC (editors). Surface analysis methods in material science. New York, Berlin: Springer Verlag; 1992. p. 480.
4. Oura K, Lifshits VG, Saranin AA, *et al.* Surface science: An introduction. Berlin: Springer Verlag; 2003. p. 440.
5. Henini M (editor). Molecular beam epitaxy: From research to mass production. London: Elsevier; 2012. p. 744.
6. Plusnin NI, Il'yashchenko VM, Krylov SV. Effect of incident atomic beam power on the formation of a Fe/Si(111)7×7 interface. Technical Physics Letters 2007; 33: 486–489.
7. Plusnin NI. Atomic-scale control of molecular-beam growth of nanolayers. In: Comprehensive guide for nanocoatings technology. Volume 2: Characterization and reliability. New York: Nova Science Publishers Inc; 2015. p. 87–102.
8. Plusnin NI, Tarima NA, Il'yashchenko VM, *et al.* The effect of underlayer-modified atomic monolayer on the mechanism of subsequent film growth. Technical Physics Letters 2012; 38: 324–327.
9. Plusnin NI. Application of AES and EELS for surface/interface characterization. Journal of Electron Spectroscopy & Related Phenomena 2004; 137: 161–164.
10. Plusnin NI. The use of AES and EELS for complex analysis of two-dimensional coatings and their growth process. Modern Electronic Materials 2017; 3: 131–141.
11. Plusnin NI. From physics of the interface formation to low-dimensional nanocoatings and nanomaterials based on them. Vestnik of Far East Branch of Russian Academy of Science 2016; 4(188): 27–35. Available from: <https://cyberleninka.ru/article/n/optfizki-formirovaniya-granitsy-razdela-k-nizkorazmernym-nanopokrytiyam-i-materialam-na-ih-osnove>.
12. Plusnin NI, Galkin NG, Lifshits VG, *et al.* Formation of interfaces and templates in the Si(111)-Cr system. Surface Review and Letters 1995; 2: 439–449.
13. Plusnin NI, Il'yashchenko VM, Kitan' SA, *et al.* Metal thin-film nanophases and their interface with silicon. Journal of Physics Conference 2008; 100: 052094.
14. Plusnin NI, Il'yashchenko VM, Kitan' SA, *et al.* Formation, electronic structure, and stability of film nanophases of transition metals on silicon. Journal of Surface Investigation. X-ray, Synchrotron and Neutron Techniques 2009; 3(5): 734–746.
15. Plusnin NI. Atomic-scale AES-EELS analysis of structure-phase state and growth mechanism of layered nanostructures. Advances in Materials Physics and Chemistry 2016; 6: 195–210.
16. Plusnin NI. Metallic nanofilms on single crystal silicon: Growth, properties and applications. Modern Electronic Materials 2017; 3(2): 57–65.

REVIEW ARTICLE

A review on metal-organic framework: Synthesis, properties and application

Sanju Soni¹, Parmendra Kumar Bajpai², Charu Arora¹

¹Department of Chemistry, Guru Ghasidas Vishwavidyalaya, Bilaspur, C.G. 495009, India

E-mail: charuarora77@gmail.com

²Department of Pure and Applied Physics, Guru Ghasidas Vishwavidyalaya, Bilaspur, C.G. 495009, India

ABSTRACT

Metal organic framework is a class of hybrid network of supramolecular solid materials comprised of a large number of inorganic and organic linkers all bounded to metal ions in a well-organized fashion. This type of compounds possess a greater surface area with an advantage of changing pore sizes, diversified and beautiful structure which withdrew an intense interest in this field. In the present review articles, the structural aspects, classification, methods of synthesis, various factors affecting the synthesis and stability, properties and applications have been discussed. Recent advances in the field and new directions to explore the future scope and applications of MOFs have been incorporated in this article to provide current status of the field.

Keywords: Metal Organic Framework; Nanoporous Material; Drug Delivery; Gas Sensor; Secondary Building Unit

ARTICLE INFO

Article history:

Received 5 August 2020

Received in revised form 4 September 2020

Accepted 7 September 2020

Available online 20 September 2020

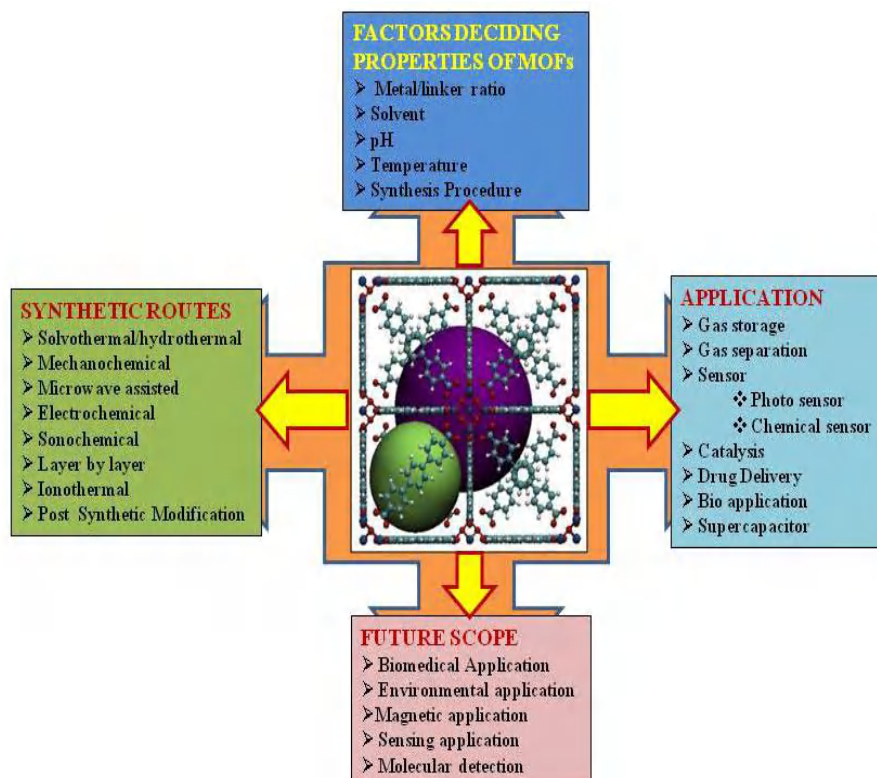
COPYRIGHT

Copyright © 2020 Sanju Soni *et al.*

doi: 10.24294/can.v3i2.551

EnPress Publisher LLC. This work is licensed under the Creative Commons Attribution-NonCommercial 4.0 International License (CC BY-NC 4.0).

<http://creativecommons.org/licenses/by/4.0/>



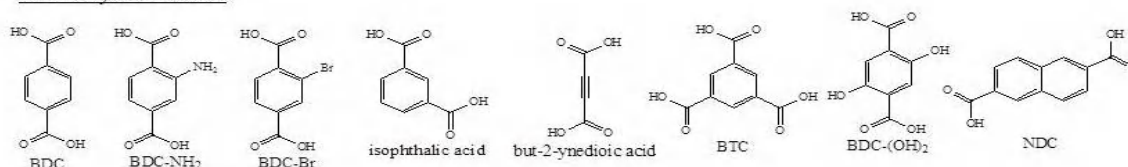
Framework of this paper

1. Introduction

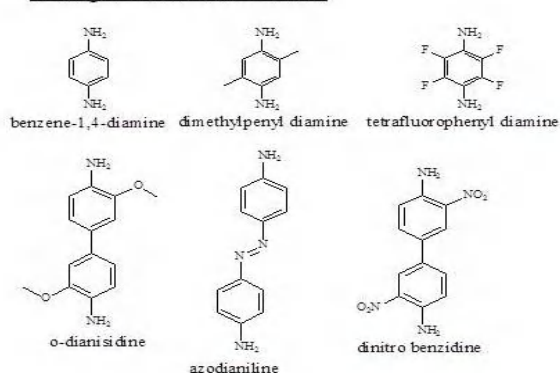
Metal-organic framework (MOF) is a promising class of materials composed of metal centres or clusters and organic linkers. These are porous crystalline materials in which metal is locked into a position to produce rigid and porous geometry and connected through different organic groups. Due to structural flexibility, large surface area and tailorable pore size, MOFs have wide applications in field of gas adsorption and storage, separation, catalysis, sensing, molecular recognition, drug delivery, non-linear optics, luminescence etc.^[1-12]. Due to three dimensional tuneable porous channels, MOFs are useful materials for storage, separation or conversion of molecules on the basis of dimension. Generally, MOFs are related to the general class of co-ordination polymers. However, MOFs are more

specific than co-ordination polymers for 2D or 3D crystallized networks with porous structure. Thus these are also termed as porous coordination polymer (PCP)^[13,14]. Although, several review articles on metal-organic frameworks have been published previously, however, recent advances including the contributions of some Indian research groups, such as Banerjee *et al.*, Ghosh *et al.*, and Kumar etc. necessitates further review on this topic. The present paper comprehensively reviewed the methods of synthesis, properties and applications of MOFs based on reported literature. Recent advances and new foundations, direction for further exploring MOFs for their applications as well as critical analysis of the research have been incorporated in this paper so as to provide the current status of the field.

Carboxylate linkers



Nitrogen donor atom linkers



Neutral nitrogen atom containing heterocyclic linkers

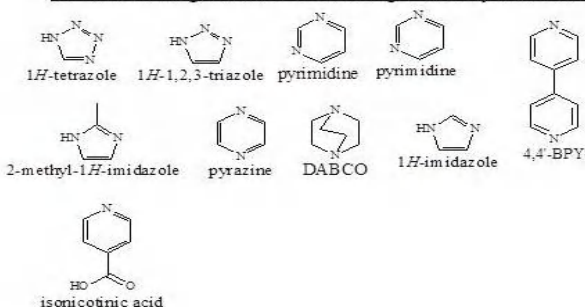


Figure 1. Some Linkers used in synthesis of MOFs.

2. Structural aspects

2.1 Primary building units

The metal ions (connectors) connecting the organic polymers which are linkers are basic primary units that result in porous three dimension structure MOFs. Thus, the metal ions and organic compounds used in the formation of metal-organic frameworks are the “Primary Building Units”.

Commonly, metal ions of first row transition series such as Cr³⁺, Fe³⁺, Co²⁺, Zn²⁺ are used as connectors in the formation of MOFs^[15-17]. Some alkali metal ions^[18,19], alkaline-earth metal ions^[20-22] and rare earth metal ions^[23-27] are also used as a metal connector in the synthesis of MOFs. Nitrate, acetate, sulphate, chloride and oxide of metals are used as precursor for preparing MOFs in most of the synthesis routes. However, in electrochemical synthesis

of MOFs metal rods are used.

Organic linkers, through which the metal ions or nodes are connected, generally contain functional groups that are capable of forming coordination bonds such as carboxylate, phosphate, sulfonate, amine, nitrile etc. some examples of organic linkers are shown in **Figure 1**.

2.2 Secondary building units (SBUs)

In MOFs, organic linkers are connected through metal-oxygen-carbon clusters, instead of metal ions alone. These metal-oxygen-carbon clusters are referred as “Secondary Building Units” (SBUs). SBUs have intrinsic geometric properties, which facilitate MOF’s topology^[28]. Some SBUs are shown in **Figure 2**.

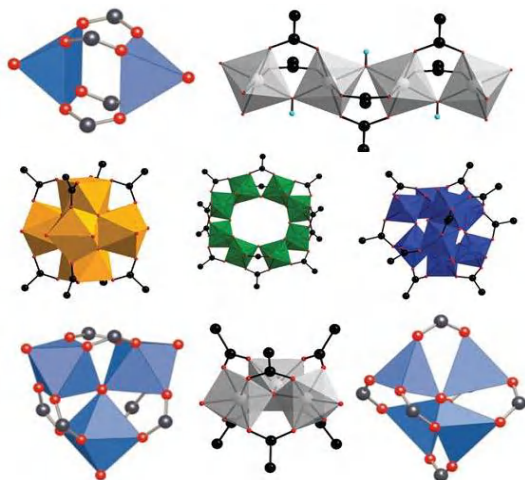


Figure 2. Some secondary building units (SBUs).

2.3 Classification of metal-organic frameworks

On the basis of structural features, MOFs have been classified^[29] in following groups.

(a) Rigid frameworks: These are stable and robust porous frameworks and retain their porous framework on adsorption or desorption of guest molecules. These MOFs are applicable in molecular sieving^[30].

(b) Flexible/dynamic frameworks: Flexible frameworks show an utmost change in shape on insertion or removal of guest particles and also affected by external factors such as pressure, temperature. Dynamic MOFs show a change in framework on

removal of solvent molecules but retain their porous structure on adsorption of gas molecules at high pressure^[4]. MIL-5^[31,32], MIL-8^[33] and SNU-M10^[34] are some MOFs that exhibit breathing effect during adsorption and desorption. In breathing MOFs^[35], there is a severe change in unit cell volume (pore volume) on adsorption/desorption of guest molecules. Different types of flexibility modes are identified and reviewed as shown in **Figure 3**.

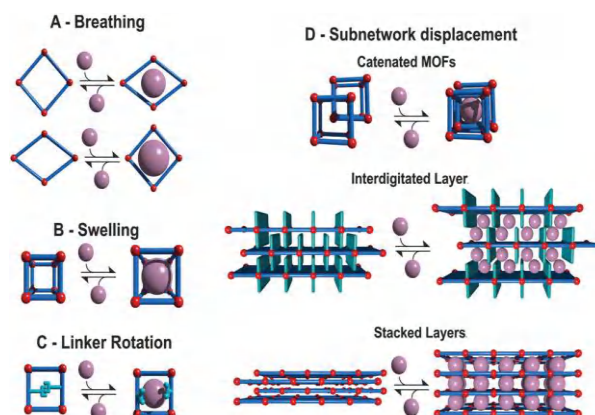


Figure 3. Classification of different flexibility modes of MOFs.

(c) Open metal site: Performance of MOFs can be enhanced by the presence of open metal site. Presence of water in open metal site MOFs enhances the CO₂ capture ability of the MOFs. For example, HKUST-1 [(Cu)₃(btc)₂] which has an open metal site structure and consists of paddlewheel units Cu₂(COO)⁻ connected through btc³⁻ ligands, exhibits a significant increase in CO₂ adsorption when it contains 4 wt.% water^[36].

(d) Surface functionalized framework: Adsorption ability of MOFs can be enhanced by grafting functional groups onto the surface of the MOFs. Functional groups with a high affinity for CO₂ (e.g. arylamine^[37], alkylamine^[38], hydroxyl^[39]) have been reported to enhance the capacity and selectivity of MOFs for CO₂ adsorption when these functional groups are grafted onto the surface of the porous framework through either ligand modification or coordination to unsaturated metal centre.

3. Synthesis of MOFs

As discussed earlier, MOFs consists of two major components, metal ion and organic linkers

or bridging ligands. Conventionally, MOFs are prepared by combining metal ions and organic linkers under mild conditions in order to get a crystalline and porous network. This is termed as “Modular Synthesis”^[40].



During the last two decades, different synthesis methods have been developed and applied to synthesize these materials. In general, these can be classified as conventional solvothermal method and unconventional method.

3.1 Conventional solvothermal/hydrothermal and non-solvothermal method

In conventional solvothermal synthesis, a mixture of metal ions and organic linkers in solvent is heated in glass vials (for lower temperature) or in Teflon lined autoclaves or bomb reactor (for temperature higher than ≈ 400 K)^[41]. If water is used as solvent, this method is termed as hydrothermal method. The synthesis parameters that are controlled for specific structure are pressure, temperature, solvent composition, reagent concentration etc. Temperature of reaction mixture is an important parameter in the synthesis of MOFs. When the temperature of the reaction is higher than the boiling point of solvent, then the reaction is referred as solvothermal reaction and when the temperature is lower than the boiling point of solvent, it is referred as nonisothermal reaction. Some MOFs, such as MOF-5, MOF-74, MOF-177, HKUST-1 ZIF-8, have been reported to synthesize at ambient condition^[42-44]. This method is also known as direct precipitation reaction. Morphology of the crystals produced is highly affected by the reaction temperature^[45].

3.2 Unconventional methods

A mixture of metal salt and organic linker is grinded in a mortar pestle or in a ball mill without using solvent after grinding the mixture is heated gently to evaporate water or other volatile molecules which are formed as by products in the reaction mixture^[46]. This method is termed as mecha-

nochemical method. In this method, breaking of intramolecular bonds by mechanical force takes place followed by a chemical transformation. The method is known to be environmentally friendly because of no use of any solvent and can give high yield of products^[47,48]. Quantitative yields of small MOF particles can be obtained in short reactions times, normally in the range of 10-60 min. In many cases, metal oxides were preferred over metal salts as starting material, which results in water as the only byproduct^[49]. Synthesis of porous framework using mechanochemical method is first reported by Pichon *et al.*^[50] in 2006. Comparative study of a bipyridene-based covalent organic framework (COF) has been reported using solvothermal and mechanochemical methods and it is revealed that proton conducting property^[51] is revealed by mechanochemically synthesized COF only. When solvent is added in a small amount, the mechanochemical process is termed as liquid-assisted grinding (LAG). Addition of small amount of solvents in reaction mixture accelerates the mechanochemical reactions by increasing the mobility of the reactants^[52].

3.3 Alternative synthesis methods

Alternative routes have also been attempted in addition to these methods. Alternative routes can lead to different crystallization rate, particle size, size distribution and adsorption properties as well as morphologies that can have an influence on the properties of material. For example, diffusion of guest molecules in porous materials with different particle size can exhibit a direct effect on catalytic activity, adsorption and separation capacity of molecules. Important alternate routes can be categorised as:

3.3.1 Microwave-assisted synthesis

In this method, energy for reaction is provided in the form of microwave (MW) radiation. It is generally used in organic syntheses, but it has wide application in rapid synthesis of nanoporous materials. Apart from fast crystallization, phase selectivity^[53,54], narrow particle size distribution^[55] and morphological controls^[56,57] are some of the advantages of this method. Several MOFs containing

Fe^{3+} , Al^{3+} , Cr^{3+} , V^{3+} , Ce^{3+} have been synthesised using MW assisted method. Cr-MIL-100^[58] is the first MOF which has been synthesized via MW method.

Formation of MOFs has been reported to carry out under MW radiation at a temperature over 100°C with reaction time exceeding 1 hour. Generally, MOFs can be formed quickly via MW irradiation with respect to conventional electrical heating process. By applying MW synthesis route two MOFs, named IRMOF-1 and HKUST-1, are studied widely. IRMOF-1 reveals crystals of higher quality and better CO_2 adsorption when it is synthesized via MW assisted route^[59]. Highly pure and micropore with high volume ($0.79 \text{ cm}^2 \text{ gm}^{-1}$) HKUST-1 is prepared by MW synthesis in a short time of 30 minutes^[60].

3.3.2 Electrochemical synthesis

Researchers at BASF first reported the synthesis of MOF using electrochemical route^[61]. They developed new synthesis procedures for some MOFs using Zn, Cu, Mg, Co as cathode material and 1,3,5- H_3BTC and 1,2,3- H_3BTC , H_2BDC and $\text{H}_2\text{BDC}-(\text{OH})_2$ as linkers. Electrochemical synthesis of MOF uses metal ions continuously supplied through anodic dissolution as a metal source instead of metals salts, which react with the dissolved linker molecules and a conducting salt in the reaction medium. Protic solvents are used to avoid deposition of metal on cathode, but H_2 is generated in this process^[62]. The electrochemical route is also possible to run normal batch reactions^[49]. MOFs containing ionic liquids as linker e.g. $[\text{Zn}(\text{MIm})_2]$ and $[\text{Zn}(\text{BIm})_2]$ are also synthesized via electrochemical route^[63].

Schlesinger *et al.*^[60] synthesized HKUST-1 using solvothermal, ambient pressure and electrochemical routes and compared the effect of synthesis procedures on its properties. It has been pointed out that the product obtained via electrochemical route reveals inferior quality due to incorporation of linker molecules and/or conducting salt in the pores during crystallization.

3.3.3 Sonochemical synthesis

This is a rapid and environmental-friendly method in which ultra-sonic radiation (20 kHz-10 MHz) is used for MOFs synthesis. This method, via homogenous and accelerated nucleation, can also achieve a reduction in crystallization time and significantly smaller particles size than those by the conventional solvothermal synthesis^[64,65]. When high energy ultrasound interacts with liquid, cavitation (process of bubble formation, growth and collapse under altering pressure) takes place and provides energy with high temperature of $\approx 5000\text{K}$ and pressure of $\approx 1000 \text{ bar}$ ^[66].

In case of solids, microjets are formed as a result of cavitation process and these microjets clean, erode or activate the surface. Dispersion of agglomerated smaller particles takes place. A chemical reaction can take place when ultrasonic radiation is applied to homogenous liquid. Qiu *et al.*^[67] were the first who reported a MOF $[\text{Zn}_3(\text{BTC})_2]$ synthesized sonochemically in ethanol which reveals selective sensing towards organoamine. Effect of reaction time on particle size is also investigated in sonochemical synthesis of MOFs. Partial decomposition of crystals at long reaction time is obtained in the sonochemical synthesis of HKUST-1^[68].

3.3.4 Layer by layer synthesis

Layer by layer method is used for the preparation of MOF thin films. The method is based on surface chemistry in which functionalized organic surface is immersed sequentially into the solutions of metal ion and organic linker. It was observed that orientation of thin film depends on that sequence through which the reactants are added^[69]. The kinetics for stepwise formation in this method has been studied using Surface Plasmon Resonance (SPR) spectroscopy. Metal source and surface termination are the two major factors that affect the rate of growth MOF film^[70,71]. Highly oriented growth was observed for substrates functionalized with different functional groups such as COOH , OH ^[72].

Besides these synthesis routes, other routes such as chemical solution deposition^[73-75] (for the preparation of thin film MOFs), post synthesis modi-

fication^[49] (when functional groups cannot be incorporated during MOF synthesis), and ionothermal method^[76, 77] (ionic liquids are used as solvent) have also been implemented for MOF synthesis. Banerjee and coworkers have reported Fe-based MOF which is prepared by Fe-metallogels via gel degradation^[78]. However, other MOF has not been reported by this method so far.

4. Factors affecting the synthesis of MOFs

4.1 Solvents

Solvent system plays an important role in MOF synthesis as well as in deciding the morphology of MOFs. Solvents may coordinate with metal ion and or may act as space filling molecules^[79,80]. Instead, they also act as a structure directing agent^[49]. Solvents used in MOF synthesis should have high boiling point and polar nature. Usually, dimethyl formamide (DMF), diethyl formamide (DEF), dimethyl sulphoxide (DMSO), dimethyl acetamide (DMA), alcohols, acetone, acetonitrile etc. are used as solvent as is shown in **Figure 4**. Sometimes a mixture of solvents is also used, which depends on the solubility of starting materials.

MOF synthesis process is affected by the reaction medium because of polarity of solvent used and solubility and protolysis property of organic linker. It is also reported that different solvent systems in same reaction condition provide MOF of different

morphology. This may happen because of difference in degree of deprotonation of organic linker in different solvent system. Banerjee *et al.*^[81] reported MOFs containing magnesium and PDC (3, 5-pyridine dicarboxylic acid) have different crystal structure prepared under same condition using different solvent system (**Figure 5**). They found that coordination ability of solvent with metal determines the dimensionality of MOF network. Among DMF, H₂O, EtOH and MeOH, H₂O has the highest affinity towards Mg while EtOH and MeOH do not having any affinity to coordinate with metal centres when DMF/MeOH and EtOH/H₂O are used as solvent.

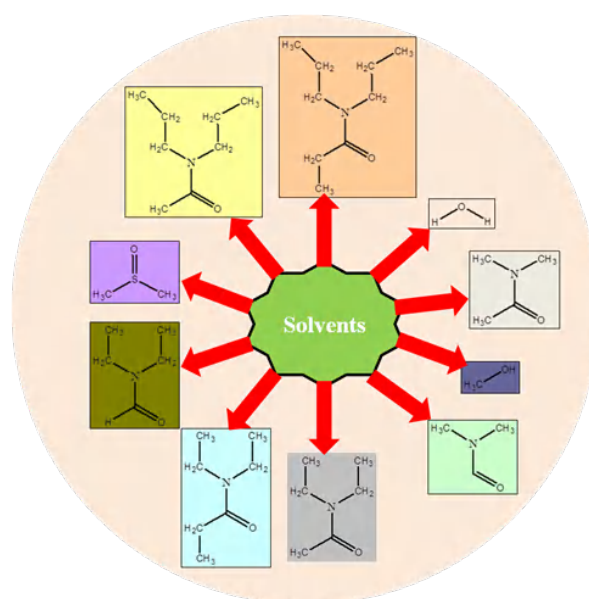


Figure 4. Solvents used in Synthesis of MOFs.

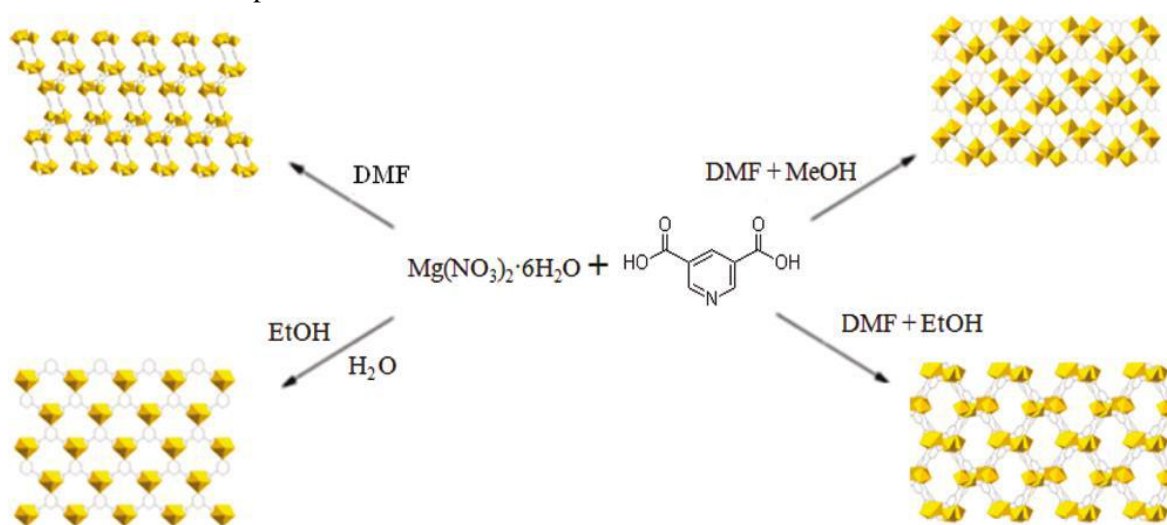


Figure 5. Effect of solvent systems on morphology of MOF.

In addition to structure, different solvent systems result in synthesis of MOFs having difference in pore size. MOFs of cobalt and 4,4'-((5-carboxy-1,3-phenylene bis(oxy)) dibenzoic acid (H₃CPBDA) were synthesized using three different solvents viz. DMP, DMA and DMF under the similar conditions resulting into pore sizes of 76.84 Å, 74.37 Å and 72.76 Å respectively. The change in pore size due to different solvents has been correlated with the size of the solvent molecule. Among the three solvents used the size of the molecules varies as DMP > DMA > DMF. The pore size also reduces in the same order^[82]. Similar correlations are reported by other researchers^[83].

4.2 Effect of temperature and pH on synthesis of MOFs

Temperature and pH of reaction medium have remarkable influence on synthesis of MOFs. Different coordination modes can be adopted by linkers at different pH ranges^[84]. Further, the degree of deprotonation of linker increases on increasing the

pH value. For example, Al³⁺ ion is coordinated with four, six and eight carboxyl O-atoms with increasing pH resulting into MIL-121 (pH = 1.4), MIL-118 (pH = 2) and MIL-120 (pH = 12.2) respectively^[85]. Interpenetrated network has been reported to be formed at higher pH value and uninterpenetrated at lower pH^[86]. Colour of MOF compounds also depend on pH of reaction medium. Luo *et al.*^[87], through their experimental work, explored three Co-MOF complexes, viz. [Co₂(L)(HB-TC)₂(μ₂-H₂O)(H₂O)₂].3H₂O (1), [Co₃(L)₂(BTC)₂].4H₂O (2), [Co₂(L)(BTC)(μ₂-OH)(H₂O)₂].2H₂O (3), (L = 3,3', 5,5'-tetra(1H-imidazol-1-yl)1,1'-biphenyl and BTC = 1,3,5-benzenetricarboxylate) exhibit different structure and colour, by altering the pH value. Along with structure and colour, these three MOFs exhibited different adsorption capability. It is also revealed that compounds of higher dimension are formed at higher pH^[88]. The effect of pH on various properties of MOFs is summarized in **Table 1** as reported in the study of Chu *et al.*^[88]

Table 1. Effect of pH on MOFs

S. No.	Properties of Co-MOFs	Complex-1	Complex-2	Complex-3
1	Chemical Formula	[Co ₂ (L)(HBTC) ₂ (μ ₂ -H ₂ O)(H ₂ O) ₂].3H ₂ O	[Co ₃ (L) ₂ (BTC) ₂].4H ₂ O	[Co ₂ (L)(BTC)(μ ₂ -OH)(H ₂ O) ₂].2H ₂ O
2	Morphology	Monoclinic	Monoclinic	Orthorhombic
3	Space group	P2/c	C2/c	Pccn
4	pH	5	7	9
5	Colour	Pink	Purple	Brown

Temperature of the reaction is another important factor which affects the properties of synthesized MOFs. High temperature favours higher crystallization due to high solubility of reactants and results in formation of large crystals of high quality^[89-91]. Nucleation and crystal growth rates were affected by temperature of reaction mixture. Morphology of synthesized MOFs can also be altered by varying the temperature of reaction medium. MOFs of Tm-succinate^[92], are synthesized at different temperatures with same empirical formula but different morphology i.e. monoclinic and triclinic. Bernini *et al.* prepared two Ho-succinate MOFs and reported that the MOFs prepared via hydrothermal method at higher temperature is ther-

mally more stable as compared to the other prepared at room temperature^[93]. Along with thermal stability, hydrothermal methods also provide denser, less hydrated and higher dimensional solids^[94].

5. Factors affecting the stability of MOFs

5.1 Surface engineering

Crystal growth of MOFs can be altered via “coordination modulation”^[95] which involves introduction of monodentate ligands known as “modulators” with same functional group as to the existing multidentate organic ligand. Modulators can increase or decrease the crystal growth by control-

ling the nucleation leading to the formation of MOFs crystals of different size. When modulators decrease the crystal growth they can be used as “capping agents”. Sodium acetate^[96-99], sodium formate^[99-101], acetic acid^[102-104], benzoic acid^[103], n-dodecanoic acid^[105], trifluoroacetic acid (TFA)^[106], pyridine^[104], n-butyl amine^[101], 1-methyl imidazole^[101], polymers such as PVP^[107], PEG^[108], chitosan^[108] have been used as modulators/capping agents in synthesis of MOF. It is also reported that the concentration of modulator can influence the crystal size and morphology of MOF crystals. In

microwave synthesis^[109] of HKUST-1, when lauric acid is used as modulator, the crystal sizes change from nano to micro scale range. However, when capping agent is used in large amount formation of a new phase is induced^[99]. Stability and specific properties of MOF crystals such as molecule sensing^[107,110], drug delivery^[108] etc. can be enhanced by using modulators. MOF^[111] coated with liposomes lipid has been explored for imaging and anticancer property. Effect of some modulators or capping agents on the properties of MOFs has been summarized in the **Table 2**.

Table 2. Effect of capping agents/modulators on MOF properties

S. No.	Modulator/capng agent	MOF	Change in MOF's property	Ref
1	Sodium formate	HKUST-1	Reduction in crystal size, phase change	100
2	Sodium Acetate	MIL-68(In)	Decrease in length and diameter of hexagonal nanorods	97
3	n-dodecanoic acid	HKUST-1	Change in morphology	105
4	Acetic acid	NH ₂ -MIL-53 (Al)	Selective capping of crystal faces	102
5	Benzoic acid, acetic acid	UiO-66, UiO-66(NH ₂), UiO-67, UiO-68	Improve crystallinity, formation of single crystal	103
6	TFA	UiO-66	Induce defects	106
7	Sodium Acetate	[Ln(1,3,5-btc)(H ₂ O)] _n (Ln = Dy ³⁺ , Tb ³⁺)	2D nano sheet	98
8	PVP/silica	[Mn(1,4-bdc)(H ₂ O)] _n	Selective uptake in human cancer cell, Enhance imaging	110
9	PEG	MIL-88, MIL-100	Improve aggregation, neutral zeta potential	108

MOFs are also modified via exchanging a terminal ligand by a bridging ligand of different functionality (**Figure 6**). Research group of Kitagawa successfully exchanged the surface ligands of Zn-based MOFs [Zn₂(1,4-ndc)₂(dabco)]_n and [Zn₂(1,4-bdc)₂(dabco)]_n with a fluorescent dye boron dipyrromethene (BODIPY). In these MOFs, only surface carboxylate ligands were exchanged and surface dabco ligands remained unmodified. Furth-

er, due to bulkier nature of BODIPY in comparison to original carboxylate ligand, it gets attached to surface only^[112]. Liu *et al.*^[113] demonstrated the effect of surface modification on properties of ZIF-8. It shows greater stability towards hydrolysis when its surface ligand 2-methylimidazole has been exchanged with more hydrophobic ligand 5, 6-dimethylbenzimidazol (DMBIM).

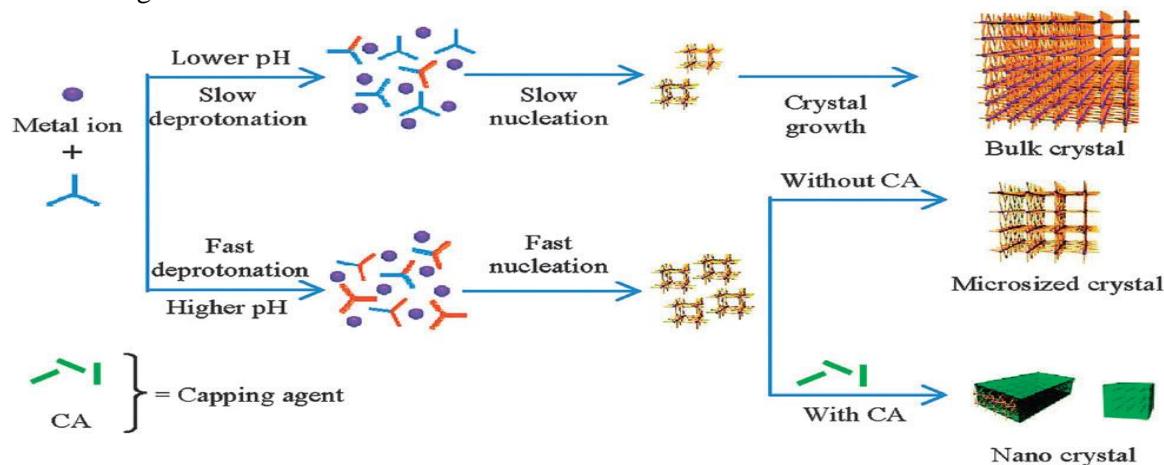


Figure 6. Effect of pH control and crystal capping during coordination modulation.

Unlike linker ligand exchange, it has been difficult to control metal cation exchange in MOFs, as it can lead to the formation of Core-shell structure^[114]. Kitagawa and group reported the core shell hybrid of Cu-MOF $[\text{Cu}_2(1,4\text{-ndc})_2(\text{dabco})]_n$ synthesized on Zn analogous $[\text{Zn}_2(1,4\text{-ndc})_2(\text{dabco})]_n$ by adding Zn crystals to the solution of $\text{CuSO}_4 \cdot 5\text{H}_2\text{O}$, 1,4-ndc and dabco. Formation of green crystals confirms the formation of Cu-MOF on Zn framework surface^[115].

6. Major applications of MOFs

In MOFs, there is a simultaneous appearance of three characteristics, viz. crystallinity, porosity and existence of strong metal-ligand interaction. The unique combination of these properties makes MOFs a very special class of materials^[116]. MOFs show application in catalysis, drug delivery, gas storage, nanoparticle precursor, luminescence, electrochemistry and as sensor in technology.

6.1 Gas storage and separation

There are several methods for storing gas effectively but these require high pressure tank and multistage compressor. These methods are highly expensive for practical uses and there is a need of simpler and cheaper solution. To overcome these issues and to find safer storage methods, several materials, like Zeolite or activated porous carbons, have been studied for gas storage. In this context, MOFs have provided edge over other materials. This is due to easy preparative methods, high surface area, wide opportunities for functionalization and tuneable pore structure which makes MOFs preferable compared to other porous materials.

More than 300 MOFs have been tested for H_2 storage. One of the promising MOFs for this purpose is MOF-177 which consists of $[\text{Zn}_4\text{O}]$ clusters and 4,4',4''-benzene-1,3,5-triyltribenzoate (BTB) to form (6,3) net^[117]. Due to its high surface area ($\sim 5000 \text{ m}^2\text{g}^{-1}$) and large pore volume, it shows a gravimetric H_2 uptake of 7.5 wt.% at 70 bar and 77 K. MOF-5 (IRMOF-1), which is constructed from $[\text{Zn}(\text{OAc})_2]$ and terephthalic acid, possesses a BET

surface area of $3800 \text{ m}^2\text{g}^{-1}$ and takes up 7.1 wt.% at 40 bar and 77 K. Apart from these two, MOF-210, MIL-101, HKUST-1, NU-100, PCN-12, NOTT-102 and MOF-205 are also known for H_2 storage^[118-121]. Generally MOFs with open metal sites provide high surface area facilitating stronger interaction between the metal ion and H_2 molecule. This is the principal reason behind the high H_2 uptake in MOFs. NU-100^[120] has the highest excess H_2 storage capacity i.e., 99.5 mgg^{-1} at 56 bar and 77 K. MOF-210^[121] has been reported as highest total H_2 storage capacity of value 176 mgg^{-1} at 80 bar and 77 K. In addition experimentally, it is reported that doping MOFs with metal ions could enhance the H_2 uptake capacity^[46,122]. As compared to other H_2 storage systems such as transition metal hydrides, MOFs require little energy to release adsorbed hydrogen. This released hydrogen can be used in automobile and fuel cell industries^[123].

MOFs are reported to be useful for reducing CO_2 level in atmosphere. For example, MOF-210 is the highest surface area ($10450 \text{ m}^2 \text{ g}^{-1}$) MOF known to date, synthesized from 4,4',4''-[benzene-1,3,5-triyl-tris(ethyne-2,1-diyl)] tribenzoate (H_3BTE), biphenyl-4,4'-dicarboxylate (H_2BPDC), and zinc (II) nitrate hexahydrate^[121] and has an uptake of CO_2 2400 mg g^{-1} (74.2 wt.%, 50 bar at 298 K) which exceeds that of any other porous material. MOF-200 has a similar CO_2 uptake as MOF-210 under similar experimental conditions^[121]. Other well-known MOFs, such as NU-100 (69.8 wt.%, 40 bar at 298 K), Mg-MOF-74 (68.9 wt.%, 36 bar at 278 K), MOF-5 (58 wt.%, 10 bar at 273 K), and HKUST-1 (19.8 wt.%, 1 bar at 298 K) also show considerable CO_2 uptake. It has also been proved experimentally and theoretically that the presence of polar groups such as $-\text{NH}_2$ or free N containing organic heterocyclic residues on the pores is helpful for high CO_2 uptake compared with unfunctionalized analogues. One of the best examples, Bio-MOF-11, exhibited the effects of an N-heterocycle and its CO_2 uptake of 15.2 wt.% (at 1 bar and 298 K) exceeds any other MOF in the same category^[124].

Noro *et al.* studied the first methane sorption

study on MOFs^[125]. Zhou and co-workers showed methane uptake of 16 wt.% (35 bar) in PCN-14 [Cu₂(adip), Adip = 5,5'-(9,10-anthracenediyl)di-isophthalate] MOF, having BET surface area 1753 m² g⁻¹[126]. Other MOFs such as HKUST-1 (15.7 wt.% at 150 bar), MIL-101 (14.2 wt.% at 125 bar), IRMOF-1 [228 cm³ (STP) g⁻¹ at 298 K and ~36 bar], and MOF-210 (264 mg g⁻¹)^[121] also show considerably high methane uptake capacity. In the case of Ni-MOF-74 [190 cm³ (STP) g⁻¹ (298 K, 35 bar)], open metal sites are the dominating factor responsible for the high methane capacity^[15]. Other important hydrocarbons like benzene, toluene, xylene and linear hydrocarbons have also been effectively separated from liquid mixtures by trapping inside MOFs.

Hazardous gases like CO and NO can also be separated from gas mixtures by using MOFs. Though separation of CO in MOFs could not be achieved experimentally, it is believed that interaction between CO dipole and open metal sites in MOFs are the dominating factor for the sorption performance. On the other hand, MOFs have been used for capturing NO gas, e. g. Cu-SIP-3^[127] and Zn (TCNQ-TCNQ)(bpy) [TCNQ = 7,7,8,8-tetracyano-p-quinodimethane, bpy = 4,4'-bipyridyl]^[128]. Usually these two MOFs are nonporous in nature and they do not absorb gases like Ar, N₂, CO₂ etc., however, these are reported for uptake of NO gas (~9 molecules per formula unit at 1 bar) above gate-opening pressure. Reducing the pressure, the desorption path is not like adsorption. In 2010, Allen and co-workers reported the reason for this performance of the above two MOFs. The strong coordination to coordinatively unsaturated metal sites (CUMs) in case of Cu-SIP-3, while for [Zn (TCNQ-TCNQ)(bpy)], charge transfer plays a crucial role for high NO capture^[127]. Ni- and Co-MOF-74 also exhibited very high NO uptake (~7.0 mmol NO per g of activated material) at room temperature^[129].

In 2014, Yan *et al.* synthesized and characterized a new organic linker 1,2,4,5-tetrakis(3-carboxyphenyl)-benzene (m-H₄TCPB) and its first metal-organic framework Cu-m-TCPB. This compound

can uptake 24.4 cm³g⁻¹ H₂ and 2.3 cm³g⁻¹ N₂ at 77K and 1 atm. It has been reported to possess uptake capacity 23.3 cm³g⁻¹ acetylene, 23.0 cm³g⁻¹ CO₂ and 7.3 cm³g⁻¹ at 273 K and 1 atm^[130].

Instead of gaseous molecule uptake, some MOFs have also been prepared which are capable of adsorption of water molecule. In this direction, R. Banerjee and his research group demonstrated the water adsorption ability of chemically stable keto-enamine COFs^[131].

6.2 Magnetism and its application

Metal organic framework materials show magnetism when paramagnetic 3d transition metal nodes are used along with suitable diamagnetic organic linkers and MOFs with magnetic properties are named as magnetic metal organic frameworks (MMOFs). The MOFs consist of first-row transition metals (V, Cr, Mn, Fe, Co, Ni and Cu) have contributed significantly to develop porous molecular magnets^[132-137]. Close-shell ligands^[138] such as oxo, cyano, azido bridges and polycarboxylic ligands, which give weak magnetic interaction, are good candidates for this purpose.

Another reason for magnetic behaviour of MOFs is the framework structure, which may involve layered geometry with a shorter conjugated distance between metal clusters. Organic linkers have also been used for synthesis of MMOFs, where radicals present in organic linker are responsible for magnetic properties. This metal-radical combined approach has also been used for synthesizing a variety of MMOFs^[139-141].

A Ni-Glutarate based MOF [Ni₂₀(H₂O)₈(C₅H₆O₄)₂₀.40H₂O]^[142] showed ferromagnetic behaviour with a curie temperature of 4K due to weak ferromagnetic interactions of Ni-O-Ni angle. HKUST-1 is antiferromagnetic at high temperature and below 65K shows weak ferromagnetism^[143]. MIL-9^[144] [Co₅(OH)₂(C₄H₄O₄)₄] is reported to possess ferromagnetic properties. Jain *et al.*^[145] reported four MOFs of general formula [(CH₃)₂NH₂] M(HCOO)₃ (M = Mn, Fe, Co, Ni) as multiferroics.

Instead of 3d transition metals, lanthanides also produce magnetic metal-organic frameworks. Two magnetic lanthanide-organic frameworks^[146]

(LnOF), having formula $[\text{Dy}_2(\text{bpa})_2(\text{H}_2\text{O})_3]$ and $[\text{Er}_4(\text{bpa})_4(\text{H}_2\text{O})_6](\text{H}_2\text{O})$, consist a 3D frameworks built by the 1D rod shaped metal carboxylate SBUs and 3,5-bis (4-carboxyphenoxy) benzoate (bpa^{3-}) ligands.

Magnetic MOFs can also be explored for the environmental application in removal of arsenic. Magnetic nanoclusters have been reported for applications in arsenic removal^[147,148].

6.3 Sensing

A large number of MOFs have been reported to be photoluminescent because aromatic units of linkers in most of the MOFs lead to excitation by absorbing UV-visible light and provide luminescence. MOFs as luminescent materials or phosphors can find application in cathode ray tubes, projection television, fluorescent tubes and X-ray detectors^[149], small-molecule sensors^[150,151], pH sensors^[152], light concentrators for photovoltaic devices, antennae in photo-sensitive bioinorganic compounds and high-technology optics. Trivalent lanthanide metal ions are widely used for synthesis of luminescent MOFs due to their electronic transition from d- to f-shell, with accompanying photon emission. Lanthanides like Eu, Tb, Dy, Sm, Nd, Gd, Er and Yb are used as luminescent metal ions. Naphthalene, anthracene, pyrene, perylene and stilbene types of ligands are most commonly used for synthesis of luminescent MOFs. Both the metal and the linker can be used to give rise to luminescence, and can furthermore interact (via antenna effect) to increase the brightness and the quantum yield. 4,4-[(2,5-Dimethoxy-1,4-phenylene)-di-2,1-ethenediyl] bisbenzoic acid (H_2pvdc) was used to efficiently sensitise the NIR emission of the Yb^{3+} ions at ca. 1000 nm in an extended $[\text{Yb}_2(\text{pvdc})_3(\text{H}_2\text{O})_2] \cdot 6\text{DMF} \cdot 8.5\text{H}_2\text{O}$ porous network^[153]. The LnMOFs co-doped with multiple Ln^{3+} ions can be used as bimodal (or multicoloured) light emitters. Bimodal (or multicoloured) emission may be applied in multiplexed detection and imaging of therapeutic cells^[154]. Ln-MOFs are used in cation sensing, anion sensing as well as molecule sensing. A visible colour change of material is one

of the simplest, most powerful sensing strategies. For example, a nanotubular MOF, $\{[(\text{WS}_4\text{Cu}_4)\text{I}_2(\text{dptz})_3] \cdot \text{DMF}\}_n$ ($\text{dptz} = 3,6\text{-di-(pyrid-in-4-yl)-1,2,4,5-tetrazine}$, $\text{DMF} = \text{N,N-dimethylformamide}$) was reported for sensing small solvent molecules. When accommodating different solvent molecules as guests, the resulting inclusion compounds exhibited different colours depending on the solvent guests, showing a new way of signal transduction as a new kind of sensor^[150]. Recently, water stable cationic MOF^[155] has been reported which can adsorb oxoanionic pollutants such as MnO_4^- , $\text{Cr}_2\text{O}_7^{2-}$. Recently, MOFs have been demonstrated as chemical sensor for selective fluorescence quenching of an explosive TNP (2,4,6-tri nitro phenol) in water using urotropin-based metal-organic framework (Ur-MOF)^[156].

Nano MOFs (NMOFs) have experienced another exciting development and NMOFs are used for sensing pesticides. Akash Deep *et al.*^[157] were the first who demonstrated biosensing application of Nano MOF $[\text{Cd}(\text{atc})(\text{H}_2\text{O})_2]_n$ ($\text{atc} = 2\text{-amino terephthalic acid}$) impedimetrically for the detection of organo-phosphate pesticide by developing an anti-paration/NMOF/2-ABA/ITO (ABA = 2-amino benzyl amine, ITO = Indium Tin oxide) sensing platform.

A novel approach to develop an inkless and erasable printing medium using MOFs has been demonstrated by synthesizing photochromic MOF containing 1,4,5,8-naphthalenediimide (NDI) and Ca, Mg, Sr and revealed their inkless printing property^[158]. The print content was self-erased after 24 hours. This may be useful for reducing paper wastage.

6.4 Catalysis

The presence of strong metal–ligand interaction in MOFs can provide permanent porosity to the material, i.e., it is possible to remove solvent molecules completely without structure collapse. MOFs have shown great potential as heterogeneous catalyst. The MOFs, in which metal centres are not completely blocked by organic ligands or unsaturated, i.e., labile ligands are introduced, and are

good catalysts because when labile ligands are generally solvent molecules and when they are removed leave a free coordination position on the metal. For example, $[\text{Cu}_3(\text{btc})_2]$ (btc = 1,3,5-benzenetricarboxylate) material HKUST-1, in which coordinated water molecule leaves a coordination vacancy on Cu upon thermal activation^[159]. A number of organic reactions have been catalyzed by using nanoporous MOFs. For example, Knoevenagel condensation reaction catalyzed by using either $[\text{Cd}(4\text{-btapa})_2(\text{NO}_3)_2]$ (btapa = 1,3,5-benzene tricarboxylic acid tris[N-(4-pyridyl)amide])^[160] or $[\text{Cr}_3\text{F}(\text{H}_2\text{O})_2\text{O}(\text{bdc})_3]$ (bdc = 1,4-benzenedicarboxylate)^[161]. Xu *et al.* synthesized a novel bimetal complex $[\text{Zn}_4\text{Ru}_2(\text{bpd})_4.4\text{C}_2\text{NH}_8.9\text{DMF}]_n$ (H2bpd = 4,4'-biphenyldicarboxylic acid), which can adsorb Ru(II) photosensitizer $[\text{Ru}(\text{bpy})_3]^{2+}$ and cobalamin derivative such as heptamethyl cobyrinate perchlorate (B_{12}) to form a complex $\text{B}_{12}\text{-Ru@MOF}$. This complex has been reported to catalyze dechlorination reaction and 1, 2-migration reaction in solid state. This is the first example of B_{12} catalysis using MOF system^[162].

6.5 Biomedical application

MOFs offer extremely high drug loading capacity and very long release time. As compared to mesoporous silica materials, MOFs can load four times greater drug, i.e., ibuprofen adsorption (upto 1.4 gm per gram of MOFs) with longer release time (upto 21 days)^[108]. Non-toxic MOFs are applicable in targeted drug delivery. MIL family of metal-organic frameworks has a good candidature for storage and controlled release of biologically important molecules due to their enhanced stability, enormous porosity and large pore volume^[10,163]. Serrey and Férey *et al.*^[8] demonstrated encapsulating drug molecules (Ibuprofen) in chromium carboxylate MOFs, MIL-100 and MIL-101, exhibiting drug storage capacities of 35 wt.% and 140 wt.% respectively and controlled drug release behaviour of 5 to 6 days under physiological conditions. Iron (III) carboxylate MOFs such as MIL-88A, MIL-8, MIL-100 and MIL-101 are able to entrap anticancer^[163], anti-tumor and antiretroviral drugs as well as cosmetic agents^[8]. Férey *et al.*^[164] reported first group of

synthesized MOFs using trivalent metal centers with carboxylic acid bridging for drug delivery application. A novel type of magnetic MOF composite $\text{Fe}_3\text{O}_4/\text{Cu}_3(\text{BTC})_2$, fabricated by incorporation of Fe_3O_4 nanorods with nanocrystals of $\text{Cu}_3(\text{BTC})_2$ (HKUST-1), adsorbed upto 0.2 gm of Nimesulide (an anticancer drug for pancreatic cancer treatment) per gram of composite and it took as long as 11 days for the complete drug release in physiological saline at 37°C ^[165]. Zhuang *et al.* demonstrated ZIF-8 as pH responsive drug delivery system with high cellular uptake efficiency by incorporating camptothecin into ZIF-8 nanospheres. This encapsulated ZIF-8 exhibited enhanced cell death^[11].

Bernini *et al.* demonstrated the ability of GCMC (Grand canonical monte carlo) simulation to predict the microscopic performance of new porous MOFs in drug delivery application and validated their simulation, with the available experimental data reported for the adsorption-release of ibuprofen in MIL-53(Fe), MIL-100(Fe) and MIL-101(Cr)^[166]. Their simulation predicted an outstanding ibuprofen adsorption capacity of 1969 mg g⁻¹ for mesoporous BioMOF-100 which is six times higher than the values reported for mesoporous silica. The presence of strong electrostatic interactions due to existence of charge compensating ions in MOFs enhances the adsorbate-adsorbent interaction which leads to higher drug loading at low pressure. In BioMOF-100, dimethylammonium cations present in the pores reinforce the attractive interaction with ibuprofen molecules. Monte carlo simulation was also used for comparing the drug uptake capacity of two different mesoporous MOFs, viz. MIL-101 and UMCM-1 computationally^[9].

Anti-bacterial activity of novel MOF STAM-1^[138] has been compared with that of the HKUST-1 against the growth of some bacteria such as *Clostridium difficile*, *Staphylococcus aureus* and *Pseudomonas aeruginosa*. It is found that both the MOFs have significant effect against the growth of these pathogens. Antimicrobial activity of these MOFs has been enhanced when they are impregnated with NO.

6.6 Electrical property and its application

MOFs have been demonstrated as useful device material for energy storage. Electrical storage capacity of MOFs in Co-doped MOF-5, i.e., Co8-MOF-5^[167] as electrode for supercapacitors has been reported by Diaz *et al.* However, this MOF has much lower capacitance than the commercially activated carbon. Lee *et al.* introduced Cobalt based MOF film^[168] which has pseudocapacitor behavior with specific capacitance upto 206.76 F g⁻¹ and energy density of 7.18 Wh kg⁻¹ at 0.6 A g⁻¹. Zn-doped Ni-based MOF^[169] with a flowerlike microsphere exhibited high specific capacitance (1620 F g⁻¹ and 860 F g⁻¹ at 0.25 and 10 A g⁻¹ respectively), good rate capability and good cycling stability (91% for the MOF with Zn/Ni of 0.26). In 2014, a series of 23 different nanocrystalline MOFs (nMOFs) were reported for their electrochemical energy storage capacity. Among these nMOFs, a zirconium based MOF, i.e. nMOF-867 exhibited high capacitance. nMOF-867 has the stack and areal capacitance of 0.64 and 5.09 mF cm⁻² which is about six times higher than that of the supercapacitors made from activated carbon^[170]. Recently, a Mn-based MOF is employed as the active coating material to enhance the capacity of Li-rich layered Li (Li_{0.17}Ni_{0.20}Co_{0.05}-Mn_{0.58})O₂ oxide as cathode for Li-ion batteries. This surface modified oxide material showed a large discharge capacity, good thermal stability without harming the cycle stability, high initial coulombic efficiency and high rate capability^[171]. Researches in this direction are needed to further explore the applications of MOFs.

7. Future scope

The knowledge about metal organic frameworks is growing rapidly during recent few years but there are still significant gaps in the completeness of our understanding of their structure, stability and properties. Detailed investigations on factors responsible for destruction of crystal structure of certain MOFs with time stability and decomposition mechanism have still not been carried out systematically.

There are some reports on applications of MOFs in drug loading and delivery for some anti-cancer and antiviral molecules. MOFs can be explored for such application for other drug molecules too. Detailed toxicological investigation should be carried out commercialization of such products.

8. Conclusion

In this review article, we have discussed various synthetic methods of MOFs along with their applications. Different methods lead to the MOFs having different properties. MOFs introduced a huge number of applications including gas storage and separation, catalysis, magnetism, sensors, electrical energy storage systems etc. Several applications of MOFs have not been explored yet, for instance, magnetic MOFs can be explored for removal of arsenic from environmental sample same as magnetic nano clusters have been demonstrated. Research work should be carried out to study degradation mechanism of unstable MOF. Studies can also be carried out to evaluate the toxicity of degradation products. These studies will be helpful to explore the biomedical application of nontoxic MOFs. Nontoxic MOFs can be explored for application as solid support for natural bioactive molecules to increase their shelf life and effectiveness.

MOFs should be evaluated for antibacterial and antifungal activities to explore their clinical and biological applications as solid support, UV-screens and synergist.

Abbreviations used

1. Adip — 5,5'-(9,10-anthracenediyl)di-isophthalate
2. BDC — benzene dicarboxylate
3. BODIPY — boron dipyrromethene
4. BTC — benzene tricarboxylate
5. COF — covalent organic framework
6. DABCO — diazabicyclooctane
7. HKUST — Hong Kong University of Science and Technology
8. IRMOF — isoreticular metal organic framework
9. MIL — Materials of Institute Lavoisier
10. MOF — metal organic framework

11. MW — microwave
12. NDC — naphthalene dicarboxylate
13. NU — North Western University
14. PCN — porous coordination network
15. PCP — porous coordination polymer
16. SBU — secondary building unit
17. SIP — 5-sulfoisophthalic acid
18. SNU — Seoul National University
19. STAM — St. Andrews Material
20. TCPB — tetra kis (carboxyphenyl) benzene
21. TFA — trifluoro acetic acid
22. ZIF — zeolitic imidazolate framework

References

1. Eddaoudi M, Moler DB, Li H, *et al.* Modular chemistry: Secondary building units as basis for the design of highly porous and robust metal-organic carboxylate framework. *Accounts of Chemical Research* 2001; 34: 319–330.
2. Rowsell JLC, Yaghi OM. Metal-organic frameworks: A new class of porous materials. *Microporous and Mesoporous Material* 2004; 73: 3–14.
3. Yamada T, Kitagawa H. Protection and deprotection approach for the introduction of functional groups into metal organic frameworks. *Journal of the American Chemical Society* 2009; 131(18): 6312–6313.
4. Horike S, Shimomura S, Kitagawa S. Soft porous crystals. *Nature Chemistry* 2009; 1(9): 695–704. doi: 10.1038/nchem.444.
5. Ferey G. Hybrid porous solids: past, present, future. *Chemical Society Reviews* 2008; 37: 191–214.
6. Lee J, Farha OK, Roberts J, *et al.* Metal-organic framework material as catalyst. *Chemical Society Reviews* 2009; 38: 1450–1459.
7. Horcajada P, Serre C, Maurin G, *et al.* Flexible porous metal-organic frameworks for a controlled drug delivery. *Journal of the American Chemical Society* 2008; 130: 6774–6780.
8. Horcajada P, Serre C, Vallet-regi M, *et al.* Metal-organic frameworks as efficient materials for drug delivery. *Angew Chem Int Ed Engl* 2006; 45: 5974–5978.
9. Babarao R, Jiang J. Unraveling the energetics and dynamics of Ibuprofen in mesoporous metal-organic frameworks. *Journal of Physical Chemistry C* 2009; 113: 18287–18291.
10. Horcajada P, Gref R, Baati T, *et al.* Metal-organic frameworks in biomedicine. *Chemical Reviews* 2012; 112: 1232–1268.
11. Zhuang J, Kuo C, Chou L, *et al.* Optimized metal-organic frameworks nanospheres for drug delivery: Evaluation of small-molecule encapsulation. *ACS Nano* 2014; 8(3): 2812–2819.
12. Kerbellec N, Catala L, Daiquebonne C, *et al.* Luminescent coordination nanoparticles. *New Journal of Chemistry* 2008; 32: 584–587.
13. Kitagawa S, Matsuda R. Chemistry of coordination space of porous coordination polymers. *Coordination Chemistry Reviews* 2007; 251: 2490–2509.
14. Kitagawa S, Kitaura R, Noro SI. Functional porous coordination polymers. *Angew Chem Int Ed Engl* 2004; 43: 2334–2375.
15. Wu H, Zhou W, Yildirim T. High-capacity methane storage in metal-organic frameworks $M_2(\text{dhtp})$: The important role of open metal site. *Journal of the American Chemical Society* 2009; 131: 4995–5000.
16. Zacher D, Shekhah O, Woll W, *et al.* Thin films of metal-organic frameworks. *Chemical Society Reviews* 2009; 38: 1418–1429.
17. Ma M. Preparation, characterization of metal-organic frameworks for biological applications [PhD thesis]. Bochum: Ruhr University; 2011. p.11.
18. Maark TA, Pal S. A model study of effect of $M=\text{Li, Na, Be, Mg}$ and Al ion decoration on hydrogen adsorption of metal-organic framework-5. *International Journal of Hydrogen Energy* 2010; 35: 12846–2857.
19. Lv Y, Zhan C, Feng Y. A chiral manganese-potassium heterometallic MOF with an unusual (3, 7)-connected network. *CrystEngComm* 2010; 12: 3052–3056.
20. Yang L, Vajeeston P, Ravindran P, *et al.* Revisiting isorecticular MOFs of alkaline earth metals: A comprehensive study on phase stability, electronic structure, chemical bonding and optical properties of A-IRMOF-1 ($A = \text{Be, Mg, Ca, Sr, Ba}$). *Physical Chemistry Chemical Physics* 2011; 13: 10191–10203.
21. Platero-Prats AE, Iglesias M, Snejko N, *et al.* From coordinatively weak ability of constituents to very stable alkaline earth sulphonate metal-organic framework. *Crystal Growth & Design* 2011; 11(5): 1750–1758.
22. Platero Prats AE, De la Peña-O’Shea VA, Iglesias M, *et al.* Heterogeneous catalysis with alkaline-earth metal-based MOFs: A green calcium catalyst. *Chemcatchem* 2010; 2: 147–149.
23. Serre C, Ferey G. Hydrothermal synthesis, thermal behaviour and structural determination from powder data of a porous three dimensional europium trimetate: $\text{Eu}_3(\text{H}_2\text{O})(\text{OH})_6[\text{C}_6\text{H}_3(\text{CO}_2)_3] \cdot 3\text{H}_2\text{O}$ or MIL-63. *Journal of Materials Chemistry* 2002; 12: 3053–3057.
24. Serre C, Millange F, Marrot J, *et al.* Hydrothermal synthesis, structure determination, and thermal behavior of new three-dimensional europium terephthalates: MIL-51(LT,HT) and MIL-52 or $\text{Eu}_2^n(\text{OH})_x(\text{H}_2\text{O})_y(\text{O}_2\text{C}-\text{C}_6\text{H}_4-\text{CO}_2)_z$ ($n = \text{III, III, II}$; $x = 4, 0, 0$; $y = 2, 0, 0$; $z = 1, 1, 2$). *Chemistry of Materials* 2002; 14(5): 1965–1975.
25. Reineke TM, Eddaoudi M, O’Keeffe M, *et al.* A microporous lanthanide-organic framework. *Angew Chem Int Ed* 1999; 38: 2590–2594.
26. Serpaggi F, Ferey G. Hybride open frameworks (MIL-n) part 4: Synthesis, and crystal structure of

- MIL-8 a series of lanthanide glutarates with an open framework, $[\text{Ln}(\text{H}_2\text{O})_2]_2[\text{O}_2\text{C}(\text{CH}_2)_3\text{CO}_2]_3 \cdot 4\text{H}_2\text{O}$. *Journal of Materials Chemistry* 1998; 8: 2737–2741.
27. Serpaggi F, Ferey G. Hybrid open frameworks (MIL-n): synthesis and crystal structure of MIL-17 a rare-earth dicarboxylate with a relatively open framework $[\text{Pr}(\text{H}_2\text{O})_2]_2[\text{O}_2\text{C}(\text{CH}_2)_2\text{CO}_2]_3 \cdot \text{H}_2\text{O}$. *Microporous & Mesoporous Materials* 1999; 32: 311–318.
 28. Yaghi OM, O'keeffe M, Ockwing NW, *et al.* Reticular synthesis and design of new materials. *Nature* 2003; 423: 705–714.
 29. Sabouni R. Carbon dioxide adsorption by metal organic frameworks (Synthesis, testing and modeling) [PhD thesis]. Ontario: University of Western Ontario, Electronic thesis and dissertation repository; 2013. p. 28–29.
 30. Dincă M, Long JR. Strong H_2 binding and selective gas adsorption within the microporous coordination solid $\text{Mg}_3(\text{O}_2\text{C}-\text{C}_{10}\text{H}_6-\text{CO}_2)_3$. *Journal of the American Chemical Society* 2005; 127: 9376–9377.
 31. Hamon L, Llewellyn PL, Devic T, *et al.* Co-adsorption and separation of CO_2 - CH_4 mixtures in the highly flexible MIL-53(Cr) MOF. *Journal of the American Chemical Society* 2009; 131: 17490–17499.
 32. Llewellyn P, Bourrelly S, Serre C, *et al.* How hydration drastically improves adsorption selectivity for CO_2 over CH_4 in the flexible chromium terephthalate MIL-53. *Angew Chem Int Ed* 2006; 45: 7751–7754.
 33. Serre C, Mellot C, Surblé S, *et al.* Role of solvent-host interactions that lead to very large swelling of hybrid frameworks. *Science* 2007; 315: 1828–1831.
 34. Choi H, Suh M. Highly selective CO_2 capture in flexible 3d coordination polymer networks. *Angew Chem Int Ed* 2009; 48: 6865–6869.
 35. Schneemann A, Bon V, Schwedler T, *et al.* Flexible metal-organic frameworks. *Chemical Society Reviews* 2014; 43: 6062–6096.
 36. Liang Z, Marshall M, Chaffee AL. CO_2 adsorption-based separation by metal organic framework (Cu-BTC) versus zeolite (13X). *Energy and Fuels* 2009; 23: 2785–2789.
 37. Millward A, Yaghi OM. Metal-organic frameworks with exceptionally high capacity for storage of carbon dioxide at room temperature. *Journal of the American Chemical Society* 2005; 127: 17998–17999.
 38. Demessence A, D'Alessandro D, Foo M, *et al.* Strong CO_2 binding in a water stable, triazolate-bridged metal-organic framework functionalized with ethylenediamine. *Journal of the American Chemical Society* 2009; 131: 8784–8786.
 39. Serre C, Bourrelly S, Vimont A, *et al.* An explanation for the very large breathing effect of a metal-organic framework during CO_2 adsorption. *Advanced Materials* 2007; 19: 2246–2251.
 40. Sumida K, Rogow DL, Mason JA, *et al.* Carbon dioxide capture in metal-organic frameworks. *Chemical Reviews* 2012; 112: 724–781.
 41. Wang C, Ying J. Sol-gel synthesis and hydrothermal processing of anatase and rutile titania nanocrystals. *Chemistry of Materials* 1999; 11: 3113–3120. doi: 10.1021/cm990180f.
 42. Huang L, Wang H, Chen J, *et al.* Synthesis, morphology control and properties of porous metal-organic coordination polymers. *Microporous & Mesoporous Materials* 2003; 58: 105–114.
 43. Tranchemontagne DJ, Hunt JR, Yaghi OM. Room temperature synthesis of metal-organic frameworks: MOF-5, MOF-74, MOF-177, MOF-199 and IRMOF-0. *Tetrahedron* 2008; 64: 8553–8557.
 44. Cravillion J, Munzer S, Lohmeier SJ, *et al.* Rapid room temperature synthesis and characterization of nanocrystals of a prototypical zeolitic imidazolate framework. *Chemistry of Materials* 2009; 21(8): 1410–1412.
 45. Biemmi E, Christan S, Stock N, *et al.* High through screening of synthesis parameters in the formation of metal-organic frameworks MOF-5 and HKUST-1. *Microporous & Mesoporous Materials* 2009; 117: 111–117.
 46. Nouar F, Eckert J, Eubank JF, *et al.* Zeolite like metal-organic framework (ZMOFs) as hydrogen storage platform: Lithium and magnesium ion exchange and H_2 -(rho-ZMOF) interaction studies. *Journal of the American Chemical Society* 2009; 131(8): 2864–2870.
 47. Braga D, Giaffreda SL, Grepioni F, *et al.* Solvent effect in a “solvent free” reaction. *CrystEngComm* 2007; 9: 879–881.
 48. Pichon A, James SL. An array based study of reactivity under solvent free mechanochemical conditions—Insights and trends. *CrystEngComm* 2008; 10: 1839–1847.
 49. Stock N, Biswas S. Synthesis of metal-organic frameworks (MOFs): Routes to various MOFs topologies, morphologies and composites. *Chemical Reviews* 2012; 112: 933–969. doi: 10.1021/cr200304e.
 50. Pichon A, Lazuen-Garay A, James SL. Solvent free synthesis of a microporous metal-organic framework. *CrystEngComm* 2006; 8: 211–214.
 51. Shinde DB, Aiyappa HB, Bhadra M, *et al.* A mechanochemically synthesized covalent organic framework as a proton-conducting solid electrolyte. *Journal of Materials Chemistry A* 2016; 4: 2682–2690. doi: 10.1039/c5ta10521h.
 52. Friscic T, Fabian L. Mechanochemical conversion of a metal oxide into coordination polymers and porous frameworks using liquid assisted grinding. *CrystEngComm* 2009; 11: 743–745.
 53. Jung S, Chang J, Hwang J *et al.* Selective formation of SAPO-5 and SAPO-34 molecular sieves with microwave irradiation and hydrothermal heat-

- ing. *Microporous & Mesoporous Materials* 2003; 64: 33–39. doi: 10.1016/S1387-1811(03)00501-8.
54. Jhung S, Lee JH, Yoon J W, *et al.* Selective crystallization of CoAPO-34 and VAPO-5 molecular sieves under microwave irradiation in an alkaline or neutral condition. *Microporous & Mesoporous Materials* 2005; 80: 147–152. doi: 10.1016/j.micromeso.2004.11.013.
 55. Kang K, Park CH, Ahn WS. Microwave preparation of titanium-substituted mesoporous molecular sieve. *Catalysis Letters* 1999; 59(1): 45–49.
 56. Jhung S, Chang J, Hwang Y, *et al.* Crystal morphology control of AFI type molecular sieves with microwave irradiation. *Journal of Materials Chemistry* 2004; 14: 280–285.
 57. Hwang Y, Chang J, Park SE, *et al.* Microwave fabrication of MFI zeolite crystals with a fibrous morphology and their applications. *Angew Chem Int Ed* 2005; 44: 556–560.
 58. Jhung S, Lee JH, Chang J. Microwave synthesis of nanoporous hybrid material, Chromium trimesate. *Bulletin of the Korean Chemical Society* 2005; 26(6): 880–881.
 59. Lu C, Liu J, Xiao K, *et al.* Microwave enhanced synthesis of MOF-5 and its CO₂ capture ability at moderate temperatures across multiple capture and release cycles. *Chemical Engineering Journal* 2010; 156: 465–470.
 60. Schlesinger M, Schulze S, Hiestchold M, *et al.* Evolution of synthetic methods for microporous metal-organic frameworks exemplified by the competitive formation of [Cu₂(btc)₃(H₂O)₃] and [Cu₂(btc)(OH)(H₂O)]. *Microporous & Mesoporous Materials* 2010; 132: 121–127.
 61. Mueller U, Puetter H, Hesse M, *et al.* (inventors). BASF Aktiengesellschaft, Ludwigshafen, D E (assignee). Method for electrochemical production of a crystalline porous metal organic skeleton material. US patent. WO2005/049892. 2005 Jun 2.
 62. Mueller U, Schubert M, Teich F, *et al.* Metal-organic frameworks — Prospective industrial applications. *Journal of Materials Chemistry* 2006; 16: 626–636.
 63. Richer I, Schubert M, Müller U (inventors). Basf S E, Ludwigshafen DE (assignee). Porous metal organic framework based on pyrroles and pyridinones. US patent. WO2007/131955. 2007 May 17.
 64. Suslick KS, Choe SB, Cichowlas AA, *et al.* Sonochemical synthesis of amorphous iron. *Nature* 1991; 353: 414–416.
 65. Gedanken A. Sonochemical synthesis of amorphous iron. *Ultrason Sonochem* 2004; 11: 47–55.
 66. Sono T, Mingos DMP, Baghurst DR, *et al.* Novel energy source for reactions. In: *The new chemistry*. In: Hall N (editor). Cambridge: Syndicate of the University of Cambridge; 2004.
 67. Qiu L, Li Z, Yun W, *et al.* Facile synthesis of nanocrystals of a microporous metal-organic framework by an ultrasonic method and selective sensing of organoamines. *Chemical Communications* 2008; (31): 3642–3644.
 68. Li Z, Qiu L, Su T, *et al.* Ultrasonic synthesis of the microporous metal-organic framework Cu₃(BTC)₂ at ambient temperature and pressure: An efficient and environmentally friendly method. *Materials Letters* 2009; 63: 78–80.
 69. Zacher D, Yusenko K, A B éard, *et al.* Liquid-phase epitaxy of multicomponent layer-based porous coordination polymer thin films of [M(L)(P)0.5] type: Importance of deposition sequence on the oriented growth. *Chemistry* 2011; 17(5): 1448–1455.
 70. Bai M, Zhang J, Cao L, *et al.* Zinc(II) and cadmium(II) metal complexes with bis(tetrazole) ligands: synthesis and crystal structure. *Journal of the Chinese Chemical Society* 2011; 58: 69–74.
 71. Shekhah O. Layer by layer method for the synthesis and growth of surface mounted metal-organic frameworks (SURMOFs). *Materials* 2010; 3: 1302–1315.
 72. Shekhah O, Wang H, Zacher D, *et al.* Growth mechanism of metal-organic framework: insights into the nucleation by employing a step by step route. *Angew Chem Int Ed* 2009; 48: 5038–5041.
 73. Horcajada P, Serre C, Grosso D, *et al.* Colloidal route for preparing optical thin films of nanoporous metal-organic frameworks. *Advanced Materials* 2009; 21: 1931–1935.
 74. Demessence A, Horcajada P, Serre C, *et al.* Elaboration and properties of hierarchically structured optical thin films of MIL-101(Cr). *Chemical Communications* 2009; 101(46): 7149–7151.
 75. Demessence A, Boissière C, Grosso D, *et al.* Adsorption properties in high optical quality nanoZIF-8 thin films with tunable thickness. *Journal of Materials Chemistry* 2010; 20: 7676–7681.
 76. Cooper ER, Andrews CD, Wheatley PS, *et al.* Ionic liquids as eutectic mixtures as solvent and template in synthesis of zeolite analogues. *Nature* 2004; 430: 1012–1016.
 77. Parnham ER, Morris RE. Ionothermal synthesis of zeolites, metal-organic frameworks and inorganic-organic hybrids. *Accounts of Chemical Research* 2007; 40(10):1005–1013.
 78. Aiyappa HB, Saha S, Garai B, *et al.* A distinctive PdCl₂-mediated transformation of Fe-based metal-organic frameworks into metal-organic frameworks. *Crystal Growth & Design* 2014; 14(7): 3434–3437.
 79. Yakovenko AA, Wei Z, Wriedt M, *et al.* Study of guest molecules in metal-organic frameworks by powder X-ray diffraction: analysis of difference envelope density. *Crystal Growth & Design* 2014; 14(11): 5397–5407.
 80. Akhbari K, Morsali A. Effect of the guest solvent molecules on preparation of different morphologies of ZnO nanomaterials from the [Zn₂(1,4-bdc)₂ (dabco)] metal-organic framework. *Journal of Coordination Chemistry* 2011; 64(20): 352–3530.
 81. Banerjee D, Finkelstein J, Smirnov A, *et al.* Synthesis and structural characterization of magnesium based coordination networks in different solvents.

- Crystal Growth & Design 2011; 11: 2572–2579.
82. Huang W, Yang G, Chen J, *et al.* Solvent influence on sizes of channels in three new Co(II) complexes, exhibiting an active replaceable coordinated site. *Crystal Growth & Design* 2013; 13(1): 66–73.
 83. He Y, Guo J, Zhang H, *et al.* Tuning the void volume in a series of isomorphous porous metal-organic frameworks by varying the solvent size and length of organic ligands. *CrystEngComm* 2014; 16(24): 5450–5457.
 84. Seetharaj R, Vandana P, Arya P, *et al.* Dependence of solvents, pH, molar ratio and temperature in tuning metal organic frameworks. *Arabian Journal of Chemistry* 2016; 12(3): 295–315. doi: 10.1016/j.arabjc.2016.01.003.
 85. Volkringer C, Loiseau T, Guillou N, *et al.* High throughput aided synthesis of the porous metal-organic framework-type aluminium pyromillite MIL-121 with extra carboxylic acid functionalization. *Inorganic Chemistry* 2010; 49(21): 9852–62.
 86. Yuan F, Xie J, Hu H, *et al.* Effect of pH/metal ion on the structure of metal-organic frameworks based on novel bifunctionalized ligand 4'-carboxy-4,2':6',4''-terpyridine. *CrystEngComm* 2013; 15(7): 1460–1467.
 87. Luo L, Lv G, Wang P, *et al.* pH-Dependent cobalt(ii) frameworks with mixed 3,3',5,5'-tetra(1H-imidazol-1-yl)-1,1'-biphenyl and 1,3,5-benzenetricarboxylate ligands: synthesis, structure and sorption property. *CrystEngComm* 2013; 15(45): 9537–9543.
 88. Chu Q, Liu G, Okamura T, *et al.* Structure modulation of metal-organic frameworks via reaction pH: Self-assembly of a new carboxylate containing ligand N-(3-carboxyphenyl) iminodiacetic acid with cadmium (II) and cobalt (II) salts. *Polyhedron* 2008; 27(2): 812–820.
 89. Wang C, Jing H, Wang P, *et al.* Series metal-organic frameworks constructed from 1,10-phenanthroline and 3,3',4,4'-biphenyltetracarboxylic acid: Hydrothermal synthesis, luminescence and photocatalytic properties. *Journal of Molecular Structure* 2015; 1080: 44–51.
 90. Zang C, Wang M, Li Q, *et al.* Hydrothermal synthesis, crystal structure and luminescent properties of two zirconium(II) and cadmium(II) 3D metal-organic frameworks. *Zeitschrift Für anorganisch und Allgemeine Chemie* 2013; 639(5): 826–831.
 91. Yang L, Qiu L, Hu S, *et al.* Rapid hydrothermal synthesis of MIL-101(Cr) metal-organic framework nanocrystals using expanded graphite as a structure-directing template. *Inorganic Chemical Communications* 2013; 35: 265–267.
 92. De Oliveira CAF, da Silva FF, Malvestiti I, *et al.* Effect of temperature on formation of two new lanthanide metal-organic frameworks: synthesis, characterization and theoretical studies of Tm(III)-succinate. *Journal of Solid State Chemistry* 2013; 197: 7–13.
 93. Bernini MC, Brusau E V, Narda GE, *et al.* The effect of hydrothermal and non-hydrothermal synthesis on the formation of holmium(III) succinate hydrate frameworks. *European Journal of Inorganic Chemistry* 2007; 5: 684–693.
 94. Zhang K, Hou C, Song J, *et al.* Temperature and auxiliary ligand-controlled supramolecular assembly in a series of Zn(ii)-organic frameworks: syntheses, structures and properties. *CrystEngComm* 2012; 14(2): 590–600.
 95. Mcguire CV, Forgan RS. The surface chemistry of metal-organic frameworks. *Chemical Communications* 2015; 51: 5199–5217.
 96. Jin L, Liu Q, Sun W. Size-controlled indium (III)-benzendicarboxylate hexagonal rods and their transformation to In₂O₃ hollow structure. *CrystEngComm* 2013; 15: 4779–4784.
 97. Goesten M, Stavitski E, Pidko EA, *et al.* The molecular pathway to ZIF-7 microrods revealed by in situ time resolved small- and wide-angle X-ray scattering, quick scanning X-ray absorption spectroscopy and DFT calculation. *Chemistry-A European Journal* 2013; 19: 7809–7816.
 98. Zhao J, Guo Y, Guo H, *et al.* Solvothermal synthesis of mono- and bi-metallic flower-like infinite coordination polymer and formation mechanism. *Inorganic Chemical Communications* 2012; 18: 21–24.
 99. (a) Guo H, Zhu Y, Qiu S, *et al.* Coordination modulation induced synthesis of nanoscale Eu_{1-x}Tb_x-metal-organic frameworks for luminescent thin films. *Advanced Materials* 2010; 22: 4190–4192; (b) Guo G, Zhu Y, Wang S, *et al.* Combining coordination modulation with acid base adjustment for the control over size of metal-organic frameworks. *Chemical Materials* 2012; 24: 444–450.
 100. Wang F, Guo H, Chai Y, *et al.* The controlled regulation of morphology and size of HKUST-1 by “coordination modulation method”. *Microporous & Mesoporous Materials* 2013; 173: 181–188.
 101. Cravillon J, Nayuk R, Springer S, *et al.* Controlling zeolitic imizolate framework nano and microcrystal formation: insight into crystal growth by time-resolved in situ static light scattering. *Chemical Materials* 2011; 23: 2130–2141.
 102. Chin J, Chen E, Menon AG, *et al.* Tuning the aspect ratio of NH₂-MIL-53(Al) microneedles and nanorods via coordination modulation. *CrystEngComm* 2013; 15: 654–657.
 103. Schaate A, Roy P, Godt A, *et al.* Modulated synthesis of Zr-based metal-organic framework: from nano to single crystal. *Chemistry-A European Journal* 2011; 17: 6643–6651.
 104. Pham MH, Vuong GT, Fontaine FG, *et al.* Rational synthesis of metal-organic frameworks nanocubes and nanosheets using selective modulators and their morphology dependent gas-adsorption properties. *Crystal Growth & Design* 2012; 12(6): 3091–3095.
 105. Umemura A, Diring S, Furukawa S, *et al.* Mor-

- phology design of porous coordination polymer crystals by coordination modulation. *Journal of the American Chemical Society* 2011; 133: 15506–15513.
106. Vermoortele F, Bueken B, Le Bars G, *et al.* Synthesis modulation as a tool to increase catalytic activity of metal-organic frameworks: the unique case of UiO-66(Zr). *Journal of the American Chemical Society* 2013; 135: 11465–11468.
 107. Rieter WJ, Taylor KML, Lin W. Surface modification and functionalization of nanoscale metal-organic frameworks for controlling release and luminescent sensing. *Journal of the American Chemical Society* 2007; 129: 9852–9853.
 108. Horcajada P, Chalati T, Serre C, *et al.* Porous metal-organic framework nanoscale carriers as a potential platform for drug delivery and imaging. *Nature Materials* 2010; 9: 172–178.
 109. Diring S, Furukawa S, Takashima Y, *et al.* Controlled multiscale synthesis of porous coordination polymer in nano/micro regimes. *Chemical Materials* 2010; 22: 4531–4538.
 110. Taylor KLM, Rieter WJ, Lin W, *et al.* Manganese based nanoscale metal-organic frameworks for magnetic resonance imaging. *Journal of the American Chemical Society* 2008; 130: 14358–14359.
 111. Huxford RC, deKrafft KE, Boyle W, *et al.* Lipid-coated nanoscale coordination polymers for targeted delivery of antifolates to cancer cell. *Chemical Science* 2012; 3: 198–204.
 112. Kondo M, Furukawa S, Hirai K, *et al.* Coordinatively immobilized monolayers on porous coordination polymer crystals. *Angew Chem Int Ed* 2010; 49: 5327–5330.
 113. Liu X, Li Y, Ban Y, *et al.* Improvement of hydrothermal stability zeolitic imidazolate frameworks. *Chemical Communications* 2013; 49: 9140–9142.
 114. Hirai K, Chen K, Fukushima T, *et al.* Programmed crystallization via epitaxial growth and ligand replacement towards hybridising porous coordination polymer crystals. *Dalton Trans* 2013; 42: 15868–15872.
 115. Furukawa S, Hirai K, Nakagawa K, *et al.* Heterogeneously hybridizes porous coordination polymer crystal: fabrication of heterometallic core-shell single crystal with an in-plane rotational epitaxial relationship. *Angew Chem* 2009; 121: 1798–1802.
 116. Corma A, Garcia H, Llabrés i Xamena FX. Engineering metal organic framework in heterogeneous catalysis. *Chemical Reviews* 2010; 110: 4606–4655.
 117. Wong-Foy AG, Matzger AJ, Yaghi OM. Exceptional H₂ saturation in microporous metal-organic frameworks. *Journal of the American Chemical Society* 2006; 128: 3494–3495. doi: 10.1021/ja058213h.
 118. Wang X, Ma S, Forster PM, *et al.* Enhancing H₂ uptake by “close-packing” alignment of open copper sites in metal-organic frameworks. *Angew Chem Int Ed* 2008; 47: 7263–7266.
 119. Lin X, Telepeni I, Blake AJ, *et al.* High capacity H₂ adsorption in Cu(II) tetracarboxylate frameworks materials. The role of pore size, ligand functionalization and exposed metal sites. *Journal of the American Chemical Society* 2009; 131: 2159–2171.
 120. Farha OK, Yazaydin AO, Eryazici I, *et al.* De novo synthesis of a metal-organic framework material featuring ultrahigh surface area and gas storage capacities. *Nature Chemistry* 2010; 2: 944–948.
 121. Furukawa H, Ko N, Go YB, *et al.* Ultrahigh porosity in metal-organic frameworks. *Science* 2010; 329: 424–428.
 122. Dincă M, Long JR. High-enthalpy hydrogen adsorption in cation-exchanged variants of microporous metal-organic framework Mn₃[(Mn₄Cl)₃(BTT)₈(CH₃OH)₁₀]₂. *Journal of the American Chemical Society* 2007; 129: 11172–11176.
 123. Suh MP, Park HJ, Prasad TK, *et al.* Hydrogen storage in metal-organic frameworks. *Chemical Reviews* 2012; 112: 782–835.
 124. An J, Geib SJ, Rosi NL. High and selective CO₂ uptake in a cobalt adeninate metal-organic framework exhibiting pyrimidine and amino decorated pores. *Journal of the American Chemical Society* 2009; 132: 38–39.
 125. Noro S, Kitagawa S, Kondo M, *et al.* A new methane adsorbent porous coordination polymer [{Cu-SiF₆(4,4'-bipyridine)₂]_n}. *Angew Chem Int Ed* 2000; 39: 2081–2084.
 126. Ma S, Sun D, Simmons JM, *et al.* Metal organic framework from an anthracene derivative containing nanoscopic cage exhibiting high methane uptake. *Journal of the American Chemical Society* 2008; 130: 1012–1016.
 127. Allan PK, Xiao B, Teat SJ, *et al.* In situ single crystal diffraction studies of structural transition of metal-organic framework copper 5-sulphoisophthalate, Cu-SIP-3. *Journal of the American Chemical Society* 2010; 132: 3605–3611.
 128. Shimomura S, Higuchi M, Matsuda R, *et al.* Selective sorption of oxygen and nitric oxide by an electron-donating flexible porous coordination polymer. *Nature Chemistry* 2010; 2: 633–637.
 129. McKinlay AC, Xiao B, Wragg DS, *et al.* Exceptional behaviour over the whole adsorption-storage-delivery cycle for NO in porous metal-organic frameworks. *Journal of the American Chemical Society* 2008; 130: 10440–10444.
 130. Yan D, Chen B, Duan Q. A copper based metal-organic framework constructed from a new tetracarboxylic acid for selective gas separation. *Inorganic chemistry communication* 2014; 49: 34–36.
 131. Biswal BP, Kandambeth S, Chandra S, *et al.* Pore surface engineering in porous, chemically stable covalent organic frameworks for water adsorption. *Journal of Materials Chemistry A* 2015; 3: 23664–23669.
 132. Kurmoo M. Magnetic metal-organic frameworks. *Chemical Society Reviews* 2009; 38: 1353–1379. doi: 10.1039/b804757j.

133. Cheetham AK, Rao CNR. Materials science. There's room in the middle. *Science* 2007; 318: 58–59.
134. Cheetham AK, Rao CNR, Feller RK. Structural diversity and chemical trends in hybrid inorganic-organic framework materials. *Chemical Communications* 2006; 46: 4780–4795.
135. Coronado E, Míguez Espallargas G. Dynamic magnetic MOFs. *Chemical Society Reviews* 2013; 42: 1525–1539.
136. Okawa H, Shigematsu A, Sadakiyo M, *et al.* Oxalate-bridged bimetallic complexes $\{NH(\text{pro})_3\}[\text{M}(\text{ox})_3]$ ($\text{M} = \text{Mn}^{\text{II}}, \text{Fe}^{\text{II}}, \text{Co}^{\text{II}}, \text{NH}(\text{pro})_3^+ = \text{Tri}(3\text{-hydroxypropyl})\text{ammonium}$) exhibiting coexistent ferromagnetism and proton conduction. *Journal of the American Chemical Society* 2009; 131: 13516–13522.
137. Rao CNR, Natarajan S, Vaidhyanathan R. Metal carboxylates with open architectures. *Angew Chem Int Ed* 2004; 43: 1466–1496.
138. Mohideen MIH. Novel metal organic frameworks: synthesis, characterization and functions [PhD thesis]. Scotland: University of St. Andrews; 2011. Available from: <http://hdl.handle.net/10023/1892>.
139. MasPOCH D, Ruiz-Molina D, Wurst K, *et al.* A nanoporous molecular magnet with reversible solvent-induced mechanical and magnetic properties. *Nat Mater* 2003; 2: 190–195.
140. Roques N, MasPOCH D, Imaz I. A three dimensional lanthanide-organic radical open-framework. *Chemical Communications* 2008; 3160–3162.
141. Roques N, MasPOCH D, Luis F, *et al.* A hexacarboxylic open shell building block: synthesis structure and magnetism of a three dimensional metal-radical framework. *Journal of Materials Chemistry* 2008; 18: 98–108.
142. Guillou N, Livage C, Drillon M, *et al.* The chirality porosity and ferromagnetism of a 3D Nickel glutarate with intersecting 20 membered ring channels. *Angew Chem Int Ed* 2003; 42: 5314–5317.
143. Zhang X, Chui S, Williams ID. Cooperative magnetic behaviour in the coordination polymers $[\text{Cu}_3(\text{TMA})_2\text{L}_3]$, ($\text{L} = \text{H}_2\text{O}, \text{pyridine}$). *Journal Applied Physics* 2000; 87: 6007–6009.
144. Livage C, Egger C, Nogues M, *et al.* Hybrid open frameworks (MIL-n) part 5 synthesis and crystal structure of MIL-9: a new three dimensional ferromagnetic cobalt (II) carboxylates with a two dimensional array of edge sharing Co octahedral with 12-membered rings. *Journal of Materials Chemistry* 1998; 8: 2743–2747.
145. Jain P, Ramachandran V, Clark RJ, *et al.* Multiferric behaviour associated with an order-disorder hydrogen bonding transition in metal-organic frameworks (MOFs) with the perovskite ABX_3 architecture. *Journal of the American Chemical Society* 2009; 131: 13625–13627.
146. Chen M, Zhao H, Wang Z, *et al.* Two magnetic lanthanide-organic frameworks based on semi-rigid tripodal multicarboxylate ligand and different rod-shaped SBUs. *Inorganic Chemistry Communications* 2015; 56: 48–52.
147. Chandra V, Park J, Chun Y, *et al.* Water-dispersible magnetite-reduced graphene oxide composite for arsenic removal. *ACS Nano* 2010; 7(4): 3979–3986.
148. Tu Y, You C, Chang C, *et al.* XANES evidence arsenate removal from water with magnetic ferrite. *Journal of Environmental Management* 2013; 120: 114–119.
149. Rocha J, Carlos LD, Paz FAA, *et al.* Luminescent multifunctional lanthanides-based metal-organic frameworks. *Chemical Society Reviews* 2011; 40: 926–940.
150. Lu Z, Zhang R, Li Y, *et al.* Solvatochromic behavior of a nanotubular metal-organic framework for sensing small molecules. *Journal of the American Chemical Society* 2011; 133: 4172–4174.
151. Sun C, Wang X, Qin C, *et al.* Solvatochromic behaviour of chiral mesoporous metal-organic frameworks and their application for sensing small molecules and separating cationic dyes. *Chemistry-A European Journal* 2013; 19: 3639–3645.
152. Harbuzaru BV, Corma A, Rey F, *et al.* A miniaturized linear pH sensor based on a photoluminescent self-assembled Europium (III) metal-organic framework. *Angew Chem Int Ed* 2009; 48: 6476–6479.
153. White KA, Chengelis DA, Zeller M, *et al.* Near Infra-red emitting ytterbium metal-organic framework with tunable excitation properties. *Chemical Communications* 2009; 4506–4508.
154. Lim YT, Noh YW, Cho JH, *et al.* Multiplexed imaging of therapeutic cells with multispectrally encoded magnetofluorescent nanocomposite emulsions. *Journal of the American Chemical Society* 2009; 131: 17145–17154.
155. Desai AV, Manna B, Karmakar A, *et al.* A Water-stable cationic metal-organic framework as a dual adsorbent of oxoanion pollutants. *Angew Chem Int Ed* 2016; 55: 7811–7815.
156. Mukherjee S, Aamod V, Desai AV, *et al.* Exploitation of guest accessible aliphatic amine functionality of a metal-organic framework for selective detection of 2,4,6-Trinitrophenol (TNP) in water. *Crystal Growth & Design* 2015; 15: 4627–4634.
157. Deep A, Bhardwaj SK, Paul AK, *et al.* Surface assembly of nano metal organic framework on amine functionalized indium tin oxide substrate for impedimetric sensing of parathion. *Biosensors and Bioelectronics* 2015; 65: 226–231.
158. Garai B, Mallick A, Banerjee R. Photochromic metal-organic frameworks for inkless and erasable print printing. *Chemical Science* 2016; 7: 2195. doi: 10.1039/c5sc04450b.
159. Prestipino C, Regli L, Vitillo JG, *et al.* Local structure of framework Cu(II) in HKUST-1 metallorganic framework: Spectroscopic characterization upon

- activation and interaction with adsorbents. *Chemistry of Materials* 2006; 18: 1337–1346.
160. Hasegawa S, Horike S, Matsuda R, *et al.* Three dimensional porous coordination polymer functionalized with amide group based on tridentate ligand: selective sorption and catalysis. *Journal of the American Chemical Society* 2007; 129(9): 2607–2614.
161. Hwang Y, Hong D, Chang J, *et al.* Amine grafting on coordinatively unsaturated metal centers of MOFs: Consequences for catalysis and metal encapsulation. *Angew Chem Int Ed* 2008; 47: 4144–4148.
162. Xu J, Shimakoshi H, Hisaeda Y. Development of metal-organic framework (MOF)-B₁₂ system as new bio-inspired heterogeneous catalysis. *Journal of Organometallic Chemistry* 2015; 782: 89–95.
163. Taylor-poshow KML, Rocca JD, Xie Z, *et al.* Postsynthetic modification of iron-carboxylate nanoscale metal-organic frameworks for imaging and drug delivery. *Journal of the American Chemical Society* 2009; 131: 14261–14263.
164. McKinlay AC, Morris RE, Horcajada P, *et al.* Bio-MOFs: Metal-organic frameworks for biological and medical applications. *Angew Chem Int Ed* 2010; 49: 6260–6266.
165. Ke F, Yuan Y, Qiu L, *et al.* Facile fabrication of magnetic metal-organic framework nanocomposite for potential targeted drug delivery. *Journal of Materials Chemistry* 2011; 21: 3843–3848.
166. Bernini MC, Jimenez DF, Pasinetti M, *et al.* Screening of bio-compatible metal-organic frameworks as potential drug carriers using Monte Carlo simulations. *Journal of Materials Chemistry B* 2014; 2: 766–774.
167. Diaz R, Orcajo MG, Botas JA, *et al.* Co8-MOF-5 as electrode for supercapacitors. *Materials Letters* 2012; 68: 16–128.
168. Lee DY, Yoon SJ, Shrestha NK, *et al.* Unusual energy storage and charge retention in Co-based metal-organic frameworks. *Microporous & Mesoporous Materials* 2012; 153: 163–165.
169. Yang J, Zheng C, Xiong P, *et al.* Zn-doped Ni-MOF materials for high supercapacitive performance. *Journal of Materials Chemistry A* 2014; 2: 19005–19010.
170. Choi KM, Jeong HM, Park JH, *et al.* Supercapacitors for nanocrystalline metal-organic frameworks. *ACS Nano* 2014; 8: 7451–7458.
171. Qiao Q, Li G, Wang Y, *et al.* To enhance the capacity of Li rich layered oxides by surface modification with metal-organic frameworks as cathodes for advanced Lithium-ion batteries. *Journal of Materials Chemistry A* 2016; 4: 4440–4447.



Characterization and Application of Nanomaterials

Focus and Scope

Characterization and Application of Nanomaterials (CAN) is an open access peer-reviewed journal allowing maximum visibility of articles published in it as they are available to a wide, global audience. We are interested in the scientific topics from all fields of nano. CAN provides a forum to share scholarly practice to advance the use of nanomaterials in the context of scientific application.

CAN publishes original research articles, review articles, editorials, case reports, letters, brief commentaries, perspectives, methods, etc.

Examples of relevant topics include but are not limited to:

1. Nanoparticle composites
2. Nanoscale quantum physics
3. Modeling
4. Simulation
5. Nanotechnology and its application
6. Nanochemistry
7. Nanoscience, nano-medicine and bio-nanotechnology
8. Nanomaterials and energy applications
9. Micro-nano scale
10. Fabrication of thin film
11. Nanomaterial synthesis, characterization, and application
12. Nanotechnology and environmental protection
13. Photocatalytic degradation properties
14. Preparation of nanostructured materials

EnPress Publisher, LLC

EnPress Publisher, LLC, is a scholastic conduit for an assembly of professionals in the domains of science, technology, medicine, engineering, education, social sciences and many more, as a roundtable for their intellectual discourse and presentation, and as an instrument to galvanize research designs, policy implementation and commercial interests, to facilitate the prevailing over their challenges and to encourage to the full advantage of their resources and true potential.

We are the intellectual and academic home for academic, educators, scholars, clinicians, corporate researchers, who all play important roles in a wide range of national and international research organisations, and whose interests, expertise, research approaches and industry objectives from around the world coalesce together to advance significant contributions in their research and professional fields.

As an instrument of information purveyor, we seek to combine academic rigor and originality with the nuanced development of policy and practice. Via our journals, client database, online campaigns and social media presence, we offer a platform for industry professionals to interconnect, as well as opening doors towards cost-effective solutions for them to succeed, and we confidently hope to inspire a new generation of multidisciplinary researchers, think-tank experts, policymakers and business entities to innovate and advance their knowledge across fields.



EnPress Publisher,LLC

Add 14701 Myford Road,Suite B-1,Tustin,CA 92780,United States

Tel +1 (949) 299 0192

Email contact@enpress-publisher.com

Web <https://enpress-publisher.com>